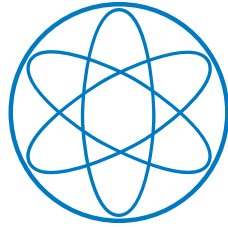


PHYSIK-DEPARTMENT



# Optimizing Detectors for Dark Matter Search

Diplomarbeit  
von

Moritz von Sivers



TECHNISCHE UNIVERSITÄT MÜNCHEN



*"The world is solid all the way through."*

Christopher Priest - *The Prestige*



## Abstract

One of the major issues in astrophysics today is the problem of dark matter (see chapter 1). It refers to the fact that various experimental observations show that there is a large amount of matter in the universe which interacts gravitationally but does not emit light and hence is called dark matter (DM). Observations suggest that most of the DM has to be of non-baryonic nature. Some extensions of the standard model (SM) of particle physics like supersymmetry (SUSY) do offer particles that have a mass  $\mathcal{O}(100\text{GeV})$  and interact only weakly and gravitationally. These weakly interacting massive particles (WIMPs) are well-motivated candidates for the DM. Experiments for the direct detection of DM try to make use of the property that WIMPs can scatter elastically off atomic nuclei producing small recoil energies of a few tens of  $\text{keV}$ . The expected rate for such interactions is very low ( $< 0.1\text{cts/kg/d}$ ), therefore these experiments require sensitive detectors with large target masses and are usually located in underground laboratories to be shielded from cosmic radiation.

CRESST, the Cryogenic Rare Event Search with Superconducting Thermometers located at the Laboratori Nazionali del Gran Sasso (LNGS) in Italy attempts to detect WIMP-nucleus scattering using modular cryogenic detectors (operating temperature  $\sim 10\text{mK}$ ) (see chapter 2). In the current second phase (CRESST-II) a single detector module consists of two individual cryogenic detectors enclosed together in a reflective housing: A scintillating  $\text{CaWO}_4$  crystal ( $\sim 300\text{g}$ ) which is equipped with a superconducting transition edge sensor (TES) to measure the temperature rise caused by an event in this detector and a second cryogenic detector for the simultaneous measurement of the scintillation light generated by the same event. Since nuclear recoil events produce significantly less scintillation light than electron recoils this technique can be used for active background discrimination.

As only a few percent of the deposited energy from an electron recoil is transformed into scintillation light in the crystals, the light collection efficiency is an important issue. In CRESST-II many scintillation photons are potentially left trapped inside the  $\text{CaWO}_4$  crystal due to its large refractive index ( $n \approx 1.95$ ) and the high symmetry of the currently used cylindrical shape.

Another important issue is to ensure the availability of scintillating crystals that match the special requirements of CRESST and the future European Underground Rare Event Calorimeter Array (EURECA), a planned multitarget experiment with a mass of up to 1ton (see chapter 3). For this purpose a dedicated Czochralski furnace has been installed at the crystal laboratory of the Technische Universität München (TUM).

During this thesis several  $\text{CaWO}_4$  crystals with a mass of  $\sim 250 - 790\text{g}$  were

---

produced in this setup (see chapter 4). The intrinsic light yield  $N_0$  and the scattering and absorption lengths  $L_{scat}$  and  $L_{abs}$  of a self-grown crystal were determined by a combination of experiments and MC simulations. The obtained values  $L_{scat} = 9.57 \pm 4.36cm$ ,  $L_{abs} = 4.34 \pm 0.90cm$  and  $N_0 = 24800 \pm 3300ph/MeV$  show that the crystal has a high light yield, however, due to the small value of  $L_{abs}$  a large fraction of the scintillation photons will be absorbed before escaping the crystal.

Furthermore, the influence of differently shaped crystals and reflective housings on the light collection in a CRESST-like detector module was studied by Monte Carlo (MC) simulations based on GEANT4 and compared to the currently used cylindrical crystal and housing (see chapter 5). The MC simulations favor a crystal shaped like a truncated pyramid in a box-shaped housing. In this module the light collection efficiency is improved by a factor of  $\sim 2$ . In addition, the light collection is more uniform with respect to the position of the scintillation event inside the crystal. However, the crystal shape has some disadvantages concerning the close packing of the detector modules. As an alternative a block-shaped crystal in a box-shaped housing offers close packing and also exhibits a more uniform light collection and an unchanged collection efficiency compared to the currently used cylindrical module. In addition, a block-shaped crystal has the advantage of losing little material and will be relatively easy to manufacture from the originally grown ingot which also has a block-like shape.

The light yields of differently shaped crystals that were cut from a self-grown ingot and mounted in differently shaped reflective housings, as suggested by the MC simulations, were measured in a dedicated setup at room temperature (see chapter 6). Furthermore, the effects of annealing the crystals under oxygen atmosphere and roughening of one of the crystals' surfaces were investigated. Depending on the crystal shape both procedures combined increased the measured light yield by  $\sim 16 - 39\%$ . In comparison to a cylindrical crystal and housing the measurements favor a block-shaped crystal in a box-shaped housing since it exhibits a more uniform light collection and a similar measured light yield. A crystal shaped like a truncated pyramid in a box-shaped housing showed an increase of the measured light yield by  $\sim 42\%$  but a less uniform light collection and therefore no significant improvement.

The MC simulations and experiments suggest that a block-shaped crystal in a box-shaped housing is a favorable design concerning future detectors for CRESST and especially for the planned large-scale EURECA experiment.

# Contents

<b>1</b>	<b>Introduction</b>	<b>1</b>
1.1	The Dark Matter Problem . . . . .	1
1.1.1	Evidence for Dark Matter . . . . .	1
1.1.2	Dark Matter Candidates . . . . .	5
1.2	Experimental Search for Dark Matter . . . . .	7
<b>2</b>	<b>The CRESST-II Experiment</b>	<b>9</b>
2.1	Basics of Cryogenic Detectors . . . . .	9
2.2	CRESST-II Detector Setup . . . . .	10
2.2.1	Phonon Detector . . . . .	11
2.2.2	Light Detector . . . . .	13
2.3	Active Background Suppression . . . . .	13
2.3.1	Importance of the light collection . . . . .	14
2.4	The CRESST-II Low-Background Setup . . . . .	17
2.5	CRESST-II Results . . . . .	18
2.5.1	Commissioning Run . . . . .	18
2.5.2	Current Run . . . . .	20
<b>3</b>	<b>The EURECA Experiment</b>	<b>25</b>
<b>4</b>	<b>Scintillating <math>CaWO_4</math> Crystals</b>	<b>29</b>
4.1	Czochralski Growth Method . . . . .	29
4.1.1	Experimental Setup . . . . .	29
4.1.2	Growth Process . . . . .	33
4.1.3	Grown Crystals . . . . .	35
4.2	Review of Scintillation Properties . . . . .	39
4.3	Light Trapping in Cylindrical Crystals . . . . .	40
4.4	Strategies to Improve the Light Collection . . . . .	42
<b>5</b>	<b>Monte Carlo (MC) Simulations</b>	<b>47</b>
5.1	Light-Output Simulation . . . . .	47

5.1.1	Results and Discussion . . . . .	48
5.2	Simulation of a CRESST-like Detector Module . . . . .	54
5.2.1	Results and Discussion . . . . .	56
5.3	Simulation of Differently Shaped Crystals and Housings . . . . .	62
5.3.1	Results and Discussion . . . . .	63
5.4	Summary and Consequences for New Detectors . . . . .	75
<b>6</b>	<b>Characterization of the Self-Grown <math>CaWO_4</math> Crystals</b>	<b>79</b>
6.1	Transmission Measurement . . . . .	79
6.1.1	Results and Discussion . . . . .	79
6.2	The Monte-Carlo Refractive Index Matching Technique . . . . .	81
6.2.1	Experimental and MC Setup . . . . .	82
6.2.2	Photon Counting Technique . . . . .	86
6.2.3	Results and Discussion . . . . .	89
6.2.4	Testing the Obtained Values . . . . .	94
6.3	Light-Yield Measurements of Differently Shaped Crystals and Housings . . . . .	97
6.3.1	Results and Discussion . . . . .	99
6.3.2	Influence of the Position of the Irradiating Source . . . . .	108
6.4	Comparison of the MLY to the Reference Crystal "Boris" . . . . .	113
6.4.1	Results and Discussion . . . . .	113
6.5	Measurement of the Radiopurity . . . . .	115
6.6	Summary and Consequences for New Detectors . . . . .	117
<b>7</b>	<b>Conclusion and Outlook</b>	<b>121</b>
7.1	Czochralski Growth of $CaWO_4$ Crystals . . . . .	121
7.2	Optical and Scintillation Properties of the Self-Grown Crystals . . . . .	121
7.3	Investigation of Differently Shaped Crystals and Housings . . . . .	123
7.4	Post-Growth Treatment of the Crystals . . . . .	125
7.5	Consequences for New Detectors . . . . .	125
	<b>Appendices</b>	<b>129</b>
	<b>A Estimation of the expected pileup in the light yield measurements</b>	<b>129</b>
	<b>Bibliography</b>	<b>131</b>
	<b>Acknowledgements</b>	<b>137</b>

# Chapter 1

## Introduction

### 1.1 The Dark Matter Problem

The first evidence of dark matter came from Swiss astronomer Fritz Zwicky in 1933 [1]. Observing the velocities of galaxies in the Coma cluster he found that "the average density in the Coma system would have to be at least 400 times larger than that derived on the grounds of observations of luminous matter". Even if we revise the Hubble constant Zwicky used to a presently accepted value this argument for dark matter (DM) still stands. Today the existence of dark matter is well supported by various different observations on all cosmological scales but a direct detection of dark matter particles has still not been possible.

#### 1.1.1 Evidence for Dark Matter

Today, evidence for dark matter comes from the rotational curves of galaxies, the observation of clusters as well as the model of big bang nucleosynthesis (BBN) and the fluctuations in the cosmic microwave background radiation (CMBR).

From Newtonian mechanics the rotational speed  $v(r)$  in a galaxy at distance  $r$  from the center should be

$$v(r) = \sqrt{\frac{GM(r)}{r}} \quad (1.1)$$

where  $M(r)$  is the mass within the distance  $r$ . At large distances from the galaxy's center therefore the dependence should be

$$v(r) \propto r^{-\frac{1}{2}} \quad (1.2)$$

However, in most observed galaxies it was found that the rotational velocity is constant at large distances (see figure 1.1). This can be best explained by an

isothermal halo of dark matter in the galaxies with a spherical density distribution [2]

$$\rho(r) = \rho_0 \left[ 1 + \left( \frac{r}{r_c} \right)^2 \right]^{-1} \quad (1.3)$$

where  $\rho_0$  is the central halo density and  $r_c$  the halo core radius.

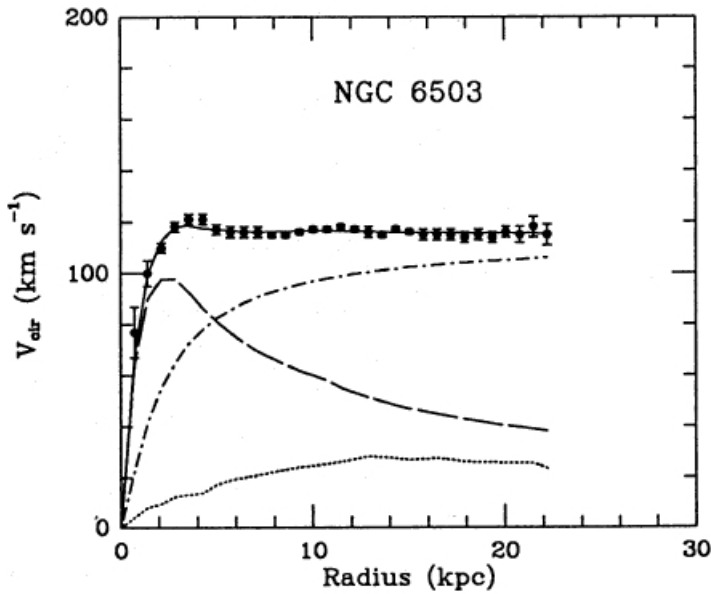


**Fig. 1.1:** Dark-halo model fit (solid line) to the measured rotation curve (points) of the galaxy NGC 6503. The rotation curves of the individual components are also shown: visible component (dashed line), gas (dotted line) and dark halo (dash-dot line) [2].

Some massive non-luminous objects can be explained by baryonic matter like brown dwarfs and neutron stars, or by black holes. The total amount of baryonic matter though is limited by the model of primordial nucleosynthesis which can predict the abundances of elements along ten orders of magnitude, if baryonic matter contributes only 4% to the total matter-energy density of the universe [3]. A direct evidence for non-baryonic dark matter comes from the interpretation of fluctuations in the cosmic microwave background radiation (CMBR). The CMBR is the remnant radiation from the time when the universe became transparent due to the formation of hydrogen atoms  $\sim 380000$  years after the big bang at a temperature of  $\sim 3000K$ . It is redshifted by the expansion of the universe to an average temperature of  $2.725K$  observed today and exhibits a nearly perfect black body spectrum. The Wilkinson Microwave Anisotropy Probe (WMAP) satellite mission, launched in 2001 obtained a sky map of the CMBR that shows a distribution

isotropic on large scales with temperature fluctuations smaller than  $200\mu K$  (see figure 1.2) [4]. By expansion into spherical harmonics a power spectrum giving the temperature fluctuations at different angular sizes is obtained (see figure 1.3). The fluctuations at large angular sizes represent the primordial density fluctuations that led to the formation of the structures observed today, while the fluctuations on small scales depend on the conditions at the time of decoupling and are due to thermoacoustic oscillations of the baryons and photons. The height and position of the observed peaks depend on the parameters of the cosmological model. It was found that the best fit for a standard cosmological  $\Lambda$ CDM model is obtained with a flat universe dominated by vacuum energy (assigned to the cosmological constant  $\Lambda$ ) and cold dark matter (CDM) [5]. The energy content of the universe derived from this fit is shown in figure 1.4. It can be seen that at the time of decoupling of the CMBR the universe was dominated by dark matter. In addition, photons, neutrinos and baryonic matter did also contribute significantly to the matter-energy density. In contrast today, as the contributions have changed due to the expansion of the universe, it is dominated by dark energy. Furthermore, baryonic matter constitutes less than 5% of the total matter-energy density while over 20% consists of dark matter the nature of which is still unclear.

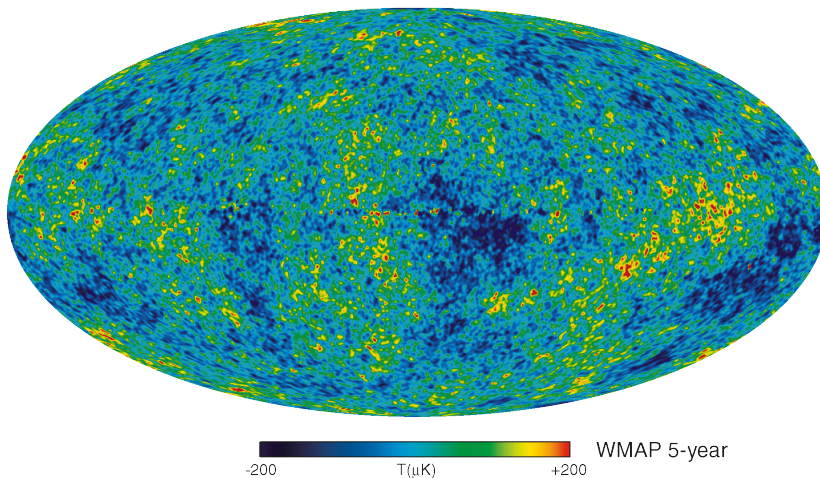


**Fig. 1.2:** Full skymap of the CMBR measured by the WMAP satellite. It shows a distribution that is isotropic on large scales with temperature fluctuations smaller than  $200\mu K$  [4].

## 1. Introduction

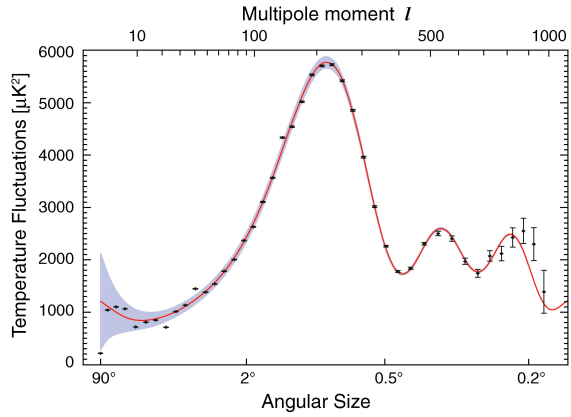


**Fig. 1.3:** Power spectrum obtained from a multipole expansion of the temperature fluctuations in the CMBR. The curve shows the best fit for a standard  $\Lambda$ CDM model to the data from which the cosmological parameters can be derived [5].

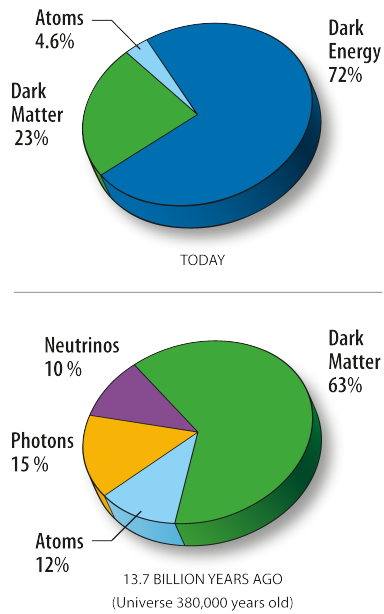


**Fig. 1.4:** Content of the Universe today (top) and at the time of decoupling of the CMBR (bottom). It can be seen that at the time of decoupling the universe was dominated by dark matter. In addition, photons, neutrinos and baryonic matter did also contribute significantly to the matter-energy density. In contrast today, the universe is dominated by dark energy. Furthermore, baryonic matter constitutes less than 5% of the total matter-energy density while over 20% consists of dark matter [5].

A recent observation strongly suggesting the existence of dark matter comes from the collision of galaxy clusters. Up to now two of these objects have been found [6, 7]. In both cases the total mass distribution derived by gravitational lensing showed two distinct peaks. These are clearly offset from the main baryonic component (the hot gas) derived by x-ray observations, which - in contrast to DM - slowed down during the collision due to friction (see figure 1.5). This suggests that the total mass is dominated by an almost "collisionless" form of dark matter, which severely challenges alternative explanations, for example the theory of modified Newtonian dynamics (MOND).

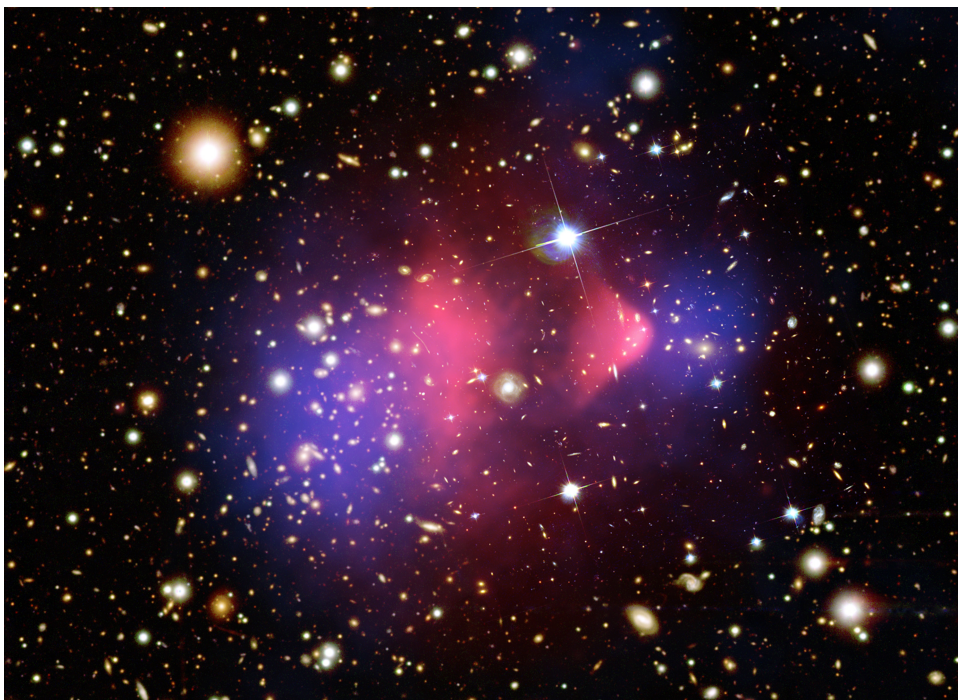


**Fig. 1.5:** The "Bullet Cluster" was formed by the collision of two smaller galaxy clusters. The dark matter (blue), derived by gravitational lensing, has passed the collision point while the hot gas (pink), derived by x-ray observations, slowed down due to friction.

### 1.1.2 Dark Matter Candidates

Because of its role as a catalyst in the formation of galaxies in the early universe non-baryonic dark matter is considered "cold", i.e. it consists of particles that were non-relativistic at their time of decoupling [8]. Furthermore, they should have a lifetime larger than the age of the universe and not be electromagnetically or strongly interacting hence charge and color neutral. Also their calculated relic

abundance should be in the observed range although it might be smaller in case of a multicomponent CDM.

At first neutrinos as the only viable standard model (SM) particles were considered as a DM candidate. However, neutrinos are relativistic at their time of decoupling and would average over primordial density fluctuations and thus make galaxy formation unlikely. Therefore, they only contribute to the hot dark matter (HDM) in the universe.

A suitable CDM candidate would be the axion which is the Goldstone boson of the Peccei-Quinn symmetry breaking that was introduced to explain the CP conservation in strong interactions described by QCD. Its mass should be  $\sim 10^{-6} - 1eV$  which gives it a proper relic abundance<sup>1</sup>. Axions can be converted into photons when crossing magnetic fields. Experiments for axion detection based on this principle are currently being pursued [9].

Interestingly, particles with a mass of  $100 - 1000GeV$  and an annihilation cross section typical of weakly interacting particles automatically lead to a relic density in the observed range [10]. This is sometimes referred to as the "WIMP<sup>2</sup> miracle" [11]. A well-motivated WIMP candidate is offered by supersymmetry (SUSY), which is often considered the most natural extension of the SM. In SUSY every SM particle has a super partner with same quantum numbers but spin differing by half an integer. Furthermore SUSY is assumed to be spontaneously broken to give these so called sparticles a higher mass than their SM partners. SUSY allows baryon and lepton number violation but in most scenarios a multiplicative quantum number called R-parity calculated by  $R = (-1)^{2S+3B+L}$  is conserved, to restore the proton lifetime to an acceptable value. Here  $S$  is the spin and  $B$  and  $L$  are the lepton and baryon number, respectively. In this way all SM particles have R-parity  $+1$  while all SUSY particles have R-parity  $-1$ . Hence, the lightest supersymmetric particle (LSP) is stable. In most models the LSP is the lightest neutralino which is a linear combination of the neutral gauginos and higgsinos (the super partners of the gauge and higgs bosons). Since it is expected to have a mass in the GeV range, to interact only weakly and to be stable it is an excellent candidate for the CDM. The neutralino might be directly produced in the LHC and identified by the large missing energy when it escapes the detector.

Besides WIMPs and axions there are a number of more exotic DM candidates (e.g. Kaluza-Klein particles, WIMPzillas, sterile neutrinos, sneutrinos, gravitinos, axinos, ...) that arise from the large variety of theories beyond the standard model [12, 11].

---

<sup>1</sup>The axion is a suitable CDM candidate despite its low mass because it was never in thermal equilibrium.

<sup>2</sup>Weakly Interacting Massive Particle

## 1.2 Experimental Search for Dark Matter

Two possibilities can be explored to search for DM. One is the indirect dark matter search that looks for annihilation or decay products of DM. The other possibility is to search for direct interactions of DM particles in terrestrial detectors. It is assumed that DM particles are distributed in a roughly isothermal halo in our galaxy with a density of  $\sim 0.3\text{GeV}/\text{cm}^3$  at the position of the earth [13]. Because of the relative motion of the milky way, with a velocity of  $\sim 220\text{km}/\text{s}$  relative to the galactic halo this leads to "WIMP-wind". In the simplest model these WIMPs could be detected by their elastic scattering off atomic nuclei, which because of the small momentum transfers is coherent, i.e. the WIMP scatters simultaneously off all nucleons. In the direct dark matter search "coherent scattering" is sometimes also used as a synonym for "spin-independent scattering" since for spin-dependent interactions only unpaired nucleons contribute to the total scattering cross section. Detecting WIMPs one would expect an annular modulation of the signal with amplitudes of a few percent because of the motion of the earth around the sun. This has been reported by the DAMA/LIBRA collaboration [14] although their parameter space in the standard WIMP scenario for coherent (spin-independent) elastic scattering is ruled out by several other experiments including CRESST-II. To resolve this conflict several other models have been suggested like spin-dependent scattering [15], scattering of electrons [16], light dark matter [17] or inelastic scattering [18] (see section 2.5).



# Chapter 2

## The CRESST-II Experiment

CRESST, the Cryogenic Rare Event Search with Superconducting Thermometers located at the Laboratori Nazionali del Gran Sasso (LNGS) in Italy is a direct dark matter search experiment using low-temperature calorimeters. In the current second phase (CRESST-II), the cryogenic detectors are based on scintillating  $CaWO_4$  crystals with active background suppression using the phonon-light technique. Passive background suppression is achieved by a low-background installation and the deep underground location. In addition, gamma and neutron shields as well as a muon veto are installed.

### 2.1 Basics of Cryogenic Detectors

A cryogenic detector measures the temperature rise  $\Delta T$  resulting from the energy  $\Delta E$  deposited as heat by an event in an absorber crystal:

$$\Delta T = \frac{\Delta E}{C} \quad (2.1)$$

To reach a reasonable sensitivity, it is best to go to very low temperatures (mK range) where the heat capacities  $C$  are small.<sup>1</sup> Still, the temperature rise from a  $keV$  event is only a few  $\mu K$ . Nevertheless it is possible to measure such changes in temperature using temperature dependent resistors (thermistors). Two different kind of thermistors are currently used in cryogenic detectors: compensated doped semiconductors (e.g. Neutron Transmutation Doped (NTD) Ge, ion implanted Si) and superconductors in their phase transition, called transition edge sensors (TES). The principle of the latter is that if a superconductor is operated around its transition temperature, a small rise in temperature  $\Delta T$  causes a steep

---

<sup>1</sup>In the Debye approximation  $C \propto T^3$  for the contribution from phonons (insulators). For the contribution from electrons (metallic systems)  $C \propto T$ .

(approximately linear) rise of the resistance  $\Delta R$  (see figure 2.1). The sensitivity is determined by the steepness of the transition characterized by the parameter  $\alpha$ , which is defined as the logarithmic derivation of the sensor's resistance  $R_T$  over the temperature  $T$ .

$$\alpha = \frac{d \ln R_T}{d \ln T} \quad (2.2)$$

A TES is realized by depositing a thin film of a superconducting material on an absorber crystal. To measure the changes in the resistance  $R_T$  of the film it is wired in a circuit parallel to a reference (shunt) resistance  $R_S$  (see figure 2.1). The whole circuit is biased with a constant current  $I_0$ . A change of  $R_T$  causes a change of the current in the superconducting coil  $L_I$ . The resulting change of the magnetic field in the coil is then coupled into a Superconducting Quantum Interference Device (SQUID), which acts as a "cold preamplifier".

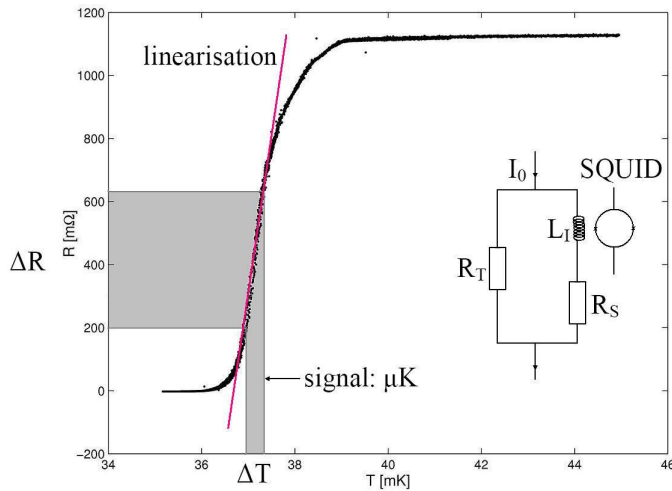


**Fig. 2.1:** Working principle of a TES. In a superconductor operated at the transition temperature a small change in temperature causes a steep approximately linear rise in resistance  $R_T$ . The whole circuit is biased with a constant current  $I_0$ . A change of  $R_T$  causes a change of the current in the superconducting coil  $L_I$  which is then read out by a Superconducting Quantum Interference Device (SQUID).

## 2.2 CRESST-II Detector Setup

CRESST-II attempts to detect WIMP-nucleus scattering events with modular detectors. A single detector module consists of a scintillating  $CaWO_4$  target crystal, operated as a cryogenic calorimeter (the phonon channel) to measure the deposited

energy from a scattering particle in form of phonons, and a nearby but separate cryogenic detector optimized for the simultaneous detection of scintillation photons (the light channel). The two cryogenic detectors are enclosed together in a highly reflective housing and are each read out by a tungsten TES (see figure 2.2). The reflector is a polymeric multilayer foil (3M Radiant Mirror Film VM2002). This foil has a reflectivity greater than 98% at room temperature (RT) for photons of wavelengths in the range of  $\sim 400 - 1000nm$  [19], which covers nearly the whole  $CaWO_4$  spectrum. It was found that the side with the Polyethylenephthalate (PEN) support layer of the foil is also scintillating.<sup>2</sup> In the detector setup this side faces the  $CaWO_4$  crystal. This is useful because recoiling daughter nuclei from  $\alpha$  decaying radioimpurities on the crystal's or foil's surface that enter the  $CaWO_4$  crystal can mimic a WIMP signal. However, the scintillation signal caused by the  $\alpha$  particle being absorbed on the reflective foil allows to discriminate such events [20]. The holders for the detectors are made from bronze ( $CuSn_6$ ) clamps that are covered with a silver coating to increase their reflectivity.

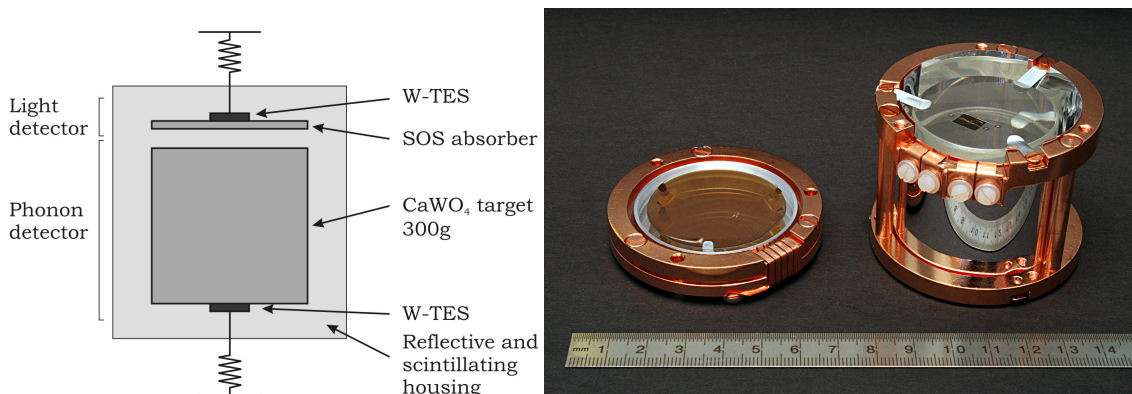


**Fig. 2.2:** Schematic drawing (left) and photograph of a CRESST-II detector module (right). The module consists of a scintillating  $CaWO_4$  crystal equipped with a tungsten TES to measure the phonon signal and a silicon-on-sapphire (SOS) light detector for the simultaneous detection of the scintillation light. The light and phonon detector are enclosed together in a reflective and scintillating housing.

### 2.2.1 Phonon Detector

The phonon detector consists of a  $\sim 300g$  cylindrical  $CaWO_4$  crystal with 40mm diameter and height.  $CaWO_4$  was - among other reasons - selected as scintillator because of its high light yield at low temperatures and because of the large atomic

<sup>2</sup>Since the excitation spectrum of the foil overlaps with the emission spectrum of  $CaWO_4$  it has also wavelength shifting properties [21].

## 2. The CRESST-II Experiment

---

mass of tungsten ( $A=183.86$ ) which makes it a favorable target for WIMPs, since the cross section for coherent elastic scattering is proportional to  $A^2$  [22]:

$$\sigma_{coh} \propto A^2 \quad (2.3)$$

The thermometer is a  $6 \times 8 \text{ mm}^2$ ,  $200 \text{ nm}$  thick superconducting tungsten film (W-TES) evaporated on the surface of the  $\text{CaWO}_4$  crystal. The superconducting transition temperature is  $\sim 10 \text{ mK}$ . Thermal and electrical connections are made by gold and aluminum bondwires. These connect contact pads on the thermometer and the detector holder to the mixing chamber of the dilution refrigerator and to the SQUID readout circuit. A rise in the thermometer resistance and a following increase in current through the SQUID coil is then observed as a rise in SQUID output voltage.

In the present run of CRESST-II there are also three  $\text{CaWO}_4$  crystals where the W-TES is not directly deposited onto the crystal surface but on a small  $10 \times 20 \times 1 \text{ mm}^3$   $\text{CaWO}_4$  substrate which is then glued onto the bigger absorber crystal (see figure 2.3). This composite detector design (CDD) was developed within the "cryoGNO" project [23, 24]. For the  $\text{CaWO}_4$  crystals of CRESST-II it has the advantage that it avoids the thermal stress when the TES is evaporated directly onto the crystal surface which can decrease the light yield by 50% due to the loss of oxygen [25]. In addition, the current run employs two (CDD)  $\text{ZnWO}_4$  crystals, which is being tested as a possible future material because of its higher light yield and higher radiopurity [26].

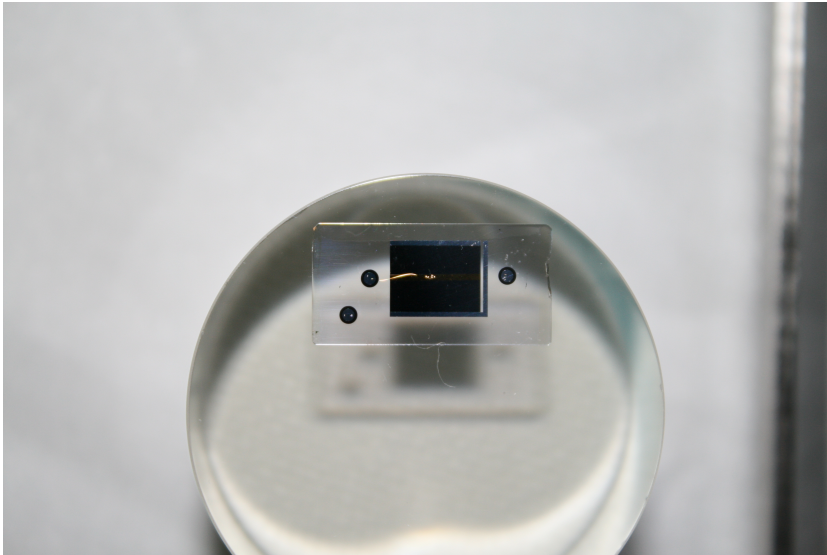


**Fig. 2.3:** Composite detector design (CDD) where the W-TES is deposited onto a small  $\text{CaWO}_4$  substrate which is then glued onto the bigger absorber crystal [27].

### 2.2.2 Light Detector

In the CRESST setup about 1% of the energy deposited by a gamma in the  $CaWO_4$  is detected as scintillation light [28]. To reach a good sensitivity and because conventional photodetectors are not operable at mK temperatures, the light is detected by another cryogenic detector. In the current run the light detector consists of a disc shaped silicon-on-sapphire (SOS) waver with 40mm diameter equipped with a W-TES. The SOS waver is made of a  $1\mu m$  thick silicon layer for optical absorption evaporated onto a  $460\mu m$  thick sapphire substrate, which has very good phonon propagation properties. In the detector module, the sapphire side which shows a higher optical absorption<sup>3</sup> then faces the  $CaWO_4$  crystal. In the current run of CRESST-II there is also one module employing two light detectors (one facing each planar side of the  $CaWO_4$  crystal) that is being tested for better light collection.

## 2.3 Active Background Suppression

An active background discrimination in the CRESST-II experiment is achieved by a simultaneous measurement of the deposited energy in phonons and scintillation light. The phonon signal is - in the first approximation - independent of the type of event and constitutes usually  $\sim 95\%$  of the deposited energy, while nuclear recoils produce less scintillation light than electron recoils. In this way, background from gamma and beta events can be rejected by their increased light to phonon ratio [30]. The reduction factor of the light yield from a nuclear recoil relative to an electron recoil of the same energy is given by the quenching factor (QF):

$$QF = \frac{\text{Light Yield for an Electron Recoil Event of Energy } E}{\text{Light Yield for a Nuclear Recoil Event of Energy } E} \quad (2.4)$$

It was found that the QFs vary for different nuclei and show a systematic increase throughout the periodic table [31]. This is particularly useful because neutrons and WIMPs scatter predominantly off different nuclei. Monte Carlo studies show that neutrons with an energy spectrum typical for Gran Sasso will produce recoils in the energy range of interest predominantly on the oxygen nuclei [32]. In contrast, coherently interacting WIMPs will scatter predominantly off tungsten nuclei. In this way, background from neutron events can be rejected by only accepting tungsten nuclear recoils. For the discrimination between the different types of recoils, events are usually plotted with their energy in the light channel vs. the energy in the phonon channel. In this plot the events appear in bands with different slopes

<sup>3</sup>This can be assigned to the fact that a beam of light that is diffusely reflected from the silicon can be reflected on the sapphire-air interface so that it hits the silicon layer again [66].

that are determined by their quenching factors (see figure 2.4). Also sometimes the ratio of the light and phonon channel is plotted on the y-axis so that the bands appear horizontally. This ratio is normalized to 1 for the average of electron recoils. The width of the bands is determined by the energy resolutions of the phonon and light channels and is dominated by the latter since the resolution of the phonon channel is about one order of magnitude better.

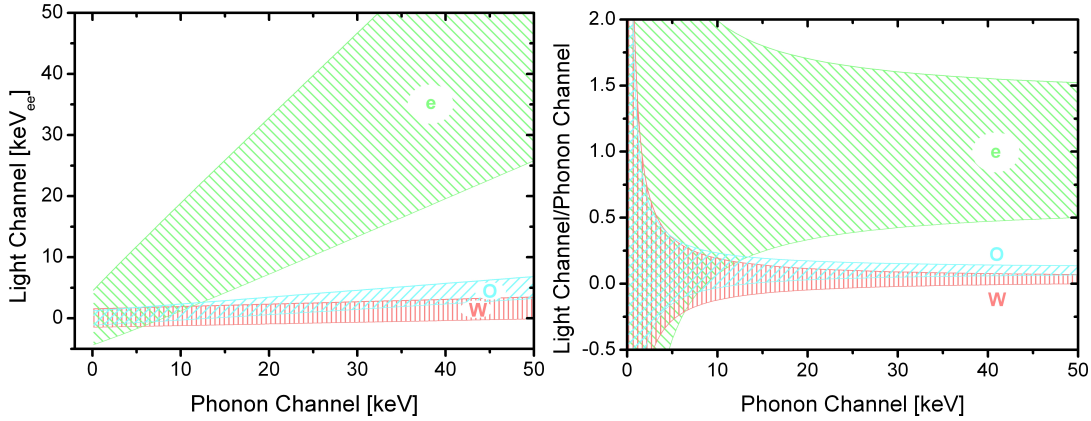


**Fig. 2.4:** Separation of different types of recoil events into bands with different slopes determined by the QFs in the so called "phonon-light" plot (left picture). Electron recoils (e) are shown in green, oxygen recoils (O) in blue and tungsten recoils (W) in red. The simplified quenching factors used here are rounded values of quenching factor measurements. The right picture is identical to the left except that the ratio of the light and phonon channel is plotted on the y-axis. This ratio is normalized to 1 for the average of electron recoils. The width of the bands is determined by the energy resolutions of the phonon and light channels. The  $1\sigma$  energy resolution was taken as  $\Delta E = \sqrt{1.44keV^2 + 0.33keV E + 0.01E^2}$  which is a typical derived value of the CRESST-II light channels [33].

### 2.3.1 Importance of the light collection

The differential rate for WIMP scattering  $\frac{dR}{dE_r}$  expressed in  $keV^{-1}kg^{-1}d^{-1}$  decreases exponentially with the recoil energy  $E_r$  [22].

$$\frac{dR}{dE_r} \propto e^{-E_r} \quad (2.5)$$

For the scattering on tungsten this leads to a vanishing event rate above  $40keV$  (see figure 2.5). Below  $\sim 10keV$  the nuclear and electron recoil band can not be discriminated anymore (see figure 2.6). Therefore, the energy range to search for

WIMP events in CRESST-II extends from  $\sim 10\text{keV} - 40\text{keV}$ .

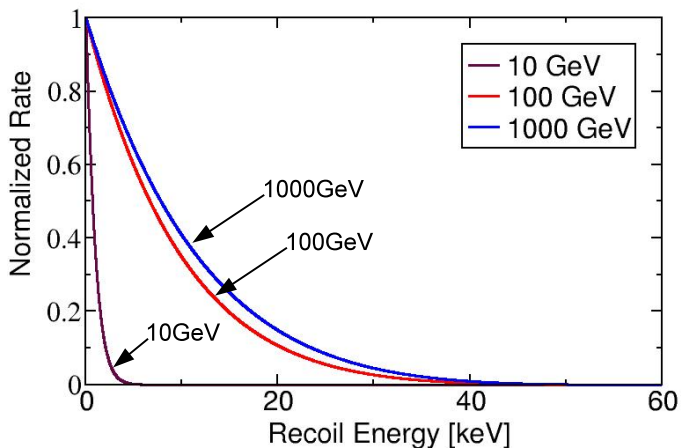


**Fig. 2.5:** Tungsten recoil spectra for various WIMP masses.

For an electron recoil the fraction of the deposited energy that is detected as scintillation light is  $\sim 1\%$  [28]. In case of tungsten nuclear recoils with a QF  $\gtrsim 33$  [34], recoil energies  $< 40\text{keV}$  and a mean scintillation photon energy of  $2.8\text{eV}$  [35] correspond to less than  $\frac{40\text{keV} \cdot 1\%}{2.8\text{eV} \cdot 33} \approx 4$  detected photons. Such small light signals are compatible with noise (see figure 2.6). Improving the light collection efficiency therefore will help to identify tungsten recoils which currently are dismissed as "phonon only" events since such events can also result from cracks in the crystals caused by too tight clamping [36]. Furthermore, with only a few detected photons the energy resolution for a nuclear recoil event in the energy range of interest is limited by photon statistics. Increasing the number of detected photons is therefore indispensable to obtain a better resolution of the light channel in addition to an improved light detector with less electronic noise as provided by the Neganov-Luke effect (see section 4.4). This will lead to more narrow recoil bands which lowers the possible discrimination threshold between nuclear and electron recoils (see figure 2.7). According to equation (2.5) this would greatly enhance the sensitivity of the experiment. In addition, with a better energy resolution of the light channel there will also be less overlap between the different nuclear recoil bands which is important for the discrimination between neutrons and coherently interacting WIMPs. Furthermore a module with an improved discrimination between different types of nuclear recoil events is of particular importance for the measurement of the quenching factors in  $\text{CaWO}_4$  at  $m\text{K}$  temperatures. This is currently being pursued at a neutron scattering experiment at the Maier-Leibnitz-Laboratorium

(MLL) in Garching [37].

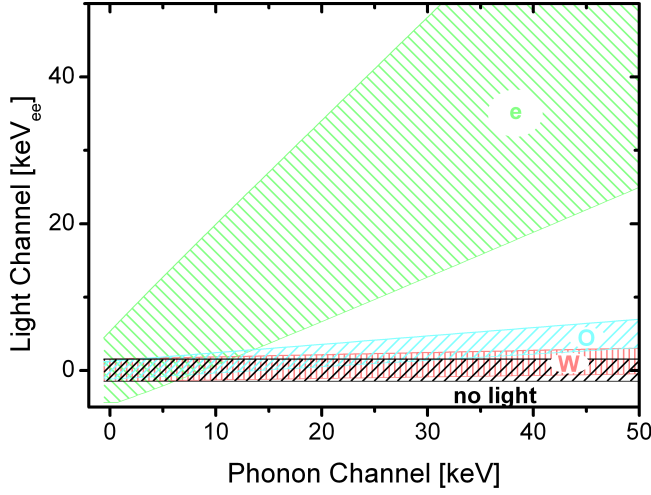


**Fig. 2.6:** Separation of different types of recoil events into bands in the "phonon-light" plot. Tungsten nuclear recoils in the expected energy range lead to very small light signals compatible with thermal noise. For other details see figure 2.4 [33].

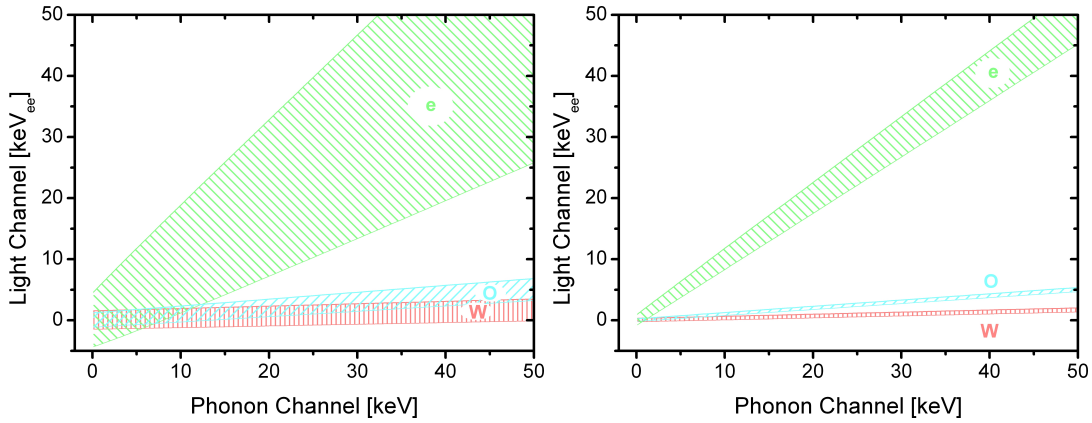


**Fig. 2.7:** Separation of different types of recoil events into bands in the "phonon-light" plot. In the right picture the energy resolution of the light channel is improved by a factor of 5. For other details see figure 2.4 [33].

## 2.4 The CRESST-II Low-Background Setup

Since the expected event rate for WIMP interactions is very low it is important for the CRESST-II experiment to be shielded efficiently against all kinds of background. In order to realize a low-background setup different strategies are applied. The CRESST-II experiment is setup in hall A of the LNGS under a minimum rock overburden of  $\sim 1400m$  ( $\sim 3500m.w.e.$ ), thus reducing the surface muon flux by six orders of magnitude to  $\sim 1m^{-2}h^{-1}$  [38]. The commercially available  $^3He$ - $^4He$  dilution refrigerator cooling the detectors to their operating range contains materials with an amount of radioimpurities not suited for a low-background setup. Therefore the cryostat (CR) is kept separate from the shielded detectors (see figure 2.8), and the cooling power is transferred to the shielded volume via a  $1.3m$  long cold finger (CF) made of ultra-pure copper. The current setup can hold up to 33 detector modules (carousel CA), allowing for a total target mass of  $\sim 10kg$  when equipped with the currently used  $CaWO_4$  crystals. The parts within the experimental volume are mostly made from ultra-pure copper. It is surrounded by the thermal shields of the cryostat and additional shields of ultra-pure copper (CU) and low-radioactivity lead (PB) against gamma particles. All parts are surrounded by the radon box (RB), a container constantly flushed with nitrogen gas to displace radon. Outside the radon box a  $\sim 45cm$  thick polyethylene shield (PE) against neutrons and plastic scintillator panels as an active muon veto (MV) are installed. The experimental setup including the primary electronics is surrounded by a Faraday cage equipped as a clean room. With closed shields the trigger rate of one detector module is  $\sim 0.05 - 0.5Hz$ .

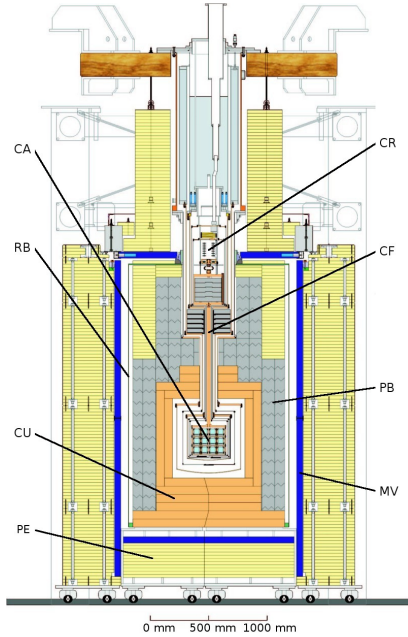


**Fig. 2.8:** Experimental setup of CRESST-II: CA indicates the detector carousel, CR the mixing chamber of the cryostat, CF the cold finger, PB the lead shield, MV the muon veto, PE the polyethylene shield, CU the copper shield, and RB the radon box.

## 2.5 CRESST-II Results

### 2.5.1 Commissioning Run

In the standard scenario of elastic WIMP-nucleus scattering, CRESST-II is largely sensitive to coherent (spin-independent) interactions, because of the earlier mentioned  $A^2$  enhancement. However one of the W isotopes ( $^{183}\text{W}$ ) has a net nuclear spin, and occurs with a natural abundance of 14.4% providing some sensitivity to spin-dependent interactions. The coherent (spin-independent) WIMP-nucleon scattering cross section has been constrained by data from two detector modules taken during the prototyping phase of the CRESST-II experiment and from two detector modules taken during the commissioning phase of the new setup. Figure 2.9 shows data from the latter after an exposure of about three months. In the area below the dashed black curve 90% of all nuclear recoils, and below the solid red curve 90% of the tungsten recoils are expected. Figure 2.10 shows the upper limit for the coherent (spin-independent) WIMP-nucleon scattering cross section that can be derived from this data.

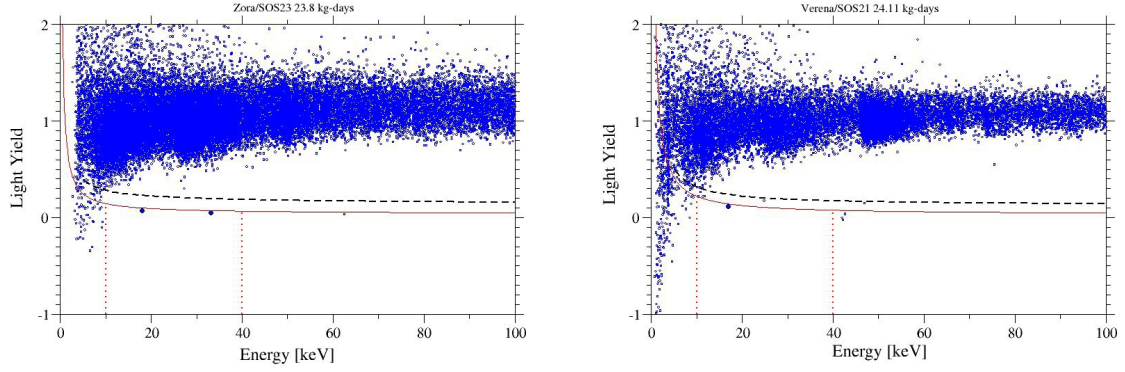


**Fig. 2.9:** Data from two detector modules taken during the commissioning run of CRESST-II. Below the dashed black curve 90% of all nuclear recoils, and below the solid red curve 90% of the tungsten recoils are expected. The heavy black dots show the events in the "tungsten recoils" acceptance region.

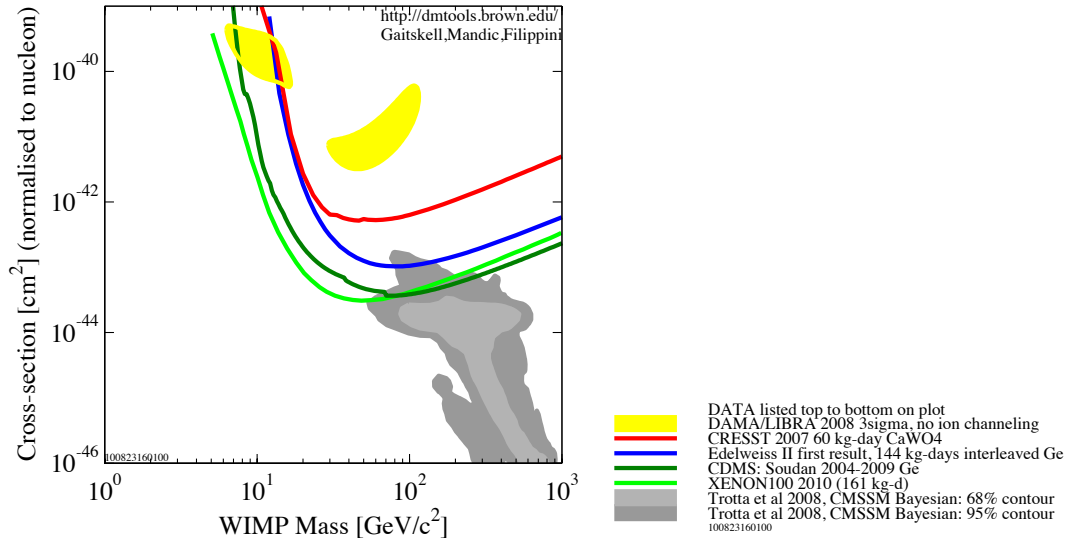


**Fig. 2.10:** Coherent (spin-independent) scattering cross section exclusion limit derived from the data of figure 2.9. For comparison the limits from other experiments and the range predicted by some supersymmetry models are also shown.

### 2.5.2 Current Run

Another WIMP scenario is the model of inelastic dark matter (iDM) [39], which is appealing because it can reconcile the annual modulation signal observed by DAMA/LIBRA and the null results of other experiments including CDMS and XENON-10 [40]. In addition, it can also explain excess fluxes in cosmic radiation observed by indirect DM searches [41]. In this model the WIMP has to make a transition to an excited state in the scattering process, where the splitting energy of the excited level  $\delta$  is assumed to be  $\mathcal{O}(100\text{keV})$ . The available energy  $E_{CM}$  in the center of mass for this splitting is  $E_{CM} = 1/2\mu v^2$  with the reduced mass  $\mu$  and the relative velocity  $v$  of the dark matter particles with respect to the target nucleus. With interactions in a heavy target with a large reduced mass  $\mu$  a large energy  $E_{CM}$  is available to excite internal states of the WIMP. Thus, the CRESST-II experiment, with tungsten as the heaviest target nucleus used in any direct WIMP search today, places the most stringent constraints on coherently (spin-independent) interacting iDM.

In the current run of CRESST-II 18 detector modules are installed of which 10 are operable and taking data since July 4th 2009. The analysis of the collected data is still in progress. Preliminary results of this data analysis have been used to constrain iDM models (see figure 2.11). For splittings  $\delta = 80 - 140\text{keV}$  the allowed DAMA/LIBRA region for coherent (spin-independent) scattering is fully excluded by the present CRESST-II data. This makes coherently interacting iDM seem a highly unlikely explanation for the DAMA/LIBRA modulation.

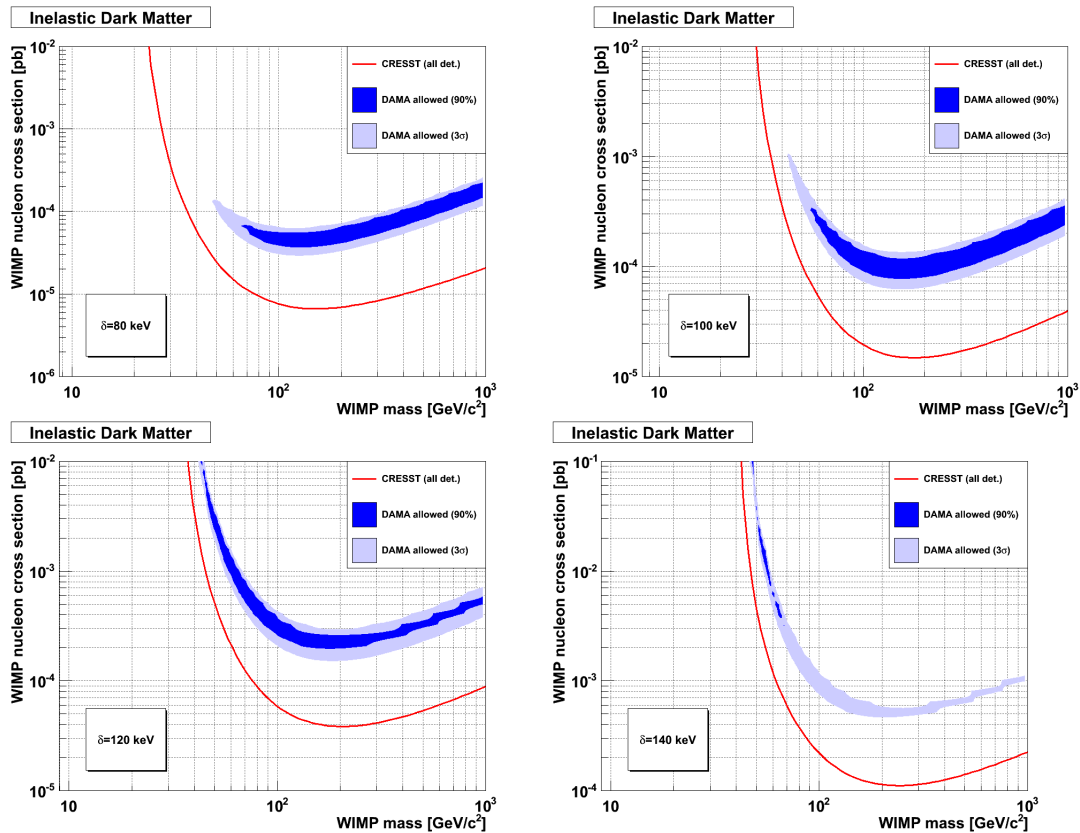


**Fig. 2.11:** Preliminary coherent (spin-independent) scattering cross section exclusion limits from the current run of CRESST-II for iDM models with different splittings  $\delta$ . For splittings  $\delta = 80 - 140 \text{ keV}$  the allowed DAMA/LIBRA region is fully excluded by the present CRESST-II data.

Recently, there has been some excitement regarding what may be hints of direct dark matter detection in addition to DAMA/LIBRA. The CoGeNT experiment based on an ultra low-noise Ge detector with a very low energy threshold, operated underground (2100 m.w.e.), has found an excess of events at low recoil energies [42]. These events may be explained by DM particles with a mass in the  $\sim 7 - 11 \text{ GeV}$  range. This observation can be put in agreement with the modulation observed by DAMA/LIBRA [43]. In addition, two events observed by the CDMS-II [44] and one by the EDELWEISS-II [45] experiments just above threshold might also hint towards a light DM candidate. However, the null results of XENON-100 (and XENON-10) [46, 47] severely challenge the light WIMP scenario (see figure 2.12) but there is some controversy about their calibration for low energy nuclear recoils [48, 49, 50].

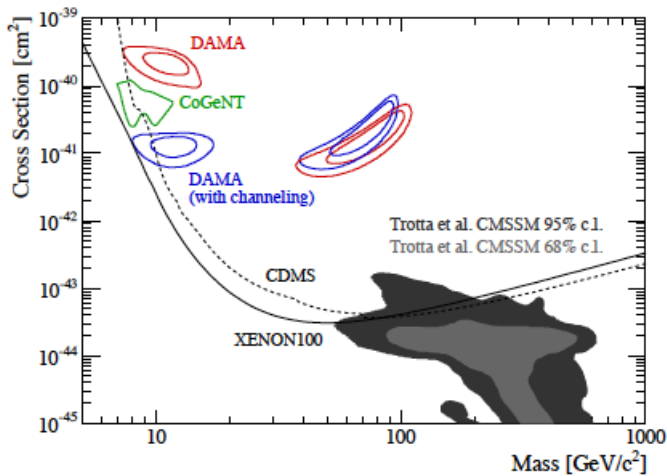


**Fig. 2.12:** Coherent (spin-independent) scattering cross section exclusion limits from XENON-100 and CDMS-II together with the allowed DAMA/LIBRA and CoGeNT regions [47]. The limit from XENON-100 excludes the region from DAMA/LIBRA and CoGeNT that are interpreted as the scattering caused by light WIMPs. However, there is some controversy regarding the calibration of low-energy nuclear recoils in XENON-100.

The preliminary data analysis of the current run of CRESST-II shows some events in the oxygen nuclear recoil band (see figure 2.13). Their rate in all detector modules agrees within statistics. These events could be caused by light ( $\sim 10\text{GeV}$ ) WIMPs which would mainly scatter off oxygen in the energy window from 10 – 40keV (see figure 2.14). However, at present it can *not* be excluded that these events are due to neutrons.

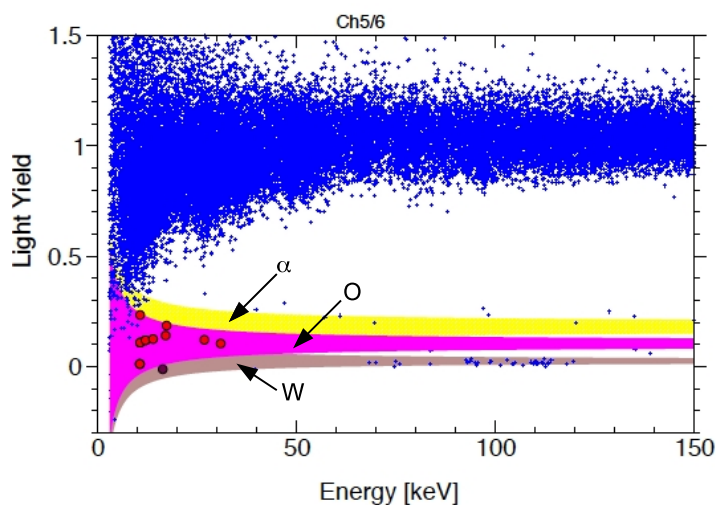


**Fig. 2.13:** Present data of a CRESST-II detector module. The magenta colored area is the oxygen band, where 80% of the oxygen recoils are expected (90% below the upper and 10% below the lower end). Tungsten and alpha bands are shown in brown and yellow, respectively.

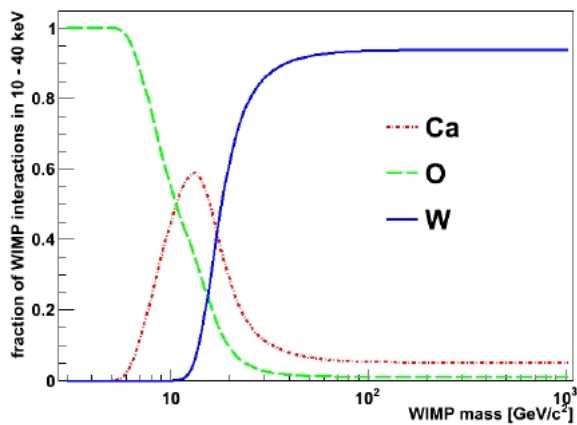


**Fig. 2.14:** Fraction of WIMP interactions in  $CaWO_4$  for recoil energies from 10–40 keV in dependence of the WIMP mass. Light WIMPs with a mass  $< 10 GeV$  would mainly scatter off oxygen.



## Chapter 3

# The EURECA Experiment

For future direct dark matter searches it is important to upscale the absorber mass to further explore the SUSY parameter space. A planned project is the European Underground Rare Event Calorimeter Array (EURECA), which several collaborations of present direct detection experiments (CRESST, EDELWEISS, ROSEBUD) have joined. The total absorber mass will be  $100\text{kg} - 1\text{ton}$ . The installation will take place in the Laboratoire Souterrain de Mondane (LSM) (4800m.w.e.) in France. EURECA is planned to have multiple targets and multiple discrimination techniques (phonon-light, phonon-charge) [51]. It is further expected that the target will be equipped with transition edge sensors as well as NTD Ge thermistors. The advantage of multiple targets is that the experiment can be sensitive to light and heavy WIMPs as well as coherent (spin-independent) and spin-dependent interactions. In addition, it will be able to confirm the  $A^2$ -scaling and therefore to determine the scattering cross section in case of a positive signal. The present experiments that have joined this collaboration can be considered as R&D for this project. To match the challenges of the large detector mass, the reproducibility of scintillating crystals with high radiopurity, large light output and good phonon properties is an important issue.

The excavations for a new lab at the LSM that will host the EURECA experiment are planned for 2011 (see figure 3.1). The experiment will employ two individual cryostats to allow changes on one setup while the other is running (see figure 3.2). The detectors will be shielded by  $\sim 3\text{m}$  of water. The inside of the water tanks will be equipped with photomultiplier tubes acting as an active Cherenkov veto. The main parts of the  $^3\text{He}-^4\text{He}$  dilution refrigerator will be placed outside the tanks to reduce radioactive contamination. The pumping system will be placed in a separate cave to avoid disturbances of the detectors from microphonics. The detector modules are planned to consist of closely packed tower-like structures that can be exchanged without long interruptions (see figure 3.3).

### 3. The EURECA Experiment

---

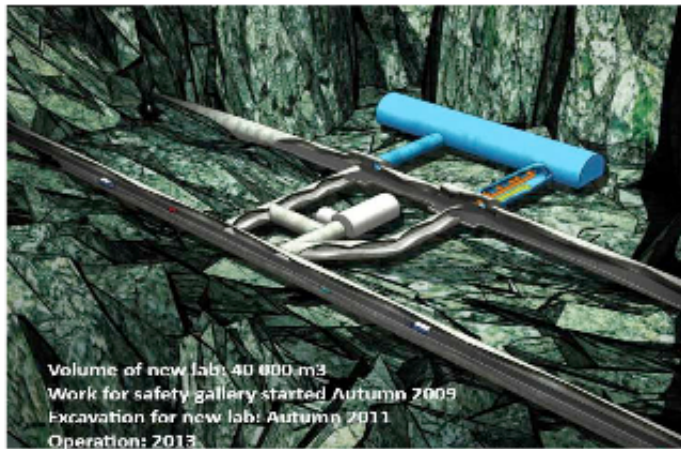


**Fig. 3.1:** Sketch of the LSM underground laboratory with the new extension (blue) that will host the EURECA experiment.

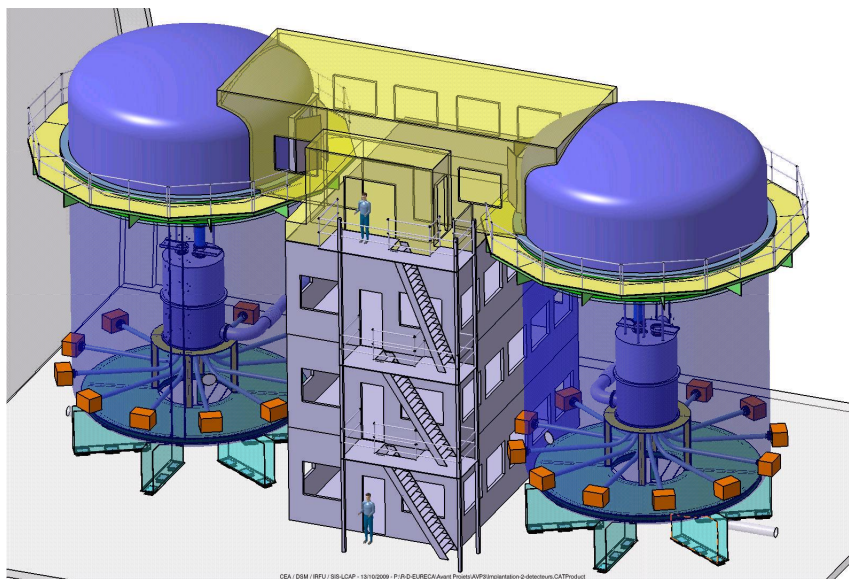


**Fig. 3.2:** Planned setup of the EURECA experiment with two individual cryostats submersed in water tanks which act as an active Cherenkov muon veto. The building in the middle provides the infrastructure and clean rooms for the detector installation.

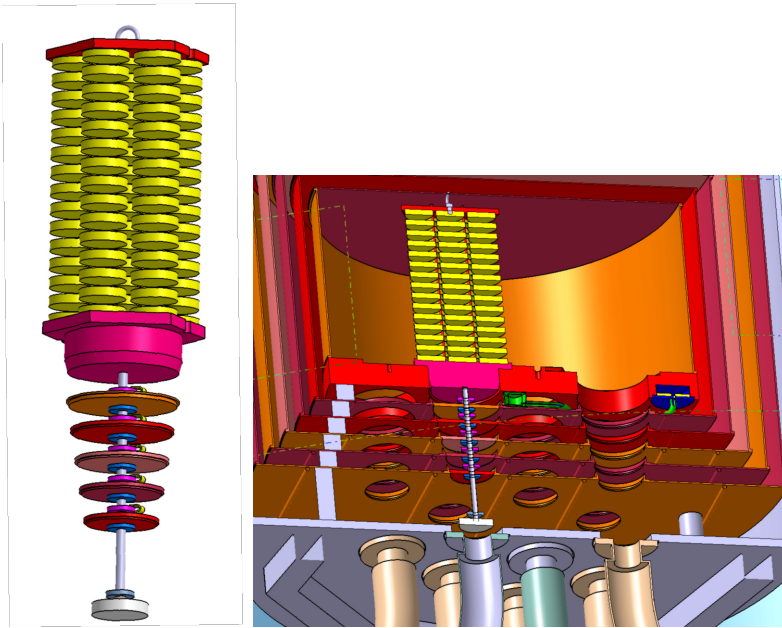


**Fig. 3.3:** Planned close packed tower-like detector modules of the EURECA experiment (left) and their installation in the cryostat (right).



# Chapter 4

## Scintillating $CaWO_4$ Crystals

$CaWO_4$  also known as scheelite (named after K. W. Scheele, who discovered the new element tungsten in the material [52]) is an interesting scintillator for cryogenic dark matter search because of the earlier mentioned  $A^2$  scaling for coherent interactions. In addition, the high density of  $6.1g/cm^3$  provides a large detector mass for the expected low event rate. A relatively high and constant light output at the operating temperature of cryogenic experiments makes it a suitable material for phonon-scintillation detectors.

### 4.1 Czochralski Growth Method

To ensure the availability of crystals meeting the requirements of the CRESST-II and future EURECA experiments,  $CaWO_4$  crystals are being produced with the Czochralski method at the crystal laboratory of the Technische Universität München (TUM). The Czochralski process is a method of crystal growth to obtain large single crystals. Coincidentally the first reported oxide material grown using the Czochralski technique was  $CaWO_4$  [53].

#### 4.1.1 Experimental Setup

In the Czochralski process a seed crystal with a well-defined orientation is mounted on a rod and lowered into the melt. This rod with the seed crystal is then pulled upwards and rotated at the same time (see figure 4.1). The crystallization takes place at the crystal-melt interface and the seed crystal's crystallographic orientation is transferred so that finally a large cylindrical single crystal can be extracted from the melt. The driving force behind the crystal-growth process is the temperature gradient at the phase boundary. In first approximation the equation of

thermal balance at the crystallization interface is given by [54]

$$\rho_s V Q = \lambda_s \left( \frac{dT}{dX} \right)_s - \lambda_l \left( \frac{dT}{dX} \right)_l \quad (4.1)$$

where  $\rho_s$  is the density of the crystal,  $V$  is the crystallization rate,  $Q$  is the latent crystallization heat,  $\lambda_s$  and  $\lambda_l$  are the thermal conductivities of the solid and the liquid phases, respectively.  $\left( \frac{dT}{dX} \right)_s$  and  $\left( \frac{dT}{dX} \right)_l$  are the respective temperature gradients in solid and liquid phases at the phase boundary. From equation (4.1) it appears that the maximum crystallization rate is obtained for a minimal gradient in the melt and a maximum gradient in the crystal.

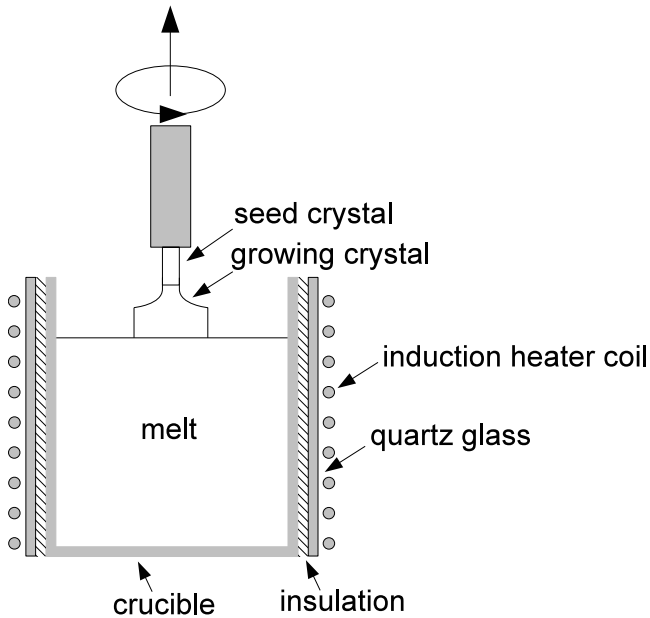


**Fig. 4.1:** Schematic drawing of the Czochralski setup. A seed crystal mounted on a rod is lowered into the melt. This rod is then pulled upwards and rotated at the same time. The crystallization takes place at the crystal-melt interface and the seed crystal's crystallographic orientation is transferred. Finally, a large cylindrical single crystal is extracted from the melt.

The newly installed Cyberstar Oxypuller 20-04 Czochralski furnace [55] at the crystal laboratory of the TUM (see figure 4.2) is equipped with a device which is continuously weighing the crystal during the growth process. The derivative of this measurement is the growth rate from which the growing software can compute the current diameter of the crystal. This allows automatic adjustment of the heating power by a PI controller so that the crystal matches pre-specified dimensions. The crucible with a diameter of  $80\text{mm}$  is made of rhodium and dedicated only to the

growth of  $\text{CaWO}_4$  crystals. The high oxidation resistance of rhodium allows to grow crystals under an atmosphere containing oxygen. The crucible is surrounded by a thermal insulation followed by a quartz-glass cylinder and an induction coil which is connected to a HF generator (see figures 4.3 and 4.4). The quartz glass avoids sparkovers between the induction coil and the crucible. A resistive after-heater located above the crucible lowers the risk of cleavage of the crystals due to thermal stress caused by temperature gradients that are induced after the crystal is separated from the melt.



**Fig. 4.2:** Newly installed Cyberstar Oxypuller 20-04 Czochralski furnace at the crystal laboratory of the TUM.

#### 4. Scintillating $\text{CaWO}_4$ Crystals

---

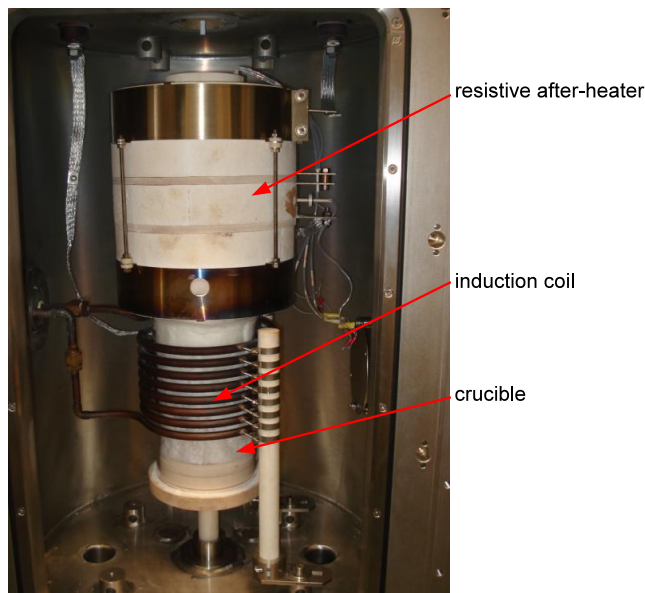


**Fig. 4.3:** Crucible surrounded by the induction coil which is connected to a HF generator. A resistive after-heater located above the crucible lowers the risk of cleavage of the crystals due to thermal stress originating from temperature gradients.

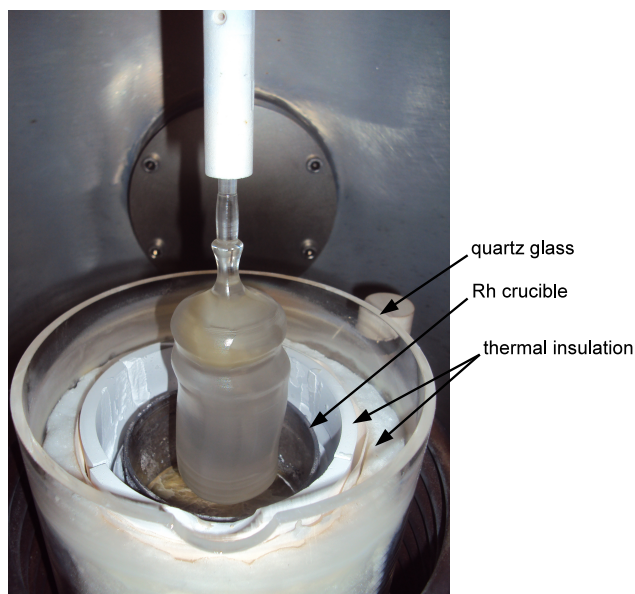
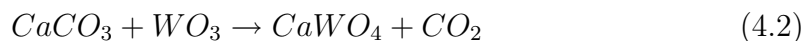


**Fig. 4.4:** Ingot "Hesso" before the extraction from the furnace. The picture shows the rhodium crucible (with the residual melt) surrounded by thermal insulation and a quartz-glass cylinder.

### 4.1.2 Growth Process

The following paragraph describes the growth process in more detail.

The  $CaWO_4$  powder for the melt is prepared by heating  $CaCO_3$  and  $WO_3$  under air at  $1250^\circ C$ :



The raw materials are carefully selected to ensure a high radiopurity of the crystals (see section 6.5). The rhodium crucible containing the  $CaWO_4$  powder or the solidified melt from the last growth is heated via the induction coil to a temperature slightly above the melting point  $T_m \approx 1600^\circ C$ . When all of the  $CaWO_4$  has melted a small cylindrical seed crystal is manually lowered into the melt. After that the control of the process is turned over to the computer. Before growing, the dimensions of the crystal to be grown have to be entered into the software that controls the process. In addition, the pulling and rotation speeds as well as the proportional and integral terms for the controller of the heating power have to be specified for different positions along the crystal and are changed linearly in between these positions. The challenge is to find the right recipe for these parameters which is mainly based on experience. During the growth a constant flow of a mixture of 99%  $Ar$  and 1%  $O_2$  is maintained inside the furnace. This avoids grey coloring due to an oxygen deficiency of the crystals (see figure 4.5). In addition, crystals with oxygen vacancies have a lower light yield since the luminescence mechanism is related to the  $WO_4^{2-}$  anion (see section 4.2). When the growth process is finished the crystal is manually pulled up into the after-heater which is then stabilized at a temperature of  $1200^\circ C$ . After the crystal has been annealed for 12 hours the after-heater is slowly ( $\sim 100^\circ C/h$ ) ramped down. Thereafter the ingot can be extracted from the furnace and is ready for further processing (mechanical treatment or annealing). The seed crystal can be cut from the ingot and used again.

$CaWO_4$  has a body-centered tetragonal crystal lattice (space group:  $I4_1/a$ ) [52]. The unit cell is shaped like a rectangular prism with a square base and sides of lengths  $a = 5.24\text{\AA}$  and  $c = 11.37\text{\AA}$  (see figure 4.6). It is built of  $Ca^{2+}$  ions surrounded by  $WO_4^{2-}$  tetrahedra. Due to the 4-fold symmetry of this crystal structure and the different growth rates for different crystal directions the ingot obtained from the melt is not completely cylindrical but slightly block shaped (see figure 4.7).

#### 4. Scintillating $\text{CaWO}_4$ Crystals

---



**Fig. 4.5:** Ingot "Hermann II" grown under pure  $N_2$  atmosphere. The lack of atmospheric oxygen leads to an oxygen deficiency and grey coloring of the crystal.

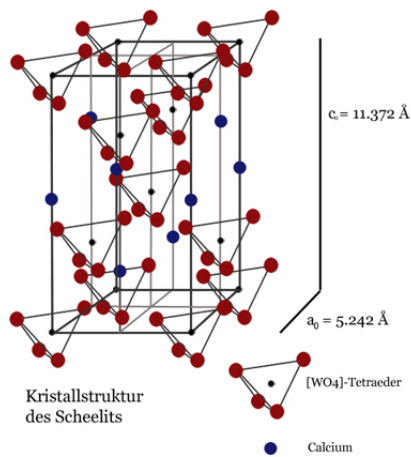


**Fig. 4.6:** The crystal lattice of  $\text{CaWO}_4$ . The unit cell is shaped like a rectangular prism with a square base and is built of  $\text{Ca}^{2+}$  ions and  $\text{WO}_4^{2-}$  tetrahedra [56].



**Fig. 4.7:** Part of the grown ingot "Rudolph I". The ingot is not cylindrical but slightly block shaped which can be attributed to the 4-fold symmetry of the crystal lattice and the resulting growth anisotropy.

### 4.1.3 Grown Crystals

During this thesis several  $CaWO_4$  crystals have been produced in the setup described above (see table 4.1). Figure 4.8 shows pictures of the produced ingots after they were extracted from the furnace.

Apart from "Friedrich I" all ingots have been annealed under an oxygen atmosphere for 72 hours at  $1450^\circ C$  at the Walther Meissner Institut in Garching. In this process oxygen can diffuse inside the crystal and fill vacancies. This can increase the light output by up to a factor of 2 [21]. The crystal "Hermann VI" showed some fractures when it was extracted from the furnace. Investigation of the crystal with a Laue camera revealed that at some point during the growth a different crystal orientation was established which was probably caused by a too rapid growth rate. The mechanical tensions arising from such a lattice defect can lead to the cleavage of the crystal.

In addition, some growth defects were found in all ingots which can include solid and gaseous enclosures, dislocations or point defects [57, 58, 59]. These appear mostly at the "tail" and "shoulder" of the crystal where the growth parameters are continuously changed. In general, the formation of such defects can be reduced by low pulling rates, good temperature control, an atmosphere with a high oxygen concentration, and a high purity of the starting material [57, 58, 59].

The crystal "Hesso" has a slightly curved shape along its symmetry axis which can

#### 4. Scintillating $\text{CaWO}_4$ Crystals

---

be assigned to the fact that the crucible was not exactly centered at the pulling axis. In addition, the crystal showed a slight yellow-green coloring at the "shoulder". This coloration can be attributed to the presence of tungsten trioxide ( $\text{WO}_3$ ) in the crystal [60, 61]. In addition, the "tail" of the crystal was colored grey which can be assigned to a slight reduction due to the lack of atmospheric oxygen. After annealing under oxygen atmosphere the discolored regions became optically clearer, however the crystal still showed a light green hue.

From the produced ingot "Friedrich I" several crystals with different shapes were cut (see table 4.2 and figure 4.9). For these crystals only parts of the ingot that were optically clear and exhibited no growth defects were used. All surfaces of the crystals were polished to optical quality. Under close inspection though it was observed that the crystals named "Sheldon II" and "Sheldon IV" as obtained from the crystal laboratory do show some minor cloudy enclosures.

From the ingot "Hesso" it was unfortunately not possible to cut a crystal with dimensions as those used in CRESST-II since it showed several fractures during the mechanical treatment.

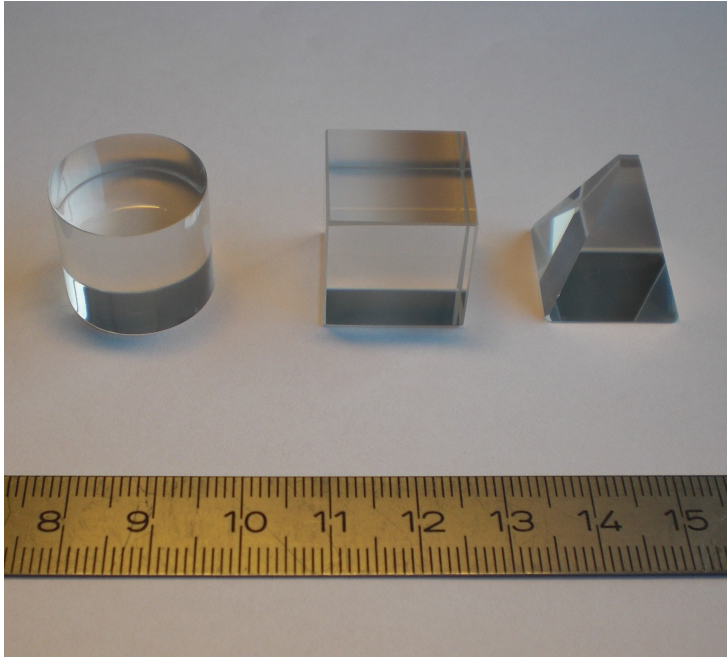


**Fig. 4.8:**  $\text{CaWO}_4$  ingots "Hermann VI", "Friedrich I" and "Hesso" (from top to bottom) produced with the Czochralski furnace at the crystal laboratory of the TUM. Details are given in table 4.1.

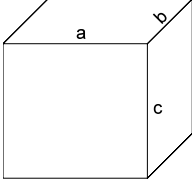
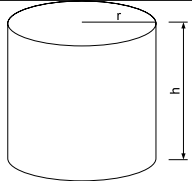
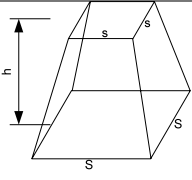
name	mass	dimensions
Hermann VI	328g	$d \approx 25\text{mm}, h \approx 120\text{mm}$
Friedrich I	252g	$d \approx 25\text{mm}, h \approx 90\text{mm}$
Hesso	786g	$d \approx 43\text{mm}, h \approx 100\text{mm}$

**Tab. 4.1:** Properties of the  $\text{CaWO}_4$  ingots produced with the Czochralski furnace at the crystal laboratory of the TUM.

#### 4. Scintillating $\text{CaWO}_4$ Crystals



**Fig. 4.9:** Differently shaped  $\text{CaWO}_4$  crystals cut from the ingot "Friedrich I". Details are given in table 4.2.

name	shape	mass	dimensions
Sheldon II		35.1g	$a = 17.9\text{mm}, b = 17.8\text{mm}, c = 18.1\text{mm}$
Sheldon III		31.3g	$r = 9.8\text{mm}, h = 17.1\text{mm}$
Sheldon IV		14.5g	$s = 2.9\text{mm}, S = 17.7\text{mm}, h = 18.2\text{mm}$

**Tab. 4.2:** Properties of the differently shaped  $\text{CaWO}_4$  crystals cut from the ingot "Friedrich I".

## 4.2 Review of Scintillation Properties

$CaWO_4$  was one of the first discovered inorganic scintillators. In 1896 Edison wrote in a telegram to Lord Kelvin that he "just found calcium tungstate properly crystallised gives splendid fluorescence with Röntgen rays" [62].

The scintillating mechanism in inorganic scintillators can be divided into different stages [63]:

1. Absorption and generation of primary "hot" electrons (e) and holes (h)
2. Production of numerous secondary electronic excitations (e-h pairs, plasmons, excitons etc.)
3. Thermalization of secondary e-h pairs to the band gap energy
4. Energy transfer to luminescent centers and their excitation
5. Relaxation of luminescent centers under emission of fluorescent light

While the luminescent centers are usually dopants in the crystal,  $CaWO_4$  is a self-activated scintillator. The luminescence originates from electronic transitions between oxygen and tungsten within the  $WO_4^{2-}$  anion interpreted as the recombination of self trapped excitons. The emission shows a maximum at  $\sim 420nm$  at  $300K$  (RT) when excited with UV light (excitation peak at  $\sim 260nm$ ). In addition, one can observe a green and in some crystals also a red luminescence. The green band is attributed to the extrinsic emission from oxygen deficient sites ( $WO_3$  Schottky defects) while the red band is believed to originate from higher tungstate complexes [64]. The luminescence of  $CaWO_4$  exhibits an exponential decay with a fast and a slow component with respective time constants of  $\sim 1\mu s$  and  $\sim 9\mu s$  at room temperature (RT) [65]. Measurements of the light yield of  $CaWO_4$  crystals from different suppliers for CRESST-II have shown variations up to a factor of 2 [66]. While literature gives a value for the light yield of 6000ph/MeV at RT [54], a measurement of a crystal from a supplier for CRESST-II gave a value of about 16,000ph/MeV at RT [67]. However, in light-yield measurements a large fraction of scintillation photons can remain trapped inside the crystal (see section 4.3). A measurement of another crystal from the same supplier using a combination of experiments and MC simulations (see section 6.2) that also accounts for trapped light gave a value of about 23,000ph/MeV at RT [68]. The light yield also depends on the type of exciting particle (see also section 2.3) and shows some non-proportionality<sup>1</sup> [67, 69].

---

<sup>1</sup>The light yield shows an increase with increasing energy and some quenching for low-energy gamma events with respect to electron events of the same energy.

Most of these luminescence characteristics are dependent on temperature. The slow decay-time constant increases significantly at lower temperatures and was measured to be  $\sim 300\mu s$  and  $\sim 500\mu s$  at  $20mK$  under excitation with  $\alpha$  and  $\gamma$  particles, respectively. The value of the fast decay-time constant though stays roughly the same and the corresponding amplitude becomes highly dominant at this temperature.

The light yield is also dependent on temperature. At temperatures  $> 20K$  the light yield decreases as temperature increases and above  $200K$  is dominated by thermal quenching.<sup>2</sup> At temperatures below  $10K$  the light yield was found to be constant down to  $20mK$  [65]. At these temperatures in the operating range of cryogenic detectors the light yield is increased by a factor of  $\sim 1.82$  compared to RT.

### 4.3 Light Trapping in Cylindrical Crystals

The propagation of scintillation light can be described by geometrical optics where the intersection of a beam of light on a specular (mirror-like) surface is described by Snell's law [71]:

$$\frac{\sin \theta_1}{\sin \theta_2} = \frac{n_2}{n_1} \quad (4.3)$$

Here  $\theta_1$  and  $\theta_2$  are the incident angles and  $n_1$  and  $n_2$  the refractive indices of the two media. If a beam of light hits the surface to an optically less dense medium at an angle greater than the critical angle

$$\theta_c = \arcsin\left(\frac{n_2}{n_1}\right) \quad (4.4)$$

the light is totally reflected.

Equation 4.4 shows that the high refractive index<sup>3</sup>  $n_{cawo} \approx 1.95$  of  $CaWO_4$  at  $2.8eV$  [72] (peak position of the scintillation spectrum at low temperatures [35]) leads to a small critical angle

$$\theta_c = \arcsin\left(\frac{1}{n_{cawo}}\right) \approx 30.85^\circ \quad (4.5)$$

for the crystal-air interface. Together with the high symmetry of the cylindrical shape of the currently used crystals this leads to a high probability that scintillation

---

<sup>2</sup>The decrease of luminescence efficiency at higher temperatures due to the increased probability of non-radiative transitions is known as thermal quenching [70].

<sup>3</sup>It should be stated that  $CaWO_4$  is weakly birefringent with a maximum birefringence  $\delta = n_{eo} - n_o = 0.017$  where  $n_o$  is the ordinary and  $n_{eo}$  the extraordinary refractive index.

photons are internally reflected an indefinitely large number of times, i.e. they remain trapped inside the crystal. The fraction  $T_N$  of all photons confined in this way as a function of the emission point in an ideal,<sup>4</sup> cylindrical scintillator was calculated in [73].  $T_N$  is independent of the diameter-to-length ratio of the cylinder and depends only on the radial position of the emission point while it is independent of the position along the cylinder axis. It can be calculated by the following equation [73]

$$T_N(d/R) = \cos \theta_c - \cos \theta_b - H(\theta_a, \theta_b) \quad (4.6)$$

$$\theta_a = \pi/2 - \theta_c \quad (4.7)$$

$$\theta_b = \begin{cases} \arcsin\left(\sqrt{\frac{1-1/n_{cawo}^2}{1-d^2/R^2}}\right) & \text{for } d/R < 1/n_{cawo} \\ \pi/2 & \text{for } d/R \geq 1/n_{cawo} \end{cases} \quad (4.8)$$

$$H(v, w) = 2/\pi \int_v^w \sin \theta \arcsin\left(\sqrt{1 - \frac{n_{cawo}^2 - 1}{n_{cawo}^2 \sin^2 \theta} R/d}\right) d\theta \quad (4.9)$$

Here  $d$  is the distance from the cylinder axis and  $R$  the cylinder radius.

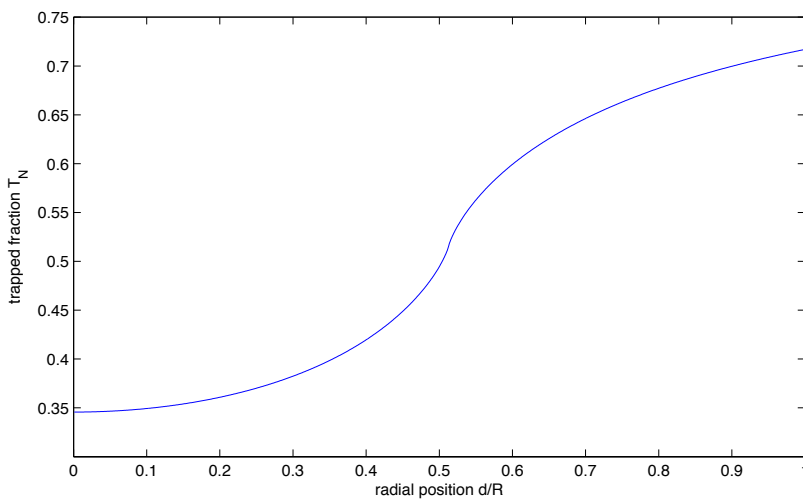


**Fig. 4.10:** Fraction  $T_N$  of trapped light in an ideal, cylindrical scintillator with refractive index 1.95 as a function of normalized distance  $d/R$  from the cylinder axis.

<sup>4</sup>This means that neither absorption nor scattering is considered and that all surfaces are specular (mirror-like).

Figure 4.10 shows the fraction  $T_N$  of trapped light as a function of the radial position, calculated by equation (4.6) for  $n_{cawo} = 1.95$ . About 35% of the scintillation photons produced at the center of the cylinder remain trapped. This fraction increases with distance from the cylinder axis, at the border it is  $\sim 72\%$ . It should be noted that the dependence on the radial position comes only from the contribution of photons that escape the circular surface of the cylinder. The fraction of light escaping the planar surfaces is independent with respect to the point of emission inside the cylinder and has a constant value of

$$1 - \sqrt{1 - \frac{1}{n_{cawo}^2}} \approx 14\% \quad (4.10)$$

In real crystals photons cannot travel infinite path lengths because a beam of light is attenuated on its way by scattering and absorption:

$$\alpha_{att} = \alpha_{scat} + \alpha_{abs} \quad (4.11)$$

Here  $\alpha_{scat}$  is the scattering coefficient,  $\alpha_{abs}$  the absorption coefficient and  $\alpha_{att}$  the attenuation coefficient of the material.

However, light can be absorbed before it can escape the crystal (quasi trapping). Absorption and scattering are competing processes, while a higher value  $\alpha_{abs}$  increases the fraction of (quasi) trapped light, scattering leads to an "untrapping" and a higher value of  $\alpha_{scat}$  leads to an increased light output [66, 68]. Earlier experiments came to the conclusion that in the  $CaWO_4$  crystals for CRESST-II scattering dominates over absorption so that no (quasi) trapping exists [66], hence the cylindrical shape was accepted. However, the crystals used in CRESST-II come from different suppliers and exhibit very different optical properties. Measurements of  $CaWO_4$  crystals from different suppliers for CRESST-II have shown that the scattering and absorption coefficients can also have comparable values [68] leading to a reduced light output (see section 5.1).

## 4.4 Strategies to Improve the Light Collection

### Surface roughening of the crystal

Trapping can be partially overcome by roughening a surface of the crystal. Since every photon in a beam of light will strike the roughened surface at a random incident angle, it prevents photons from traveling infinite path lengths and leads to an "untrapping" similar to scattering. In CRESST-II the surface facing the light detector is roughened to about  $10\mu m$ , which is also applied to homogenize

the light output that is otherwise focussed at the beveled edges of the cylinder<sup>5</sup> (see figure 4.11).

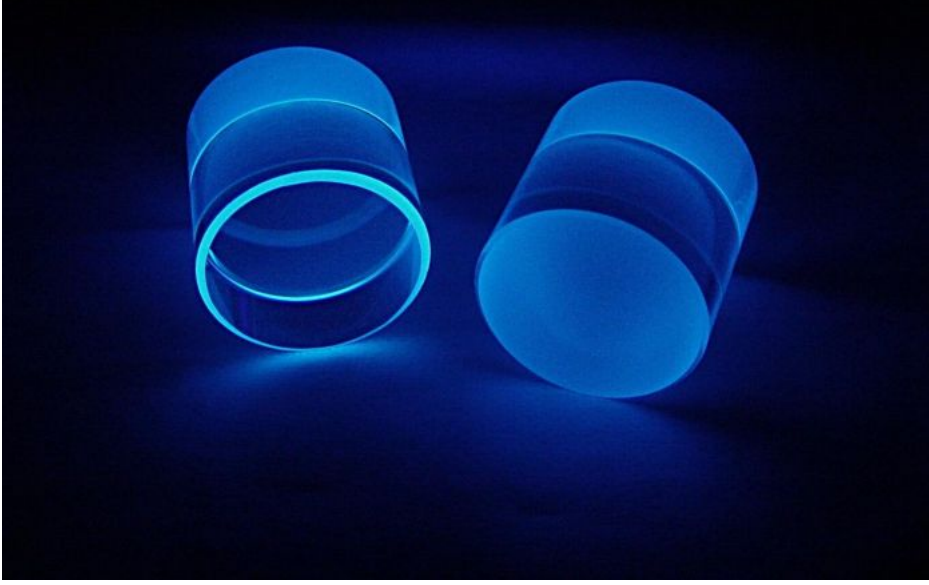


**Fig. 4.11:** Two  $CaWO_4$  crystals under UV irradiation. The planar side of the crystal on the right is roughened which homogenizes the light output that is otherwise focussed at the beveled edges (left crystal).

In addition to "untrapping" roughening may also lead to an increased transmission through the roughened surface depending on the angular distribution of the scintillation light and of the roughened surface. The reflectivity  $R$  of the crystal-air interface for unpolarized light in dependence of the incident angle  $\theta$  can be calculated by the Fresnel equations [71]

$$R(\theta) = (R_s(\theta) + R_p(\theta))/2 \quad (4.12)$$

$$R_s(\theta) = \left[ \frac{n_{cawo} \cos \theta - \sqrt{1 - (n_{cawo} \sin \theta)^2}}{n_{cawo} \cos \theta + \sqrt{1 - (n_{cawo} \sin \theta)^2}} \right]^2 \quad (4.13)$$

$$R_p(\theta) = \left[ \frac{n_{cawo} \sqrt{1 - (n_{cawo} \sin \theta)^2} - \cos \theta}{n_{cawo} \sqrt{1 - (n_{cawo} \sin \theta)^2} + \cos \theta} \right]^2 \quad (4.14)$$

Here  $R_s$  and  $R_p$  are the reflectivities for s-polarized (perpendicular to the plane of incidence) and p-polarized (parallel to the plane of incidence) light, respectively.

<sup>5</sup>The beveling is applied to minimize the risk of damages to the crystal on the otherwise sharp edges.

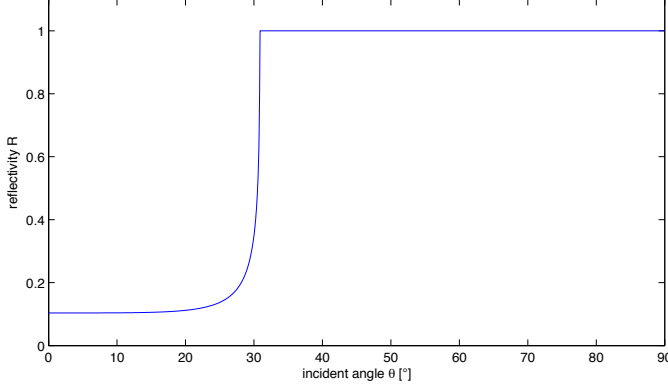


**Fig. 4.12:** Reflectivity for unpolarized light at the crystal-air interface in dependence of the incident angle calculated from equation (4.12) for  $n_{\text{cawo}} = 1.95$ . The step rise of the reflectivity at an incident angle of  $\theta \approx 31^\circ$  is due to total internal reflection.

Figure 4.12 shows the graph of equation (4.12) for  $n_{\text{cawo}} = 1.95$ . The step rise of the reflectivity at an incident angle of  $\theta \approx 31^\circ$  is due to total internal reflection. The fraction  $F$  of scintillation light that is transmitted through a surface can then be calculated as

$$F = 1 - \frac{1}{\pi/2} \int_0^{\pi/2} R(\theta) S(\theta) L(\theta) d\theta \quad (4.15)$$

where  $S(\theta)$  is the angular distribution of the roughened surface.  $L(\theta)$  is the angular distribution of incident photons at the surface. If one assumes that the angular distribution of the scintillation light at the surface is uniform (i.e. every incident angle has the same probability) then this means  $L(\theta) = 1$ .

In case of a specular (mirror-like) surface also the angular distribution  $S(\theta) = 1$ . The fraction  $F$  of transmitted scintillation light can then be calculated as

$$F = 1 - \frac{1}{\pi/2} \int_0^{\pi/2} R(\theta) d\theta = 29.7\% \quad (4.16)$$

A roughened surface can be considered as diffusely reflecting. For diffuse reflection often the model of Lambertian reflection is used [74]. The radiant intensity observed from a "Lambertian" surface is directly proportional to the cosine of the angle between the observer's line of sight and the surface normal. Hence for a roughened surface an angular distribution  $S(\theta) = \cos \theta$  can be assumed. The fraction  $F$  of transmitted light can then be calculated as

$$F = 1 - \frac{1}{\pi/2} \int_0^{\pi/2} R(\theta) \cos \theta d\theta = 64.7\% \quad (4.17)$$

This means that according to the assumptions made roughening increases the fraction  $F$  of light transmitted through the roughened surface by a factor of  $\sim 2$ . Experimentally an increase of the light output of  $\sim 50\%$  has been measured after roughening of the planar surface facing the light detector [21].

One disadvantage of roughening of the crystal's surface, however, is that it can also worsen the detector's energy resolution in the *phonon* channel since it increases the effective surface. This causes additional inelastic scattering of non-thermal phonons before they can thermalize in the TES. With the specified roughness though no degradation of the phonon detector was observed in measurements in the CRESST setup [21].

### Suitable shaping of the crystal

The easiest way to reduce internal trapping is a suitable shaping of the scintillator. The effects of geometric modifications of scintillators on the light collection have been well studied for nuclear medicine and high energy physics (HEP) [75, 76, 77, 78, 79, 80].

One possibility to increase the light collection is to give the crystal a taper-shaped axial cross section (see figure 4.13). This has a "focussing" effect since the light is mainly reflected towards the larger end face and strikes it at a smaller angle which reduces the probability of total internal reflection [75]. Thus, with the light detector facing this end face an increased light collection can be accomplished. However, since more reflections on the side walls lead to a smaller incident angle on the large end face (facing the light detector) the light collection in a taper-shaped scintillator is not uniform with respect to the position of the scintillation event inside the crystal but favors light produced near to the small end face (opposite to the light detector). This spatial dependence of the light collection worsens the detector's energy resolution in the light channel. Beveling the crystal at a larger angle  $\alpha$  (while keeping the size of the large end face constant) reduces the fraction of light that can escape through the smaller end face opposite to the light detector and decreases the incident angle on the large end face (see figure 4.13). As this will increase the efficiency but also the non-uniformity of the light collection, it is difficult to choose the right angle of taper.

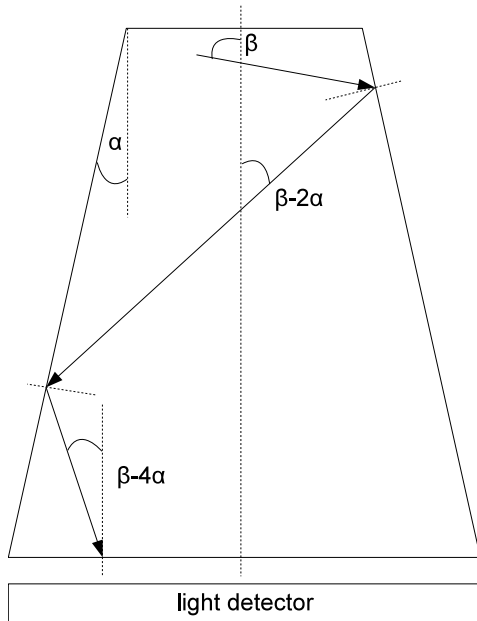


**Fig. 4.13:** Schematic drawing of the "focussing effect" in scintillators with a taper-shaped cross section. The scintillation light is mainly reflected towards the larger end face which is facing the light detector. The incident angle on this surface is reduced by a value that increases with the angle of taper  $\alpha$  and the number of reflections on the side wall.

### Improvement of the light detector

Apart from modifying the  $\text{CaWO}_4$  crystal, the sensitivity of the light channel can be increased by improving the light detector. It has recently been shown that using the Neganov-Luke [81, 82] amplification the signal-to-noise ratio of a cryogenic light detector can be improved by up to a factor of 10 [83]. In addition, black silicon is considered as a possible future material instead of SOS. Black silicon is obtained by etching of nano holes with a diameter that is much smaller than the photon wavelength, into the surface of a silicon waver [84]. This needle-like structure forms an effective medium with a continuously changing refractive index instead of a sharp optical interface. Therefore the reflectivity of the silicon waver is considerably reduced. At the peak position of the  $\text{CaWO}_4$  scintillation spectrum at low temperatures black silicon has an absorption of  $\sim 97\%$  in comparison to  $\sim 84\%$  for SOS [33]. In addition the absorption stays above 95% over a large range of wavelengths ( $\sim 200 - 800\text{nm}$ ) which is of particular importance if other scintillating materials than  $\text{CaWO}_4$  will be used.

# Chapter 5

## Monte Carlo (MC) Simulations

To study the trapping of light and the effects of differently shaped crystals on the light collection in a CRESST-like detector module two MC-simulation programs were established with GEANT4.

### 5.1 Light-Output Simulation

The first simulation was carried out to determine the light output of a cylindrical  $CaWO_4$  crystal and includes just a crystal with dimensions as those currently used in CRESST-II (40mm diameter and height) surrounded by vacuum. Running the simulation, scintillation events are generated at random positions inside the crystal. In each scintillation event a mean number of 10,000 photons (following a Poisson distribution) with a Gaussian energy spectrum, random linear polarizations and an isotropic angular distribution over a solid angle of  $4\pi$  are produced. All photons that are absorbed before they can escape the crystal are detected. The optical parameters used in the light output simulation are shown in table 5.1.

<b>CaWO<sub>4</sub> crystal</b>	
scintillation spectrum mean	2.8eV [35]
scintillation spectrum FWHM	0.56eV [35]
scattering length <sup>2</sup> $L_{scat} = \alpha_{scat}^{-1}$	16.4cm [68]
absorption length $L_{abs} = \alpha_{abs}^{-1}$	15.4cm [68]
refractive index <sup>3</sup>	1.95@2.8eV [72]
<b>vacuum</b>	
refractive index:	1

**Tab. 5.1:** Optical parameters used in the light-output simulation

GEANT4 is not capable of simulating birefringent materials, therefore the used refractive index is that for the ordinary beam calculated by the following dispersion formula [72]:

$$n^2 - 1 = \frac{2.5493 \cdot (\lambda/\mu m)^2}{(\lambda/\mu m)^2 - 0.1347^2} + \frac{0.92 \cdot (\lambda/\mu m)^2}{(\lambda/\mu m)^2 - 10.815^2} \quad (5.1)$$

The peak position and FWHM of the scintillation spectrum was taken from a measurement of a crystal from the Scientific Research Company (SRC) "Carat" (Lviv, Ukraine) under photoexcitation at  $8K$ . The scattering and absorption lengths were determined by a combination of experiments and MC simulations (see section 6.2) for a crystal from the same supplier. However, as the crystals for CRESST-II come from different suppliers these values can vary. For the CRESST-II reference crystal "Boris" only the ratio  $B = \alpha_{scat}/\alpha_{abs} = 4.3$  was determined. Such a higher value of  $B$  as compared to  $B = 0.9$  in table 5.1 results in a higher light output (see section 4.3). In [66] respective values of the absorption and scattering length of  $250cm$  and  $19.3cm$  were found with the conclusion that in such crystals no (quasi) trapped light exists. Experimentally it was shown that for these crystals geometrical modifications do not lead to a higher light output. If modifying the crystal shape is profitable will therefore depend on the crystal and its values  $L_{abs}$  and  $L_{scat}$ .

### 5.1.1 Results and Discussion

Tables 5.2-5.4 and figures 5.1-5.3 show the results of the simulation carried out with different values for  $L_{abs}$  and  $L_{scat}$ . In the simulation the fraction  $T$  of the energy of (quasi) trapped light<sup>1</sup> in each scintillation event is determined:

$$T = E_{abs}/E_{scint} \quad (5.2)$$

Here  $E_{scint}$  and  $E_{abs}$  are the total energies from photons that are produced and absorbed by the crystal in each scintillation event, respectively. In the following,  $\tau$  denotes the mean value of  $T$  and  $\sigma_\tau$  its standard deviation calculated from all simulated events (originating at different positions in the crystal):

$$\tau = \langle T \rangle \quad (5.3)$$

$$\sigma_\tau = \sigma(T) \quad (5.4)$$

---

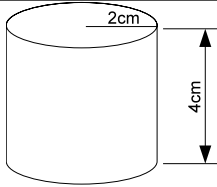
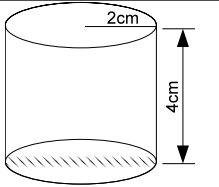
<sup>2</sup>The scattering implemented in GEANT4 is Rayleigh scattering.

<sup>3</sup>Dependent on the photon energy (see equation 5.1).

<sup>1</sup>In contrast to section 4.3 where the trapped fraction  $T_N$  of the number of photons was calculated, the trapped fraction  $T$  in the simulation is determined energy-wise.

The standard deviation  $\sigma_\tau$  arises mainly from the dependence of the fraction  $T$  of trapped light on the position of the scintillation event.<sup>2</sup> As a good crystal should have a high and uniform light output the values of  $\tau$  and  $\sigma_\tau$  should be small.

**No scattering and negligible absorption**

<b>crystal shape</b>		
<b>crystal surfaces</b>	all surfaces polished	one planar surface roughened
$\tau$	60.13%	8.59%
$\sigma_\tau$	11.73%	3.29%

**Tab. 5.2:** Results of the light-output simulation for a cylindrical crystal with  $L_{abs} = 500cm$  and no scattering. The dimensions of the crystal are similar to that used in CRESST-II. Roughened surfaces are indicated by the shaded area.  $\tau$  denotes the mean value of the fraction of (quasi) trapped light and  $\sigma_\tau$  its standard deviation. The latter arises mainly from the dependence of the fraction of trapped light on the position of the scintillation event.

<sup>2</sup>There is also a small contribution to  $\sigma_\tau$  from the statistical generation of the photons in a single scintillation event.

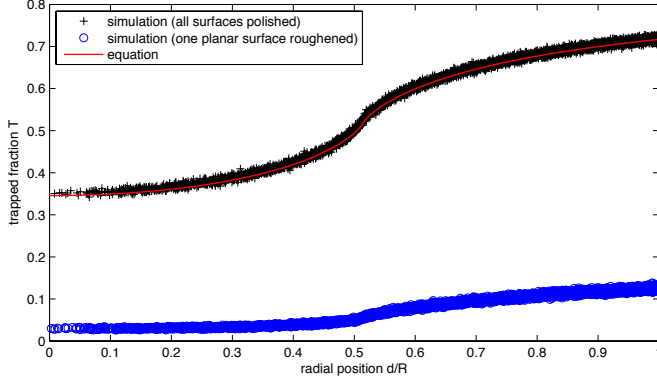


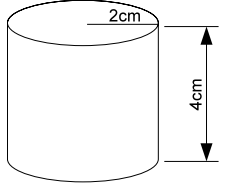
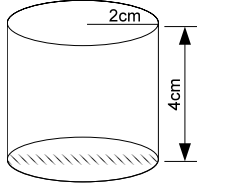
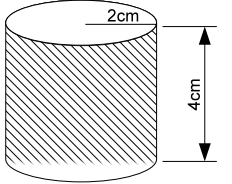
**Fig. 5.1:** Fraction of trapped light vs. the radial position in the cylindrical crystal with  $L_{abs} = 500cm$  and no scattering. For comparison, also the graph for  $T_N$  (solid line) depicted in figure 4.10 is shown that was calculated from equation 4.6. The curve fully matches the simulation when all surfaces of the crystal are polished. Roughening of one planar surface reduces the fraction of trapped light and its radial dependence. See also table 5.2.

At first the simulation was carried out without scattering and a large absorption length of  $500cm$ . Figure 5.1 shows the fraction  $T$  of (quasi) trapped light in dependence of the radial position  $d/R$  for all simulated scintillation events. For comparison, also the graph for  $T_N$  calculated from equation 4.6 and depicted in figure 4.10 is shown. It can be seen that in the case that all surfaces of the cylinder are polished the simulated events match the curve calculated from equation 4.6. However, the simulated events show a distribution of  $T$  because the simulation uses a Gaussian scintillation spectrum and a dispersive refractive index. Although the graph of  $T$  is symmetrical the mean value  $\tau \approx 60\%$  is slightly higher than the value of  $T$  at the radial position  $d/R \approx 0.5$  (see table 5.2). This results from the fact that the simulated events are uniformly distributed inside the crystal which means their number increases (linearly) with distance from the cylinder axis. This is shifting the mean value of  $T$  to a higher radial position.

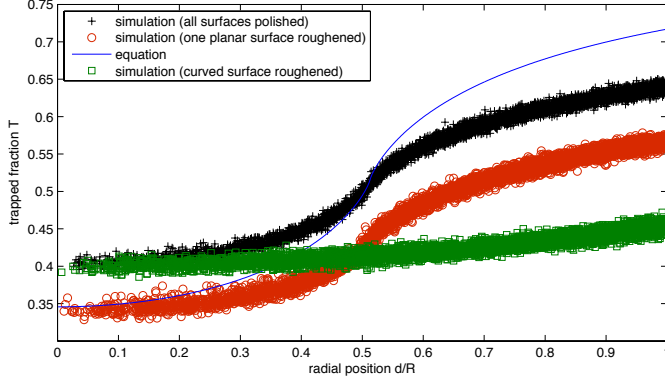
As mentioned in section 4.4, roughening of the crystal is known to decrease the amount of trapped light. In GEANT4 this was implemented with the "glisur" model, which assumes that a rough surface is a collection of "micro-facets". The normal vector of such a facet is indicated by the value of *polish*: When it is  $< 1$  a random point is generated in a sphere of radius  $r = 1 - polish$ , and the corresponding vector is added to the normal of the surface. For the simulations with a roughened surface a value  $polish = 0$  was chosen which means maximum roughness with the effective plane of reflection distributed according to  $\cos \alpha$ , where  $\alpha$  is the angle between the surface and the facet normal.

Figure 5.1 and table 5.2 also show the result of a simulation where one of the cylinder's planar surfaces was roughened. It can be seen that this reduces the mean fraction of trapped light to  $\tau \approx 9\%$ . In addition, the graph is flattened (i.e. a reduced radial dependence) which is reflected in the smaller value of the standard deviation  $\sigma_\tau$ . Some of the remaining trapped light can be assigned to the presence of absorption which is needed in the simulation that would otherwise run infinitely long. Without scattering and absorption the roughened surface will remove all of the trapped light that is not emitted exactly perpendicularly to the cylinder axis since it will eventually hit this surface at a random incident angle.

### Comparable absorption and scattering lengths

			
<b>crystal shape</b>			
<b>crystal surfaces</b>	all surfaces polished	one planar surface roughened	curved surface roughened
$\tau$	55.92%	48.45%	42.67%
$\sigma_\tau$	7.58%	7.49%	1.67%

**Tab. 5.3:** Results of the light-output simulation for a cylindrical crystal with  $L_{abs} = 15.4cm$  and  $L_{scat} = 16.4cm$ . For further details see caption of table 5.2.



**Fig. 5.2:** Fraction of trapped light vs. the radial position in the cylindrical crystal with  $L_{abs} = 15.4cm$  and  $L_{scat} = 16.4cm$ . When all surfaces remain polished the graph is flattened compared to the curve calculated from equation 4.6 due to the low scattering length implemented in the simulation. Roughening of one planar surface reduces the mean fraction of trapped light while its radial dependence is almost eliminated if the curved surface is roughened. See also table 5.3.

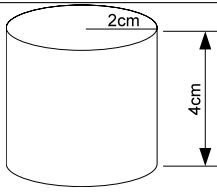
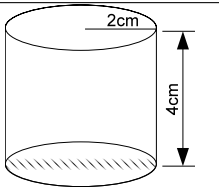
Figure 5.2 shows the fraction of trapped light versus the radial position if the values  $L_{abs} = 15.4cm$  and  $L_{scat} = 16.4cm$  are entered in the simulation. In case that all surfaces of the crystal are polished the fraction of trapped light for  $d/R \approx 0.5$  is roughly the same as calculated from equation 4.6 without scattering and absorption because of the similar values of  $L_{scat}$  and  $L_{abs}$ . However, because scattering reduces spatial dependencies of the light propagation inside the crystal the curve is a little flattened. The mean fraction of trapped light is  $\tau \approx 55\%$ .

The figure also shows the graph that is obtained if one of the planar surfaces has been roughened. In comparison to the polished cylinder this reduces the mean fraction of trapped light to  $\tau \approx 48\%$  while the radial dependence reflected in the value of  $\sigma_\tau$  remains almost constant. Here, roughening is far less effective in removing trapped light in comparison to the simulations depicted in figure 5.1. This can be assigned to the smaller absorption length which leads to the fact that a lot of photons will be absorbed before they can get "untrapped" by the roughened surface. Especially photons emitted almost perpendicularly to the cylinder axis have a small probability of reaching the roughened surface. As the radial dependence of the fraction of trapped light arises from the photons escaping the curved surface,  $\sigma_\tau$  is hardly influenced by roughening the planar surface.

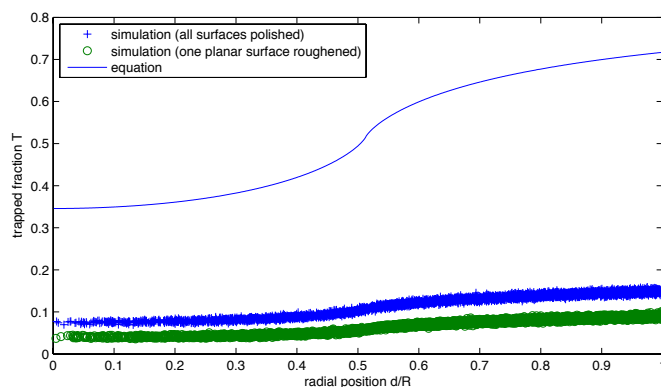
In this case it might be more efficient to roughen the curved surface of the cylinder. The results from such a simulation are also shown in figure 5.2 and table 5.3. As can be seen, the dependence of the trapped fraction on the radial position is almost eliminated which is also reflected in the low value of  $\sigma_\tau = 1.67\%$ . In addition, the

mean fraction of trapped light is decreased to  $\tau \approx 43\%$  (see table 5.3).

### Small scattering and large absorption lengths

<b>crystal shape</b>		
<b>crystal surfaces</b>	all surfaces polished	one planar surface roughened
$\tau$	12.30%	7.07%
$\sigma_\tau$	2.40%	1.65%

**Tab. 5.4:** Results of the light-output simulation for a cylindrical crystal with  $L_{abs} = 250cm$  and  $L_{scat} = 19.3cm$ . For further details see caption of table 5.2.



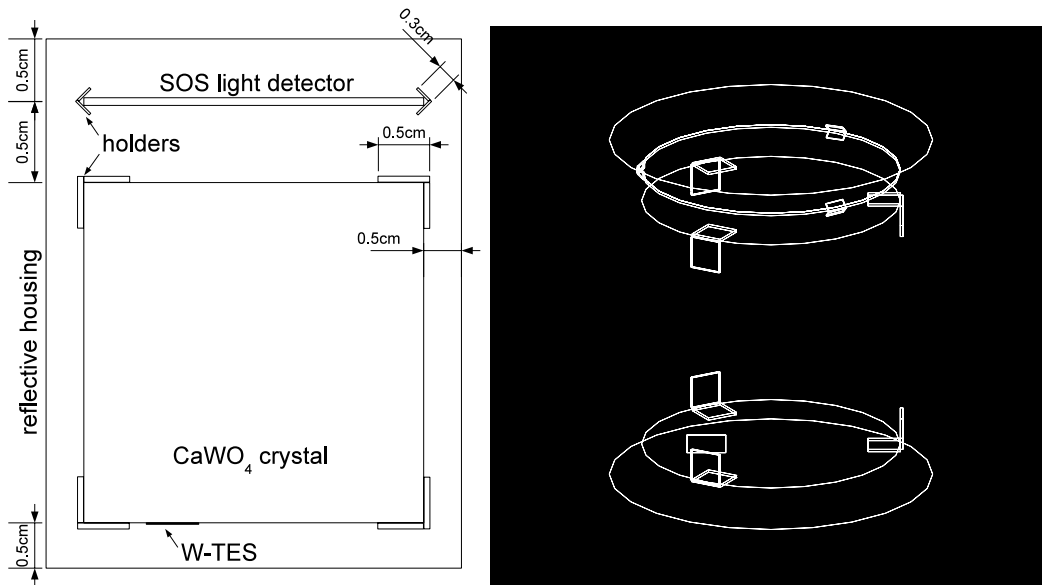
**Fig. 5.3:** Fraction of trapped light against the radial position in a cylindrical crystal with  $L_{abs} = 250cm$  and  $L_{scat} = 19.3cm$ . Due to the high ratio of scattering to absorption the graph is considerably lowered and flattened compared to the one calculated from equation 4.6. Roughening of one planar surface further reduces the fraction of trapped light and its radial dependence. See also table 5.4.

Figure 5.3 shows the graph obtained from a simulation which uses the values  $L_{abs} = 250cm$  and  $L_{scat} = 19.3cm$ . In this case only a mean fraction  $\tau \approx 12\%$  of the scintillation light remains trapped and the radial dependence of this fraction, i.e. the standard deviation  $\sigma_\tau = 2.40\%$  is relatively small (see table 5.4). This supports the fact that for such crystals the cylindrical shape is acceptable regarding the light output. In the case that one of the cylinder's planar surfaces is roughened

in the simulation the fraction of trapped light is reduced further to  $\tau \approx 7\%$  and the standard deviation to  $\sigma_\tau = 1.65\%$ .

## 5.2 Simulation of a CRESST-like Detector Module

The second simulation is a simplified model of a CRESST-II detector module. It includes a  $\text{CaWO}_4$  crystal equipped with a tungsten TES, a silicon-on-sapphire (SOS) light detector and detector holders enclosed together in a reflective housing. The geometry and dimensions of the setup are shown in figure 5.4. Running the simulation, the  $\text{CaWO}_4$  crystal is irradiated from the bottom side (opposite to the light detector) by  $122\text{keV}$  gammas with random directions. These interact via the Compton or photoelectric effect and produce scintillation events in the crystal. The scintillation photons that are absorbed by the SOS light detector are detected. The additional optical parameters that were used for this simulation are shown in table 5.5.



**Fig. 5.4:** Geometry and dimensions used in the simulation of a CRESST-like detector module. The simulation includes a  $\text{CaWO}_4$  crystal equipped with a tungsten TES, a silicon-on-sapphire (SOS) light detector and detector holders that are enclosed together in a reflective housing.

<b>CaWO<sub>4</sub> crystal</b>	
light yield	41300 $ph/MeV$ [35, 68]
<b>reflective housing</b>	
reflectivity <sup>1</sup>	98%@2.8 $eV$ [85]
<b>SOS light detector</b>	
absorption (silicon side) <sup>1</sup>	73%@2.8 $eV$ [29]
absorption (sapphire side) <sup>1</sup>	83%@2.8 $eV$ [29]
<b>holders</b>	
reflectivity <sup>1</sup>	91%@2.8 $eV$ [72]
<b>W-TES</b>	
reflectivity <sup>1</sup>	47%@2.8 $eV$ [72]

**Tab. 5.5:** Optical parameters used in the simulation of a CRESST-like detector module. The values of other parameters of the  $CaWO_4$  crystal are shown in table 5.1.

The light yield of the simulated crystal was  $22700ph/MeV$  at RT [68], which leads to a light yield of  $(22700 \cdot 1.82)ph/MeV \approx 41300ph/MeV$  at  $mK$  temperatures (see section 4.2).<sup>3</sup> The values of other parameters of the  $CaWO_4$  crystal are shown in table 5.1.

The values for the reflectivity of the housing were obtained from a measurement of the VM2002 foil at RT under an incident angle of  $10^\circ$ .<sup>4</sup> The absorption of the light detector (LD) was taken from measurements at RT from the silicon and from the sapphire side. The reflectivity of the holders and the TES are those of silver and tungsten for  $0^\circ$  incident angle, respectively. The spectra which were entered into the simulation and are shown in figure 5.5.

The disc-shaped light detector in the simulation has a radius of  $2cm$  and a thickness of  $460\mu m$ . The rectangular W-TES has a surface of  $6 \times 8mm^2$  and a thickness of  $200nm$ .

<sup>1</sup>Dependent on the photon energy (see figure 5.5).

<sup>3</sup>The non-proportionality of the light yield (see section 4.2) is not accounted for in the simulations.

<sup>4</sup>The wavelength shifting properties of the VM2002 foil were not implemented in the simulation.

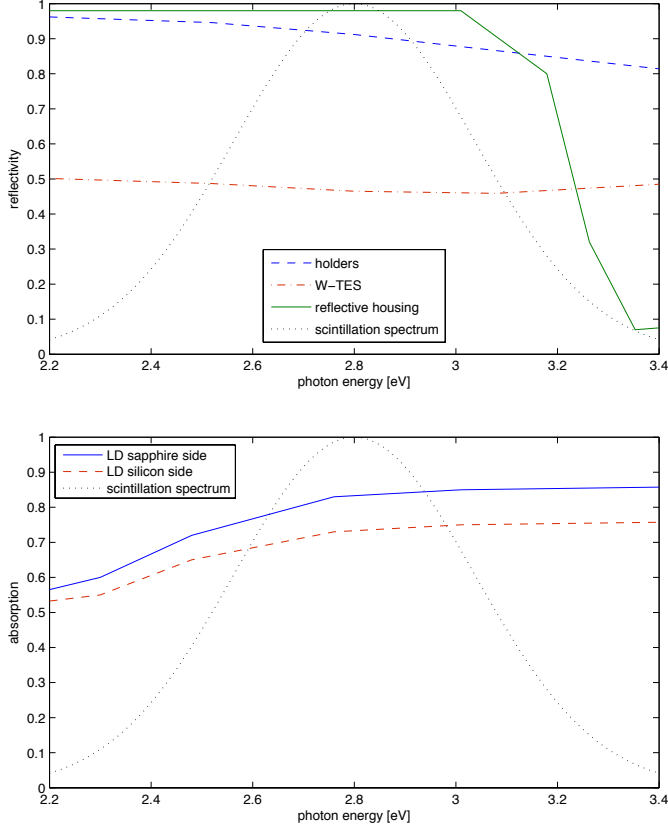


**Fig. 5.5:** Wavelength dependent reflection (top) and absorption spectra (bottom) of the objects implemented in the simulation of a CRESST-like detector module. For comparison the implemented scintillation spectrum of the  $CaWO_4$  crystal is also shown.

### 5.2.1 Results and Discussion

In the simulations, the fraction  $A$  of scintillation light (energy) that is absorbed by the light detector (LD) in each scintillation event is determined:

$$A = E_{LD}/E_{scint} \quad (5.5)$$

Here  $E_{scint}$  and  $E_{LD}$  are the total energies from photons that are produced in the  $CaWO_4$  crystal and absorbed by the light detector, respectively, in the scintillation event. The mean value of  $A$  is denoted by  $\eta$  which defines the collection efficiency of the setup while its standard deviation  $\sigma_\eta$  is a measure for the uniformity of the light collection with respect to the position of the scintillation event (analogous to

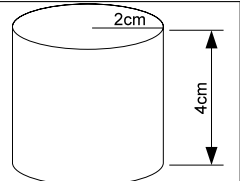
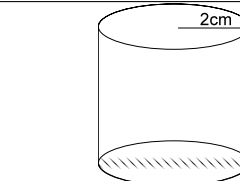
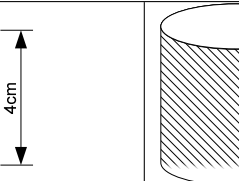
the values defined by equations (5.3) and (5.4):

$$\eta = \langle A \rangle \quad (5.6)$$

$$\sigma_\eta = \sigma(A) \quad (5.7)$$

In a detector module it is, of course, desirable to have a high and uniform light collection, i.e. a large value of  $\eta$  and a small value of  $\sigma_\eta$ .

The resolution of the  $122keV$  photopeak in the simulated energy spectrum<sup>5</sup> is defined as the ratio FWHM/Peak where Peak and FWHM are the peak position and full width at half maximum of a Gaussian fit.

			
<b>crystal shape</b>			
<b>crystal surfaces</b>	all surfaces polished	surface facing light detector roughened	curved surface roughened
$\eta$	13.19%	13.39%	18.51%
$\sigma_\eta$	1.33%	1.32%	0.96%
<b>FWHM/Peak</b>	13.05%	13.20%	11.02%

**Tab. 5.6:** Results of the simulation of a CRESST-like detector module. The light detector is facing the bottom surface of the crystal. Roughened surfaces are indicated by the shaded area. The value  $\eta$  is the collection efficiency of the setup defined by the mean fraction of light absorbed by the light detector. The standard deviation  $\sigma_\eta$  is a measure for the uniformity of the light collection. FWHM/Peak is the resolution obtained from the simulated spectrum.

<sup>5</sup>The simulated spectrum is only a histogram of the energy  $E_{LD}$  absorbed by the light detector and does not consider the intrinsic resolution of the light detector.

## 5. Monte Carlo (MC) Simulations

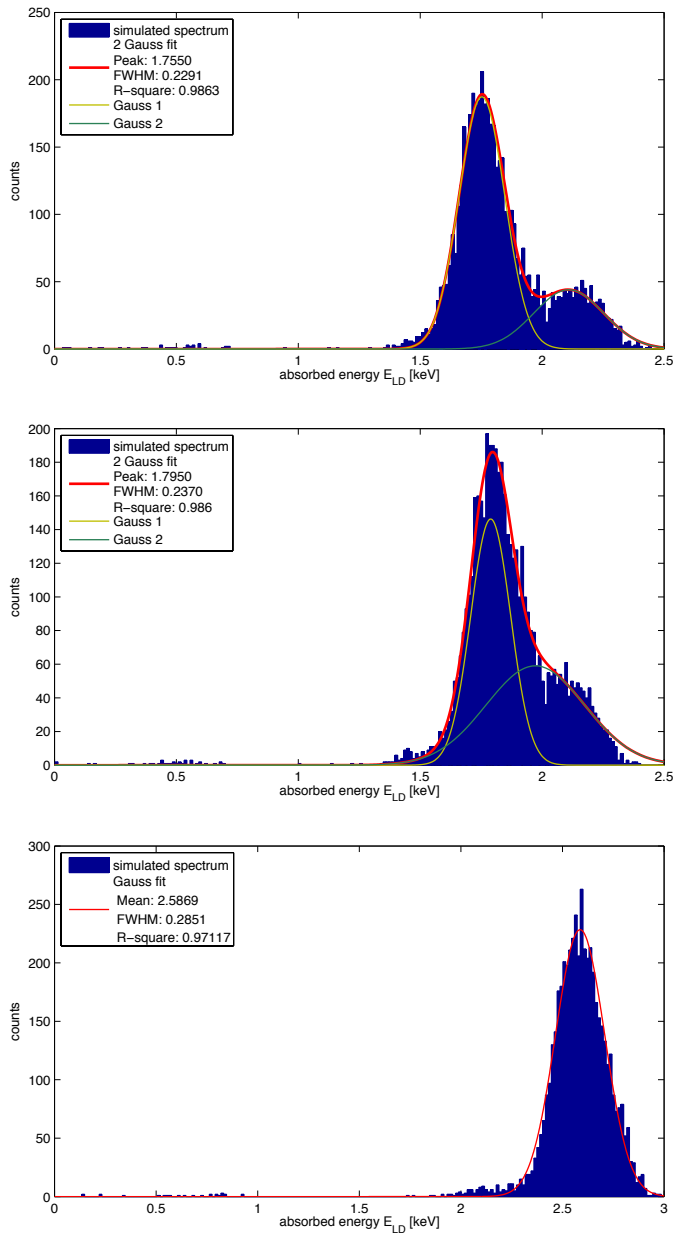


**Fig. 5.6:** Simulated spectrum of  $122\text{keV}$  gammas for the cylinder with all surfaces polished, the surface facing the light detector roughened and the curved surface roughened (from top to bottom). The doublet structure in the top figure arises from the radial dependence on the fraction of trapped light depicted in figure 5.2. Roughening of the planar surface facing the light detector reduces the doublet structure while roughening of the curved surface completely eliminates it.

### Cylinder with all surfaces polished

The second column in table 5.6 shows the results for the standard cylindrical crystal with all surfaces polished. The collection efficiency of this setup is  $\eta \approx 13\%$ . The mean fraction  $\langle A_{dep} \rangle$  of the total energy  $E_{dep}$  deposited by the gamma that is absorbed in the light detector in this setup is:

$$\langle A_{dep} \rangle = \left\langle \frac{E_{LD}}{E_{dep}} \right\rangle \approx 1.53\% \quad (5.8)$$

Experimentally this value is about 1% [28] which is in good agreement with equation (5.8). Additional losses can occur from gaps in the reflector for electrical connections which were not implemented in the simulation. Furthermore, the reflectivity of the foil has only been measured at RT and might decrease at  $mK$  temperatures.

The resolution of the  $122keV$  line in the simulated spectrum (see figure 5.6) has a value of  $FWHM/Peak \approx 13\%$ . The spectrum shows a doublet structure that can be fitted by two Gaussians. This structure arises from the spatial dependence of the fraction of trapped light depicted in figure 5.2 which has already been shown in previous simulations [86]. Due to the step-like shape of this curve the cylinder can roughly be divided into two regions at about half its radius. In the scintillation events originating from the region near the border of the cylinder a larger fraction of the photons remain trapped inside the crystal then for those occurring in the region near to the cylinder axis. Therefore scintillation events from the first region lead to the first Gaussian ("Gauss 1") in figure 5.6 while scintillation events from the region near the cylinder axis lead to the second Gaussian ("Gauss 2") in figure 5.6. This doublet structure has also been observed experimentally in some crystals in measurements in the CRESST setup (see figure 5.7) [21].

### Cylinder with the surface facing the LD roughened

The third column in table 5.6 shows the results of the simulation where the planar surface facing the light detector has been roughened. Experimentally this has been shown to improve the energy resolution because it eliminates the doublet structure and increases the light collection (see figure 5.7) [21]. The reduction of the doublet structure can also be observed in the simulated spectra (see figure 5.6) although the effect is not as pronounced as in figure 5.7. Furthermore, the simulation shows no significant increase of the light collection  $\eta$  or decrease of  $\sigma_\eta$  and hence also no improved resolution  $FWHM/Peak$ .

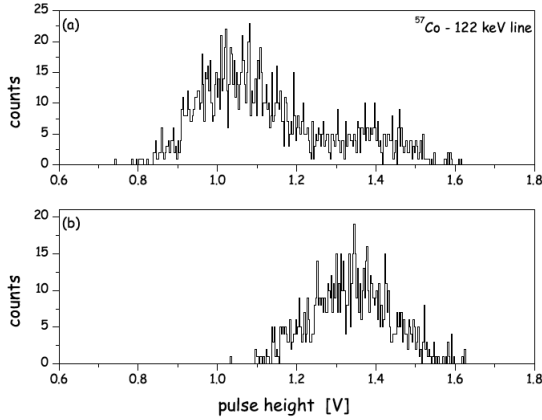


**Fig. 5.7:**  $^{57}\text{Co}$  122keV line measured in the Gran Sasso setup. a) all crystal surfaces polished, b) after roughening of the surface facing the light detector [21]. Roughening of the planar surface facing the light detector eliminates the doublet structure and increases the light collection.

### Cylinder with the curved surface roughened

As an alternative to one of the planar surfaces, it was shown in the section 5.1 that roughening of the curved surface is more effective in reducing trapped light and can in particular eliminate the spatial dependence of the trapped fraction. The results of a simulation of such a crystal are shown in the last column of table 5.6. In comparison to the polished cylinder the light collection  $\eta$  is increased by  $\sim 40\%$  and the simulated spectrum depicted in figure 5.6 shows no doublet structure. The resolution  $\text{FWHM/Peak}$  in this case is improved by  $\sim 16\%$ . It has to be stated that this result is in conflict with experimental results which showed that the best light collection is achieved with just the surface facing the light detector roughened [21]. This difference seems to originate from the fact that in contrast to the simulation, in the experiment roughening does mainly increase the transmission through the roughened surface itself. Generally this discrepancy can result from a difference in the angular distribution of the incident photons at the roughened surface or a difference in the angular distribution of the roughened surface between the simulation and experiment (see section 4.4). This in turn could be assigned to a different absorption and scattering length of the measured crystal, a difference in the geometry of the setup or a difference in the position and energy of the irradiating source<sup>6</sup> as well as a difference between the simulation model and a real roughened surface. The fact that roughening the curved surface is more effective in reducing the doublet structure though remains plausible because of the considerations described in the second paragraph of section 5.1.1.

<sup>6</sup>In the measurements the crystal was irradiated with a  $^{137}\text{Cs}$  source.

### Crystal with a smaller attenuation coefficient

In the previous section it was shown that the effects of a roughened surface do depend on the scattering and absorption coefficients of the crystal. Without scattering and absorption the roughened surface leads to maximal "untrapping". Therefore, the effects of roughening will become more prominent if the simulations are carried out with a smaller attenuation coefficient. Such a smaller value  $\alpha_{att} = 0.069\text{cm}^{-1}$  was found with another measurement [86] by comparing the transmission of two  $\text{CaWO}_4$  crystals from SRC "Carat". Under the assumption that the ratio  $B = \alpha_{scat}/\alpha_{abs}$  is the same as for the crystal used for the previous simulations, the corresponding values for the scattering and absorption lengths are  $L_{scat} = 30.1\text{cm}$  and  $L_{abs} = 27.9\text{cm}$ . Figure 5.8 shows the results of simulations where the parameters  $L_{abs}$  and  $L_{scat}$  have been replaced by these values. For the polished crystal the obtained results were  $\eta = 18.43\%$ ,  $\sigma_\eta = 2.10\%$  and  $FWHM/Peak = 13.69\%$ , for the roughened crystal  $\eta = 20.07\%$ ,  $\sigma_\eta = 1.70\%$  and  $FWHM/Peak = 11.96\%$ . It can be seen though that the double Gaussian fit is less accurate than in figure 5.6. Besides the reduction of the doublet structure here roughening leads to an increase of the light collection  $\eta$  by  $\sim 9\%$  and to an improvement of the resolution  $FWHM/Peak$  by  $\sim 13\%$ . However, experimentally an increase of the light collection of  $\sim 50\%$  was measured. Furthermore, in the simulation the doublet structure does not completely disappear after roughening as it did experimentally. These remaining differences can result from a still lower value of  $\alpha_{att}$  for the crystal used in the measurement and/or the simulation model might be insufficient for the description of the real roughened surface.

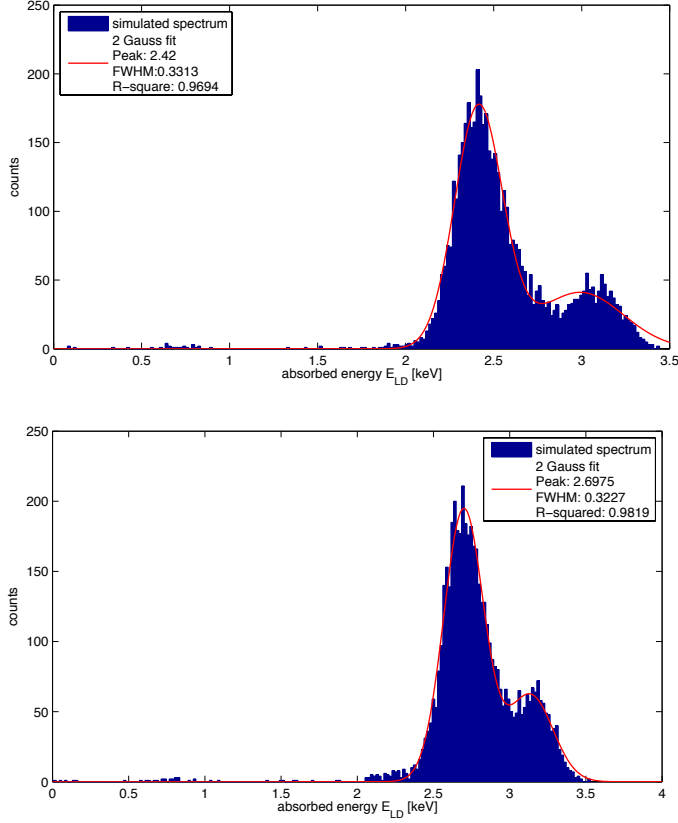


**Fig. 5.8:** Simulated spectrum of  $122\text{keV}$  gammas for a cylindrical crystal with lower attenuation coefficient  $\alpha_{att} = 0.069\text{cm}^{-1}$  with all surfaces polished (top) and the surface facing the light detector roughened (bottom). Here roughening of the surface facing the light detector reduces the doublet structure and increases the light collection.

### 5.3 Simulation of Differently Shaped Crystals and Housings

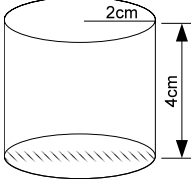
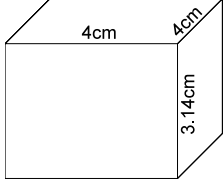
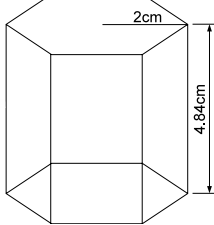
If the shape of the  $\text{CaWO}_4$  crystals is modified for better light collection, a number of aspects have to be taken into account. At first, it would be desirable to lose only as little material as possible when cutting the crystals from the ingot. Secondly, the crystals should have a large mass (volume) and a shape suited for close packing. If the detector modules are densely packed the chance to identify neutrons by multiple scattering is increased. In addition, it allows the installation of a large detector mass in the volume that is limited by the size of cryostat. Such

considerations will become more important in the future large-scale EURECA experiment. Additionally, the crystal must also be suited as a phonon detector, i.e. one must be able to deposit a TES on it. To reach the same collection properties for *phonons* as in the current cylindrical crystals, the fraction of the surface area covered by the TES should not decrease. Finally to reach a good reproducibility the manufacturing process should not be too complex.

For the simulation of differently shaped crystals and housings the MC simulation of the CRESST-like detector module (see section 5.2) was modified. The detector holders and the W-TES were not implemented because their shape and size would individually depend on the crystal. The crystal surface facing the light detector was either roughened (*r*) or all surfaces were polished (*p*). The dimensions of the light detector were kept unchanged. The reflective housing was always changed so that all distances depicted in figure 5.4 stayed constant. In addition, because  $122keV$  gammas have only a range of a few *mm* inside the crystal all events would occur near the surface. To reach a uniform irradiation of the whole crystal, scintillation events were generated similarly as in the light-output simulation (see section 5.1). The photons were again detected by the SOS light detector.

### 5.3.1 Results and Discussion

The different simulated geometries were again evaluated in terms of their efficiency  $\eta$  and uniformity  $\sigma_\eta$  of the light collection (see equations (5.6) and (5.7)). A good detector module should exhibit a high and uniform light collection, i.e. a large value of the ratio  $\eta/\sigma_\eta$ .

module	a)	b)	c)
crystal shape			
reflective housing shape	cylinder	box	hexagonal prism
crystal surfaces	$r$	$p$	$p$
crystal volume	$50.27\text{cm}^3$	$50.27\text{cm}^3$	$50.27\text{cm}^3$
$\eta$	15.84%	16.41%	16.46%
$\sigma_\eta$	1.65%	0.68%	1.04%
$\eta/\sigma_\eta^7$	1	2.51	1.65

**Tab. 5.7:** Results of the CRESST-like detector-module simulation with differently shaped crystals and housings. The light detector is facing the bottom surface of the crystals. This surface was either roughened ( $r$ ), indicated by the shaded area, or all surfaces of the crystal remained polished ( $p$ ). The value  $\eta$  is the light collection efficiency of the setup. The standard deviation  $\sigma_\eta$  is a measure for the uniformity of the light collection. A good detector module should exhibit a high and uniform light collection, i.e. a large value of the ratio  $\eta/\sigma_\eta$ .

<sup>7</sup>normalized to module a)

### 5.3. Simulation of Differently Shaped Crystals and Housings

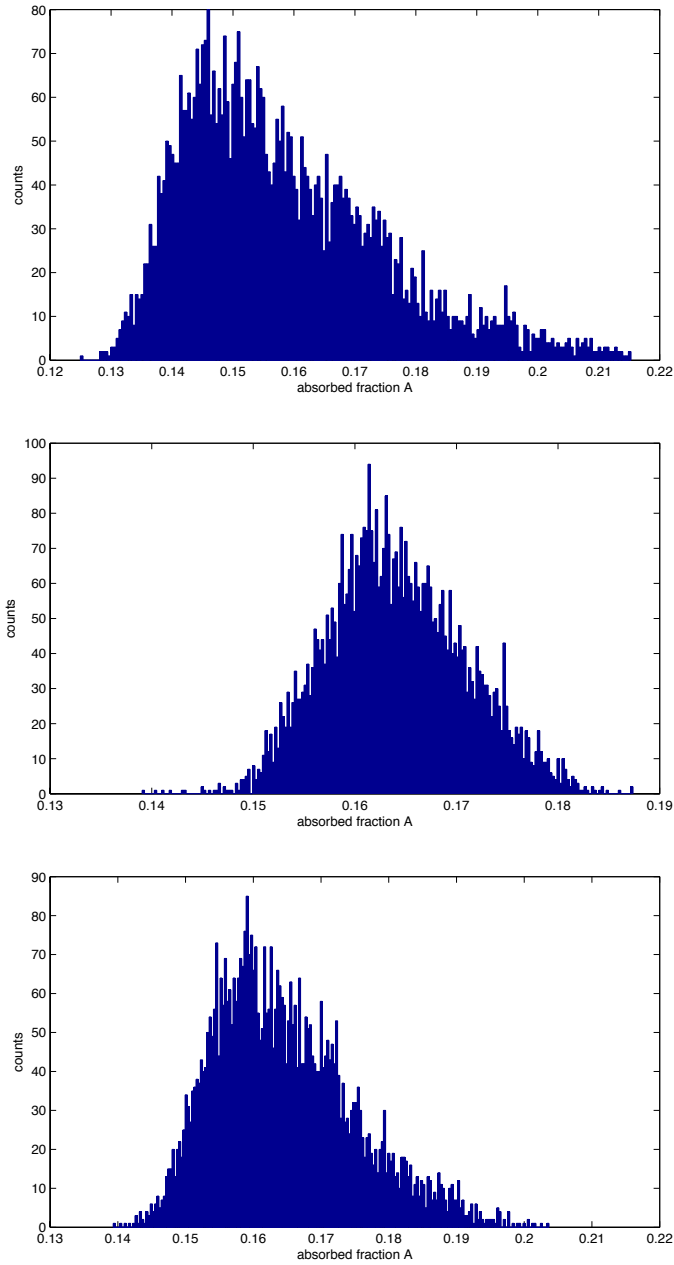


**Fig. 5.9:** Histogram of the fraction  $A$  of light absorbed by the light detector for modules a), b), c) (from top to bottom) (see also table 5.7). The most uniform light collection is achieved with module b) while the histograms of modules a) and c) exhibit non-Gaussian shapes.

## 5. Monte Carlo (MC) Simulations

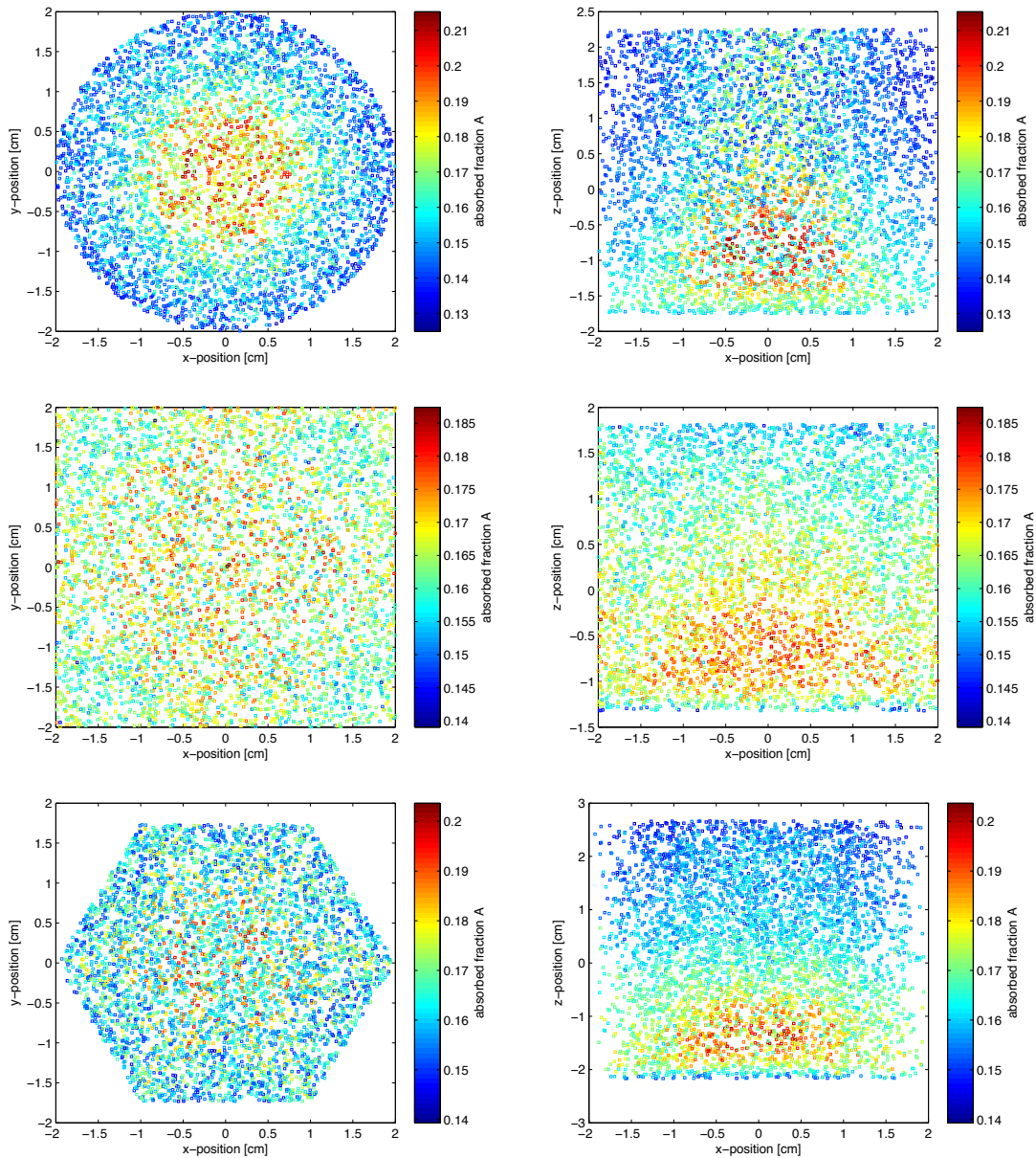


**Fig. 5.10:** Dependence of the absorbed fraction  $A$  on the position of the scintillation event in the x-y (left) and the x-z planes (right) in module a), b), c) (from top to bottom) (see also table 5.7). The z-axis is the crystal axis. The light detector is facing the x-y plane at negative z.

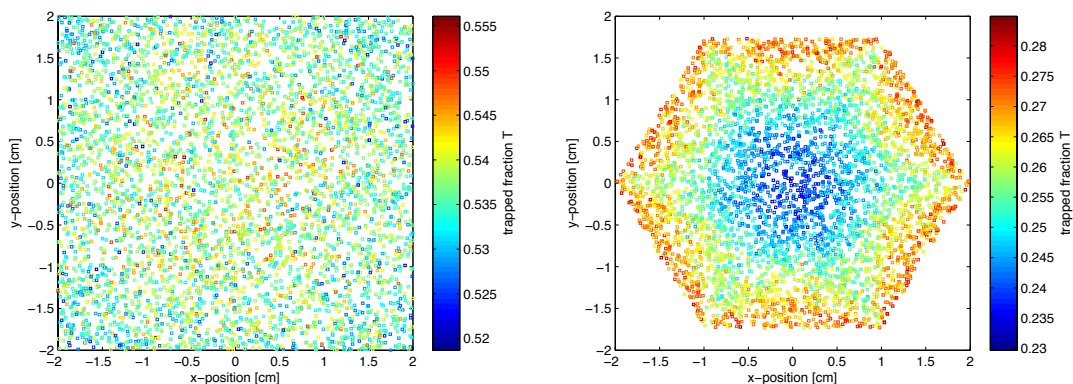


**Fig. 5.11:** Dependence of the fraction  $T$  of trapped light (see equation 5.2) on the position of the scintillation event in the x-y plane in the crystal from module b) (left) and module c) (right). The crystal from module b) shows no large radial dependence of the trapped fraction while in module c) the trapped fraction increases with distance from the crystal axis, similarly to the cylinder.

### Cylindrical crystal and housing

To obtain a reference the simulation was first carried out with the standard cylinder ( $d = 40\text{mm}$ ,  $h = 40\text{mm}$ ) where the planar surface facing the light detector is roughened. The results are summarized in table 5.7. Figure 5.9 displays a histogram of the fraction  $A$  of the energy from scintillation photons that are absorbed by the light detector (see equation (5.5)). Figure 5.10 shows the absorbed fraction  $A$  in dependence of the position of the scintillation event in the x-y and x-z planes of the crystal. In both planes an increased light collection for events originating from positions nearer to the center of the cylinder is visible. This results from the already mentioned radial dependence of the fraction of (quasi) trapped light which also leads to the doublet structure depicted in figure 5.6. In addition, the plot of the x-z plane shows an increased light collection for events with less distance to the light detector (smaller z-position) since such photons have to travel shorter path lengths and therefore a smaller probability of getting absorbed inside the crystal. However, for very small distances from the light detector the light collection decreases again. This results from a reduced number of photons that can reach the light detector by exiting the curved surface of the cylinder (for a more detailed discussion see [86]).

### Block-shaped crystal and housing

Table 5.7 also shows the results of a simulation with a block-shaped crystal of the same volume as the currently used cylinder and a box-shaped housing. Since the

ingots produced with the Czochralski method already have a block-like shape (see section 4.1) this would have the advantage of losing only little material when the crystals are cut. A box-shaped crystal and housing will also be more useful for close packing of the detector modules.

The collection efficiency  $\eta$  of this module shows only a small increase by  $\sim 3.6\%$  compared to the currently used module a). This is in agreement with the fact that the fraction of trapped light in an ideal, block-shaped scintillator with the refractive index of  $CaWO_4$  is  $\sim 56\%$  [87, 88] which is only slightly lower than the mean value  $\tau \approx 60\%$  obtained for the cylinder (see section 5.1). However, the considerably decreased value of  $\sigma_\eta = 0.68\%$  compared to  $\sigma_\eta = 1.65\%$  indicates that the light collection is much more uniform which can also be seen in figure 5.10. This can be assigned to the fact that, in contrast to the cylinder, the fraction  $T$  of (quasi) trapped light (see equation 5.2) in the block-shaped crystal shows no large radial dependence (see figure 5.11) since it has a rectangular instead of a circular cross section. Due to the more uniform light collection the histogram of the fraction  $A$  of absorbed light for this module shows a more Gaussian distribution (see figure 5.9). The ratio  $\eta/\sigma_\eta$ , which is an indication for the efficiency and uniformity of the light collection of this module shows an increase by a factor of 2.51 compared to module a).

### Hexagonal crystal and housing

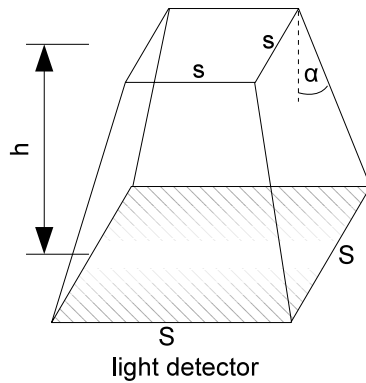
Another interesting shape for close packing would be a hexagonal module. The result of the simulation with a crystal (of the same volume as the currently used cylinder) and housing both shaped like a hexagonal prism is also shown in table 5.7. Here, the ratio  $\eta/\sigma_\eta$  shows an increase by a factor of 1.65 compared to module a). As for the block-shaped crystal, this increase is mainly due to a more uniform light collection because of the non-circular cross section. However, in comparison to module b) it shows a less uniform light collection reflected in a higher value of  $\sigma_\eta$ , and the histogram of the fraction of absorbed light has a less Gaussian distribution. This can be assigned to the higher symmetry of the hexagonal shape for which the fraction  $T$  of (quasi) trapped light does show some radial dependence. In figure 5.11 it can be seen that the trapped fraction  $T$  increases with distance from the crystal axis similarly to the cylinder. This leads to a slight position dependence of the light collection in the x-y plane (see figure 5.10).

### Taper-shaped crystal and box-shaped housing

As explained in section 4.4 scintillators in high energy physics (HEP) and nuclear medicine often have a taper-shaped axial cross section with the large end face facing the light detector since this leads to a better light collection due to the

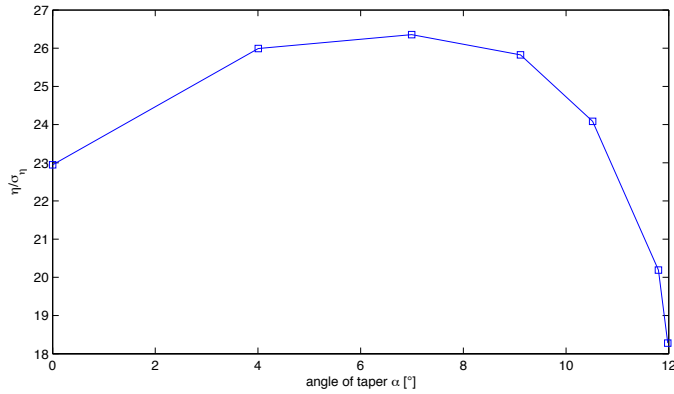
"focussing effect". For such a trapezoidal crystal it would be unfortunate to lose a lot of material when cutting the crystal from the ingot. However, it is possible to grow crystals with an increasing or decreasing diameter so that the ingot already has a trapezoidal shape.

Various simulations were carried out with the crystal shaped as a truncated square pyramid in a box-shaped housing. In all simulations the large end face was facing the light detector and had been roughened (see figure 5.12). To determine the best angle of taper  $\alpha$  two of the three parameters that define the shape of the truncated square pyramid were fixed and the third was iterated in the simulations. In the Czochralski process it can be challenging to grow crystals with a large diameter with respect to the crucible. To increase the height, on the other hand, is simpler. Therefore the parameter  $S = 4cm$  was fixed in all simulations.

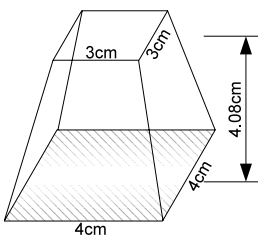


**Fig. 5.12:** Crystal shaped like a truncated square pyramid with the surface facing the light detector roughened.

Truncated square pyramids with constant volume but varying height



**Fig. 5.13:** Ratio  $\eta/\sigma_\eta$  for modules with crystals shaped like truncated square pyramids with varying angles of taper and constant volume but varying height.

module	d)
crystal shape	
reflective housing shape	box
crystal surfaces	$r$
crystal volume	$50.27\text{cm}^3$
$\eta$	18.36%
$\sigma_\eta$	0.70%
$\eta/\sigma_\eta$ <sup>8</sup>	2.73

**Tab. 5.8:** Results of the CRESST-like detector-module simulation for a crystal shaped like a truncated square pyramid in a box-shaped housing and with the surface facing the light detector roughened. Other details as in table 5.7.

<sup>8</sup>Normalized to module a)

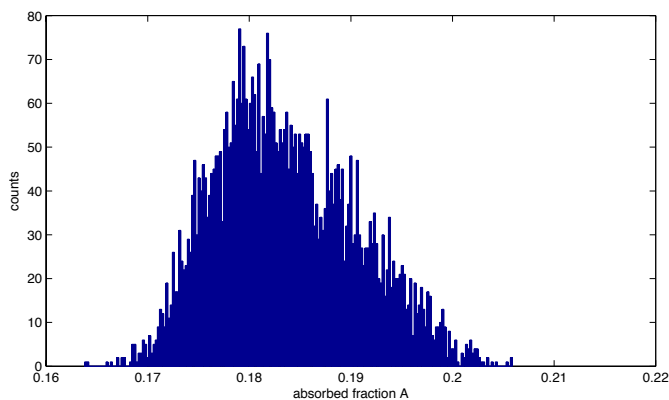


**Fig. 5.14:** Histogram of the fraction  $A$  of absorbed light for module d).

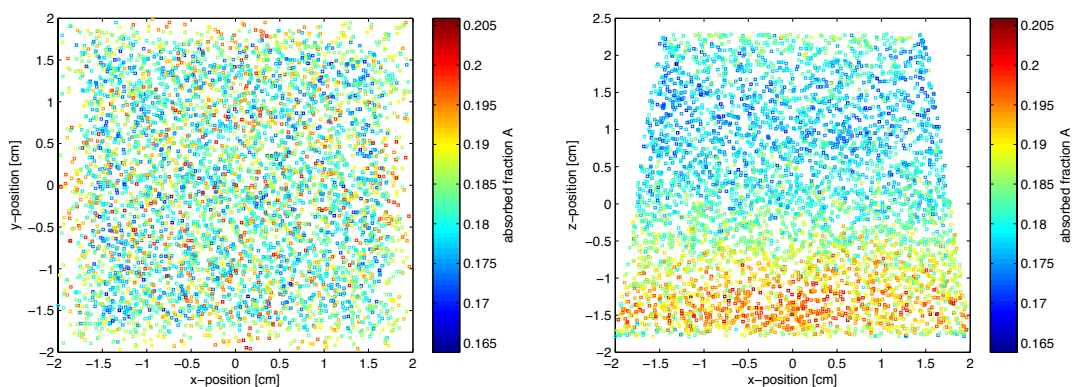


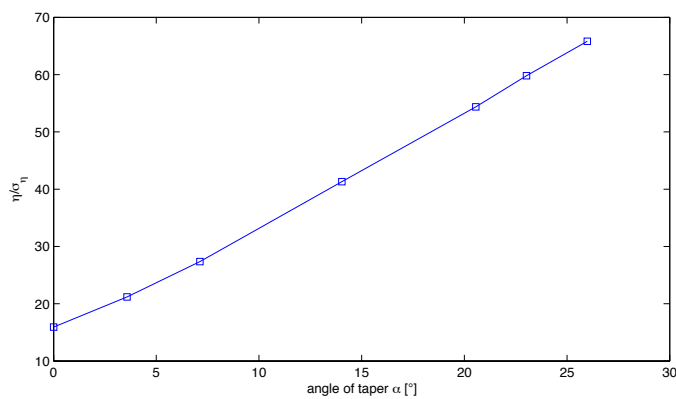
**Fig. 5.15:** Dependence of the fraction  $A$  of absorbed light on the position of the scintillation event in the x-y (left) and x-z plane (right) in module d).

In addition to  $S = 4\text{cm}$ , as a second parameter, at first the volume of the crystals was kept constant in the simulations. Figure 5.13 shows the ratio  $\eta/\sigma_\eta$  of modules that employ crystals with the fixed dimensions  $S = 4\text{cm}, V = 50.27\text{cm}^3$  and varying angles of taper  $\alpha$ .<sup>9</sup> It was observed that the light collection  $\eta$  and the non-uniformity  $\sigma_\eta$  increases with a larger angle of taper  $\alpha$ . At larger angles though the increase of the non-uniformity  $\sigma_\eta$  becomes dominant and the ratio  $\eta/\sigma_\eta$  decreases. The results of the module with the best ratio  $\eta/\sigma_\eta$  are summarized in table 5.8. Compared to the currently used module a) it shows an increase of the ratio  $\eta/\sigma_\eta$  by a factor of 2.73. The non-uniformity  $\sigma_\eta = 0.70\%$  in this case remains small and

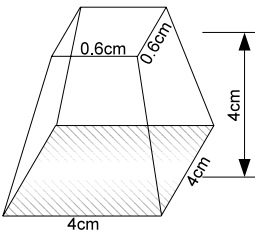
<sup>9</sup>Since the volume of the crystal is kept constant a larger angle of taper also means a larger height of the crystal (see figure 5.12).

the histogram of the fraction of absorbed light shows almost a Gaussian distribution (see figure 5.14). Figure 5.15 shows that the light collection in the x-y plane is rather uniform. The light collection in the x-z plane shows a similar behavior as in the other crystals with a rectangular axial cross section. Here however, the light collection is increasing again near the end of the crystal at large  $z$  values.

### Truncated square pyramids with varying volume but constant height



**Fig. 5.16:** Ratio  $\eta/\sigma_\eta$  for modules with crystals shaped like truncated square pyramids with varying angles of taper and varying volume but constant height.

module	e)
crystal shape	
reflective housing shape	box
crystal surfaces	$r$
crystal volume	$25.01\text{cm}^3$
$\eta$	31.18%
$\sigma_\eta$	0.52%
$\eta/\sigma_\eta^{10}$	4.77

**Tab. 5.9:** Results of the CRESST-like detector-module simulation for a crystal shaped like a truncated square pyramid in a box-shaped housing and with the surface facing the light detector roughened. Other details as in table 5.7.

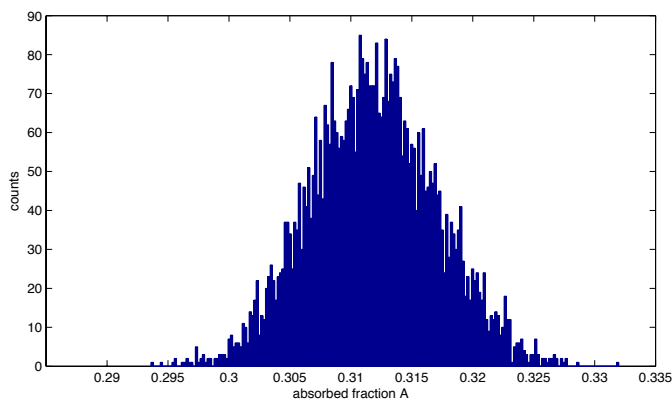


**Fig. 5.17:** Histogram of the fraction  $A$  of absorbed light for module e).

<sup>10</sup>Normalized to module with roughened cylinder of the same volume.

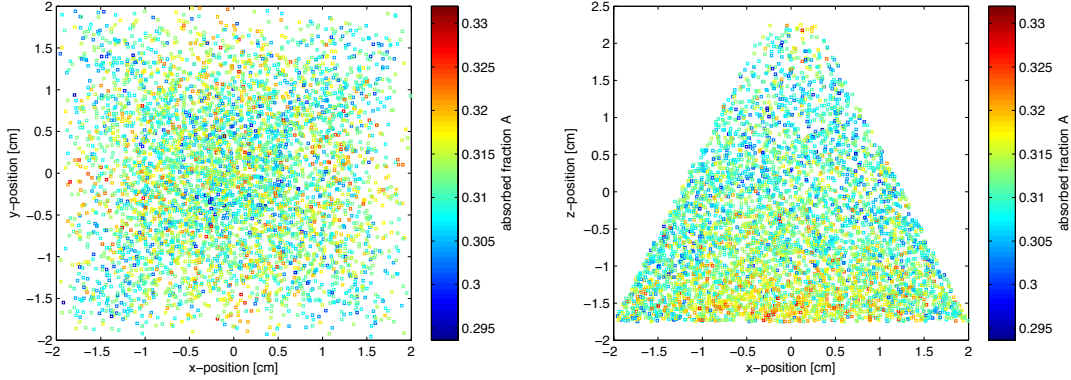


**Fig. 5.18:** Dependence of the fraction  $A$  of absorbed light on the position of the scintillation event in the x-y (left) and x-z plane (right) in module e).

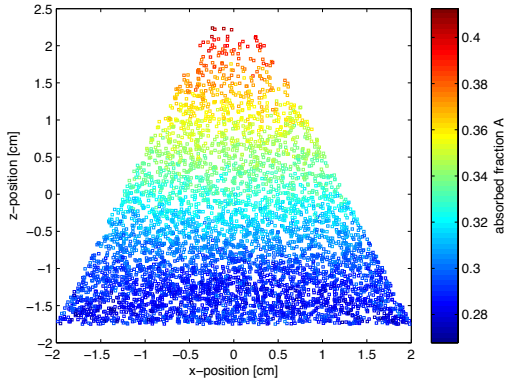


**Fig. 5.19:** Dependence of the fraction  $A$  of absorbed light on the position of the scintillation event in the x-z plane for module e) when all surfaces of the crystal remain polished. The light collection increases along the z-axis which can be assigned to the "focussing effect" (see section 4.4).

In another approach, simulations were carried out where instead of the volume the height of the crystals was kept constant. Figure 5.16 shows the ratio  $\eta/\sigma_\eta$  of modules that employ crystals with fixed dimensions  $S = 4\text{cm}, h = 4\text{cm}$  and varying angles of taper  $\alpha$ .<sup>11</sup> Here the ratio  $\eta/\sigma_\eta$  is increasing with increasing angle of taper. The reason for this is that again the light collection  $\eta$  increases with a larger angle of taper while an increasing non-uniformity  $\sigma_\eta$  is avoided due to the roughened surface. The best result is therefore obtained with a roughened (untruncated) pyramid. However, it may be more useful to produce a truncated

<sup>11</sup>This means that the volume is decreasing with increasing angle of taper (see figure 5.12).

pyramid because it leaves a small surface  $SA_{TES}$  for the deposition of a TES. Under the condition that the fraction of  $SA_{TES}$  to the total surface area  $SA$  should not be smaller than the value  $SA_{TES}/SA = 6.37 \cdot 10^{-3}$  of the current cylindrical *phonon* detectors, this surface then has to be at least  $0.6 \times 0.6 \text{cm}^2$ . Table 5.9 displays the results of a module with a crystal shaped in this way. The ratio  $\eta/\sigma_\eta$  shows an increase by a factor of 6.25 compared to the currently used module a). However, the volume of this crystal is decreased by  $\sim 50\%$ . In comparison to a module using a cylinder of the same volume ( $R = 2\text{cm}, h = 1.99\text{cm}$ ) the ratio  $\eta/\sigma_\eta$  still shows an increase by a factor of 4.77. Due to the very uniform light collection the histogram of the fraction of absorbed light for this module exhibits a nice Gaussian distribution (see figure 5.17). In figure 5.18 no large position dependencies of the light collection are visible. If however all surfaces of the crystal remain polished the light collection shows an increase along the z-axis (see figure 5.19). This is due to the "focussing effect" which leads to smaller incident angles on the surface facing the light detector for photons that undergo more reflections on the side walls (see section 4.4). In the simulation, roughening of the surface facing the light detector restores the uniformity of the light collection while the increased collection efficiency is retained because the photons are still mainly reflected towards the light detector and less light can escape through the small surface on the opposite side.

## 5.4 Summary and Consequences for New Detectors

### Cylindrical Module

The simulations of a cylindrical crystal with dimensions as those used in CRESST-II showed that depending on the scattering and absorption lengths on average  $\sim 12\% - 60\%$  of the scintillation light remains (quasi) trapped inside the crystal. This fraction  $T$  depends on the radial position of the emission point and increases with the distance from the cylinder axis. Roughening of one planar surface reduces the mean fraction of (quasi) trapped light to  $\sim 7 - 48\%$  depending on the absorption and scattering lengths.

In the simulations of a CRESST-like detector module the radial dependence of  $T$  leads to a doublet structure in the spectrum of  $122\text{keV}$  gammas which has also been observed experimentally. The obtained energy resolution of the simulated  $122\text{keV}$  gamma line was  $\sim 13\%$ .<sup>12</sup> As observed experimentally and confirmed by the sim-

---

<sup>12</sup>This value does take into account only the variations of the deposited energy, the number of generated photons and the efficiency of the light collection but not the intrinsic resolution of the light detector.

ulation, roughening of the surface facing the light detector reduces the doublet structure and increases the light collection. This increase, however, was not significant for an attenuation coefficient of  $0.126\text{cm}^{-1}$ .<sup>13</sup> As an alternative, roughening of the curved surface showed an increase of the light collection and improvement of the resolution by  $\sim 40\%$  and  $\sim 16\%$ , respectively, and completely eliminated the doublet structure. For a crystal with a smaller value of  $\alpha_{att} = 0.069\text{cm}^{-1}$  roughening of the planar surface increased the light collection and improved the resolution by  $\sim 9\%$  and  $\sim 13\%$ , respectively. Experimentally though the effects of roughening seem more pronounced than in the simulation which might be assigned to a difference of the optical properties of the crystal or a difference between the simulation model and a real roughened surface.

The simulation showed that on average  $\sim 13\%$  of the scintillation light is absorbed by the light detector. The fraction of deposited energy that is detected as scintillation light in the simulation is  $\sim 1.5\%$ , in good agreement with experimental results that showed values of  $\sim 1\%$  [28].

## Block-shaped and Hexagonal Module

In the simulations of differently shaped modules a block-shaped crystal together with a box-shaped housing exhibits a more uniform light collection, with respect to the position of the scintillation event, compared to the currently used cylindrical module. The ratio  $\eta/\sigma_\eta$ , where  $\eta$  is the efficiency and  $\sigma_\eta$  is a measure for the uniformity (spatial dependence) of the light collection, shows an increase by a factor of  $\sim 2.5$  for this block-shaped module.

A crystal and housing both shaped like a hexagonal prism also shows a more uniform light collection compared to the cylindrical module. The increase of the ratio  $\eta/\sigma_\eta$  amounts to a factor of  $\sim 1.7$ . Both modules would also be more suited for close packing compared to the cylindrical module.

## Module with a Taper-shaped Crystal

The collection efficiency in a box-shaped housing and a crystal shaped as a truncated square pyramid is considerably improved and, in particular, it increases with increasing angle of taper. However, for a crystal of the same volume as the cylinder and varying height also the non-uniformity increases with the angle of taper so that the ratio  $\eta/\sigma_\eta$  can only be improved by a factor of  $\sim 2.7$  compared to the cylindrical module. As this value is not significantly larger than the increase by a factor of  $\sim 2.5$  achieved with the block-shaped crystal, the latter seems more feasible especially for large-scale production since it is easier to manufacture from

---

<sup>13</sup>This value results from the values  $L_{abs} = 15.4\text{cm}$  and  $L_{scat} = 16.4\text{cm}$  (see table 5.1).

the original ingot.

For crystals shaped like a truncated square pyramid with constant height (varying volume) the light collection also increases with the angle of taper while it remains uniform if the surface facing the light detector is roughened in the simulations. Such a crystal with a large enough end face for the deposition of a TES shows an increase of the ratio  $\eta/\sigma_\eta$  by a factor of  $\sim 6.3$  compared to the currently used cylindrical module. The volume of this crystal though is reduced by  $\sim 50\%$  which makes it less suited for close packing. Compared to a cylindrical module with a crystal of the same volume the ratio  $\eta/\sigma_\eta$  still shows an increase by a factor of  $\sim 4.8$ .

## Consequences for New Detectors

Ultimately, the amount of trapped light in a cylinder and therefore also the profit of a modified shape will depend on the crystal's scattering and absorption coefficient. For a very high ratio of scattering to absorption as observed in [66] a cylindrical crystal can be sufficient regarding the light collection. If the values for the absorption and scattering length, however, are comparable as the values in [68] a modified shape seems promising. In this case, the simulations favor a crystal shaped like a truncated square pyramid with the large end face (facing the light detector) roughened in a box-shaped housing as it showed the highest and most uniform light collection. However, it has to be tested experimentally if the roughened surface can retain a uniform light collection as it was observed in the simulations. In every case this crystal has some disadvantage concerning the close packing of the detector modules since it has similar dimensions but only  $\sim 50\%$  of the volume compared to the currently used cylinder. As an alternative a block-shaped crystal (with the same volume as the cylinder) in a box-shaped housing offers close packing and also shows a very uniform light collection. A block-shaped crystal has the additional advantage of losing less material from the originally grown ingot than the other shapes considered. Furthermore, in comparison to a truncated pyramid a block-shaped crystal will be easier to manufacture. Thus this configuration appears to be the most favored one (see section 7).



# Chapter 6

## Characterization of the Self-Grown $CaWO_4$ Crystals

The  $CaWO_4$  crystals grown at the crystal laboratory of the TUM are to be used in CRESST-II or the future EURECA experiment. For this reason it is important to thoroughly investigate the properties of the  $CaWO_4$  crystals. In particular, the absorption and scattering lengths of the crystals have to be determined to see if a modified shape will be profitable for the light collection. In addition, a large light yield, high radiopurity and good phonon propagation properties are desired.

### 6.1 Transmission Measurement

To determine the attenuation coefficient  $\alpha_{att}$  a transmission measurement was performed with the self-grown crystal "Sheldon II" (see table 4.2). In a transmission measurement a sample is placed into a collimated beam of light and the losses in intensity for certain wavelengths are determined. The transmissivity  $T$  is defined as

$$T = I_1/I_0 \quad (6.1)$$

where  $I_1$  and  $I_0$  are the measured intensities with and without the sample in the beam, respectively. For this measurement a Perkin Elmer LAMBDA 850 UV/Vis spectrophotometer [89] was used. The transmissivity was measured for wavelengths from 250 – 800nm in steps of 1nm.

#### 6.1.1 Results and Discussion

Figure 6.1 shows the measured transmissivity  $T$  in dependence of the wavelength. The mean value (solid line) and error at 95% CL (dashed lines) were calculated from the data of four independent measurements.

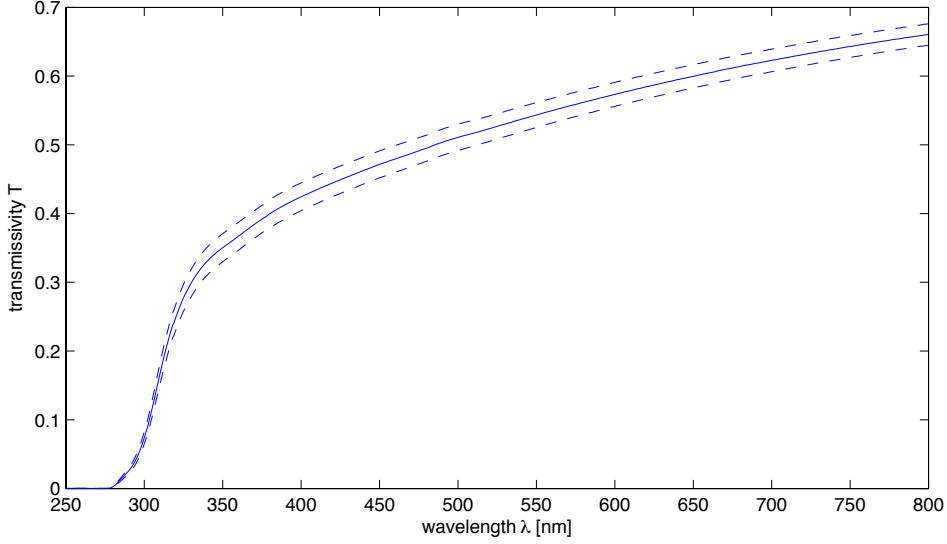


**Fig. 6.1:** Wavelength dependent transmissivity  $T$  of the crystal "Sheldon II" grown at the crystal laboratory of the TUM. The solid line shows the mean value and the dashed lines the errors derived from the data of four independent measurements. The vanishing transmissivity at  $\sim 300\text{nm}$  is due to intrinsic absorption.

The measured transmissivity  $T$  is due to the attenuation of the light inside the crystal and reflection on the surfaces.<sup>1</sup>

$$T = \frac{(1 - R)^2 \cdot \exp(-\alpha_{att}d)}{1 - R^2 \cdot \exp(-2\alpha_{att}d)} \quad (6.2)$$

Here  $d$  is the crystal's thickness,  $\alpha_{att}$  its attenuation coefficient, and  $R$  its reflectivity. The denominator of this equation accounts for multiple reflections.

In the measurement, the crystal was aligned with the beam of light perpendicular to the surface and parallel to the optical axis (c-axis, see figure 4.6) of the crystal so that no birefringence occurs. Therefore, the reflectivity can be calculated as

$$R = \frac{(n_o - 1)^2}{(n_o + 1)^2} \quad (6.3)$$

with  $n_o$  being the ordinary refractive index. Using the dispersion formula (5.1) for  $n_o$ , the measured transmissivity  $T$ , and  $d = 1.78\text{cm}$  (see table 4.2), the attenuation coefficient  $\alpha_{att}$  was calculated via equation (6.2). The result is shown in figure 6.2.

---

<sup>1</sup>The vanishing transmissivity at  $\sim 300\text{nm}$  is due to intrinsic absorption corresponding to the excitation of electrons from the valence band to the exciton levels.

For a wavelength of  $430\text{nm}$  (peak position of the  $\text{CaWO}_4$  scintillation spectrum at RT) the attenuation coefficient was determined as  $\alpha_{att} = 0.3348 \pm 0.0255\text{cm}^{-1}$ . This is about a factor of 3 higher than the value of  $0.126\text{cm}^{-1}$  that was measured for a crystal from SRC "Carat" [86]. However, the ingot from which the crystal was obtained was not annealed under oxygen atmosphere before the measurement. Since annealing can reduce scattering centers in the crystal the attenuation coefficient is expected to decrease after the process. The given error was calculated from the statistical errors of the measured transmissivity and the measured thickness ( $\Delta d = 0.05\text{mm}$ ). However, it has to be pointed out that there are some additional uncertainties in the value  $\alpha_{att}$  because the refractive index of the crystal was not directly measured and surface irregularities can cause errors in the measured transmissivity in the order of  $\sim 20\%$  [86].

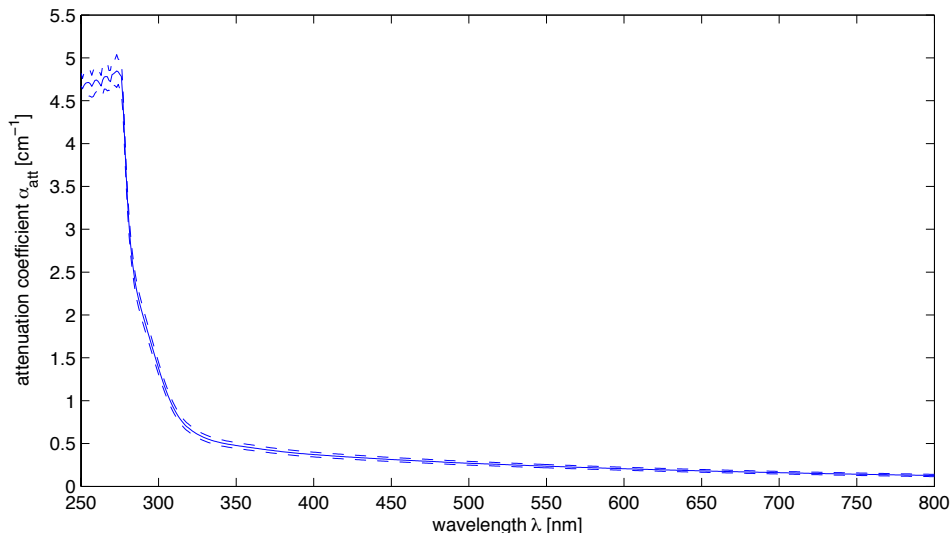


**Fig. 6.2:** Wavelength dependent attenuation coefficient  $\alpha_{att}$  of the crystal "Sheldon II" as calculated from the measured transmissivity. For further details, see figure 6.1

## 6.2 The Monte-Carlo Refractive Index Matching Technique

The Monte-Carlo Refractive Index Matching Technique (MCRIM) is a combination of experiments and MC simulations to determine the input parameters for the simulations of heavy inorganic scintillators [68]. These parameters which are difficult to measure directly are: the intrinsic light yield  $N_0$ , and the scattering

and absorption coefficients  $\alpha_{scat}$  and  $\alpha_{abs}$ , respectively.

First the attenuation coefficient  $\alpha_{att} = \alpha_{abs} + \alpha_{scat}$  of the crystal has to be measured. Thereafter, it is only necessary to determine the ratio  $B = \frac{\alpha_{scat}}{\alpha_{abs}}$  and the intrinsic light yield  $N_0$ .

The measured light yield (MLY) of a scintillating crystal is defined as the product of the intrinsic light yield  $N_0$  and the light collection efficiency  $\eta$  of the setup in which the crystal is placed. In general,  $\eta$  is dependent on a number of parameters such as the geometry of the crystal and the setup, as well as the optical properties of the materials used in the experiment:

$$MLY = N_0\eta(\text{optical properties, geometry, ...}) \quad (6.4)$$

As the measured light yield is dependent on both  $B$  (given by the optical properties) and  $N_0$ , they cannot be determined in a single experiment. However, by taking the ratio of the measured light yields  $MLY_1$  and  $MLY_2$  from two distinctive measurements with different collection efficiencies  $\eta_1$  and  $\eta_2$  the dependence on  $N_0$  can be eliminated:

$$R_{1/2} = \frac{MLY_1}{MLY_2} = \frac{\eta_1}{\eta_2} \quad (6.5)$$

The MCRIM experimental setup comprises the crystal which properties are to be determined and a photomultiplier tube (PMT) placed together into a light-tight box. A small gap between the crystal and the window of the PMT offers the possibility of introducing materials of different refractive indices. The ratio  $R_{1/2}$  can then be obtained if the crystal is excited with a radioactive source and the light yield is measured with two different materials in the gap. The experimental setup is designed to minimize the presence of optical components such as unpolished surfaces and non-ideal reflectors, which are difficult to simulate. MC simulations that iterate the value of  $B$  can then be used to match the measured ratio  $R_{1/2}$ . Having determined  $B$  in this way, the collection efficiency  $\eta$  can be calculated by the MC, and using equation 6.4 it is possible to deduce the intrinsic light yield.

### 6.2.1 Experimental and MC Setup

For the light-yield measurements an ETL 9305KB photomultiplier [90] was used. This PMT model is well suited for scintillation spectroscopy and single photon counting. The quantum efficiency of the cathode at the peak of the  $CaWO_4$  scintillation spectrum is  $\sim 25\%$ . In addition, the PMT exhibits a low dark count rate of  $\sim 500Hz$ , a fast single electron rise time of  $\sim 3ns$ , a relatively high gain of  $\sim 10^6$  and a good single electron peak to valley ratio of  $\sim 2$  [91]. The PMT was placed into a light-tight box (see figure 6.4). To minimize reflective surfaces in the setup and to ensure that only light directed towards the PMT window is detected

the box was coated with black felt on the inside. In addition, the PMT itself was wrapped in black tape. The absence of reflecting surfaces in the setup improves the reliability of the MC simulation. A small, well defined gap between crystal and PMT is simply realized by laying two thin wires ( $d = 0.04mm$ ) like rails onto the PMT window (see figure 6.4). The anode signal of the PMT is directly sampled (sampling rate  $1GHz$ ) by an "Acqiris DC282" data acquisition system [92] using an internal trigger. The recorded pulses of  $50\mu s$  length with  $1\mu s$  pre-trigger are then saved to hard disk and can be analyzed off-line.

The measurements were performed with the crystal "Sheldon II" which was placed onto the thin wires and excited with a  $^{241}Am$  gamma-ray source. The dominant gamma rays emitted by this source have an energy of  $59.5keV$ . At first a measurement was performed just with air ( $n_{air} = 1$ ) between the PMT and the crystal. For the second measurement the gap was filled with G608N refractive index matching gel ( $n_{gel} = 1.46$ ) from Thorlabs [93]. Care has to be taken to ensure that the amount of gel or water present completely fills the crystal-PMT gap also outside the wires, but not beyond the rim of the crystal. Studies demonstrated that if the presence of excess or shortage of material is not avoided it can lead to discrepancies of up to 30% in the MLY [86]. The ratio  $R_{air/gel}$  is defined as the measured light yield with air divided by the light yield measured with the gap filled with the gel:

$$R_{air/gel} = \frac{MLY(n_{air})}{MLY(n_{gel})} \quad (6.6)$$

The parameters used for the simulation of the setup are shown in table 6.1. The parameters of the PMT were taken from the data sheet [91]. In addition, the thickness of the window of the PMT was implemented as  $1mm$ . The quantum efficiency of the PMT cathode as well as the scintillation spectrum of the  $CaWO_4$  crystal that were implemented in the simulation are depicted in figure 6.5. The parameters for the scintillation spectrum were taken from a measurement at RT of a crystal from SRC "Carat" [86]. The light yield in the simulations was fixed at  $N_0 = 20000ph/MeV$  which is the approximate value where the yet to be determined real value can be expected. As mentioned above the ratio  $R_{air/gel}$  is independent of  $N_0$ . The attenuation coefficient of the crystal was entered as the value calculated in section 6.1 for  $2.88eV$  ( $430nm$ ). MC studies showed that the MLY would vary by only 1% even if  $\alpha_{att}$  varies by 20% [86], meaning it has been measured with sufficient precision for the purpose of the MCRIM technique. The refractive index of the crystal was again calculated by equation (5.1) in the same way as in the simulations in chapter 5. Running the simulation, the crystal is irradiated from one side by  $59.5keV$  gammas with random directions and the scintillation photons are detected by the PMT cathode.

6. Characterization of the Self-Grown  $\text{CaWO}_4$  Crystals

---



**Fig. 6.3:** Experimental setup of the MCRIM technique: A light-tight box containing the PMT, crate with electronics, and the data acquisition system.

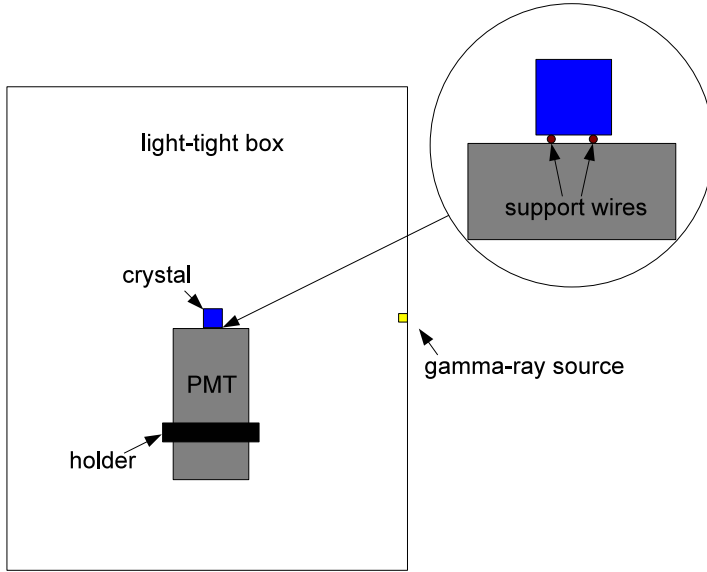


**Fig. 6.4:** Schematic drawing of the experimental setup of the MCRIM technique which comprises a PMT placed into a light-tight box. The crystal is placed onto the PMT window and excited with a gamma-ray source. Two thin wires between the crystal and the PMT build a small, well defined gap with the possibility of introducing materials of different refractive indices.

<b>CaWO<sub>4</sub></b>	
light yield	20,000ph/MeV
scintillation spectrum mean	2.88eV [86]
scintillation spectrum FWHM	0.32eV [86]
attenuation coefficient	0.3348cm <sup>-1</sup>
<b>PMT window</b>	
thickness	1mm
diameter	78mm (3") [91]
refractive index	1.49 [91]
<b>PMT cathode</b>	
active diameter	70mm [91]
quantum efficiency <sup>2</sup>	25%@2.88eV [91]

**Tab. 6.1:** Parameters of the *CaWO<sub>4</sub>* crystal and the PMT used for the simulation of the MCRIM setup.

<sup>2</sup>Dependent on the photon energy see figure 6.5.

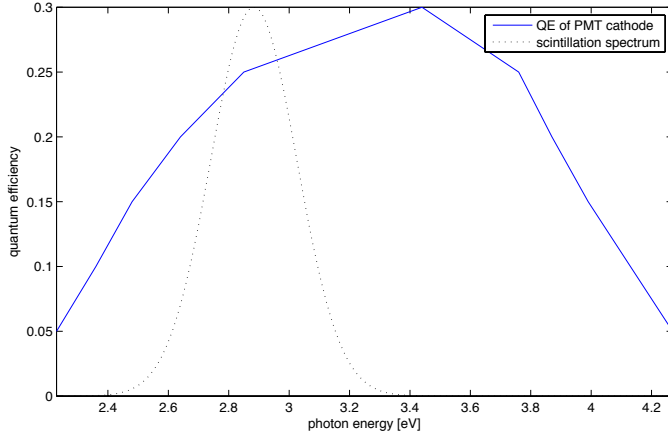


**Fig. 6.5:** Quantum efficiency of the PMT cathode (solid blue line) implemented in the simulation. For comparison the implemented scintillation spectrum (dashed black line) is also shown.

## 6.2.2 Photon Counting Technique

In order to compare the MLY to the simulation it is necessary to determine the number of detected photons in each scintillation event. Since  $\text{CaWO}_4$  has a rather slow decay time constant (see section 4.2) and the low-energy gammas of the  $^{241}\text{Am}$  source produce only few photons this can be realized by counting the individual photoelectrons (p.e.) in each anode pulse.<sup>3</sup> For this purpose a simple code was written in Matlab which analyzes the recorded PMT pulses.

Figure 6.7 shows an example of a measured scintillation pulse. Each spike corresponds to a single scintillation photon that was absorbed in the PMT cathode and generated a photoelectron which was then multiplied in the dynode chain. In the analyzation of each pulse at first the data from the pre-trigger is used to determine the baseline and a possible offset is corrected by subtracting its mean value from every data point. To determine the number of photoelectrons a simple peak-detection function was used which compares each data point to its neighboring values. This function returns only data points above a certain threshold that are larger than both of their neighbors and have a specified minimal distance. For the latter a value of  $6ns$  was chosen which is the approximate half width of a single p.e. pulse and avoids the double counting of pulses with two local maxima (see figure 6.6). For the minimal peak height a value of  $3000a.u.$  was chosen which ensures a threshold above the noise of the baseline while most of the p.e. pulses remain counted (see figure 6.7). With these values the peak-detection function was

<sup>3</sup>Concerning pileup of single photons in the PMT pulses see appendix A.

tested on a number of scintillation events and no mismatch was observed.

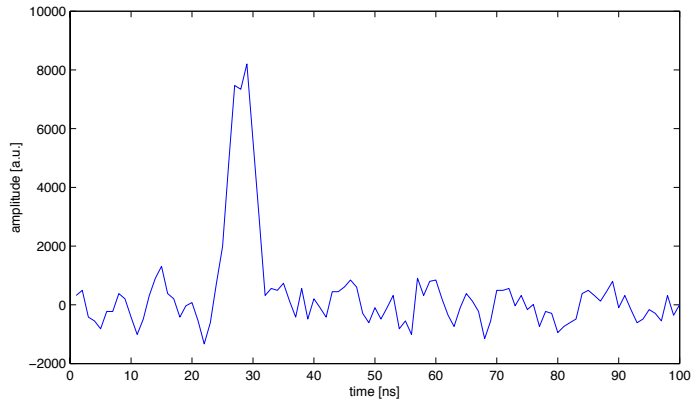


**Fig. 6.6:** Recorded single p.e. pulse with two local maxima. To avoid double counting only points with a minimal distance of  $6ns$  are returned by the peak-detection function.

## 6. Characterization of the Self-Grown $\text{CaWO}_4$ Crystals

---

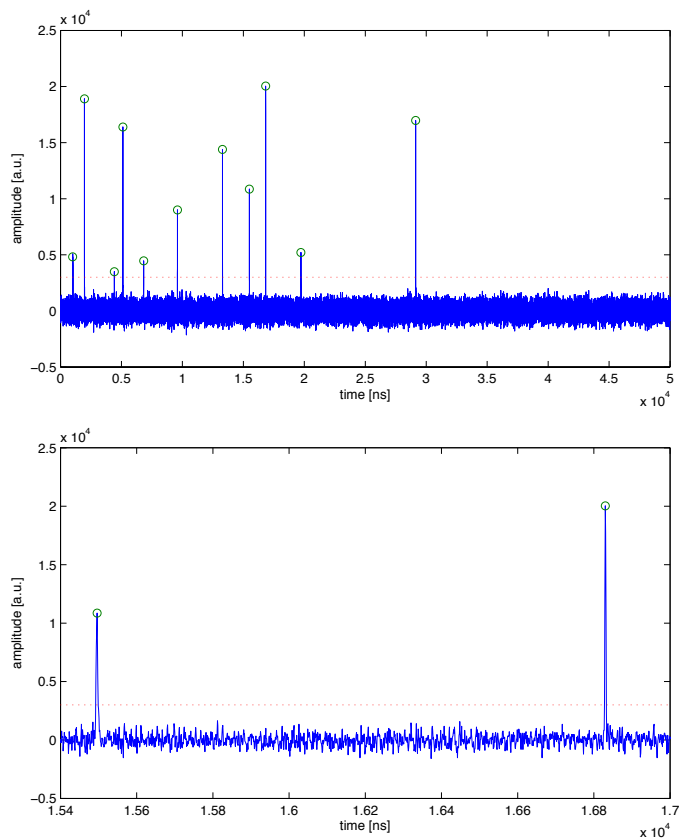


**Fig. 6.7:** Recorded PMT pulse of a scintillation event (top) and zoom in on some of the single p.e. pulses (bottom). The dashed red line indicates the threshold for the peak-detection function. The recognized peaks are marked by the green circles.

### 6.2.3 Results and Discussion

#### Experimental determination of $R_{air/gel}$

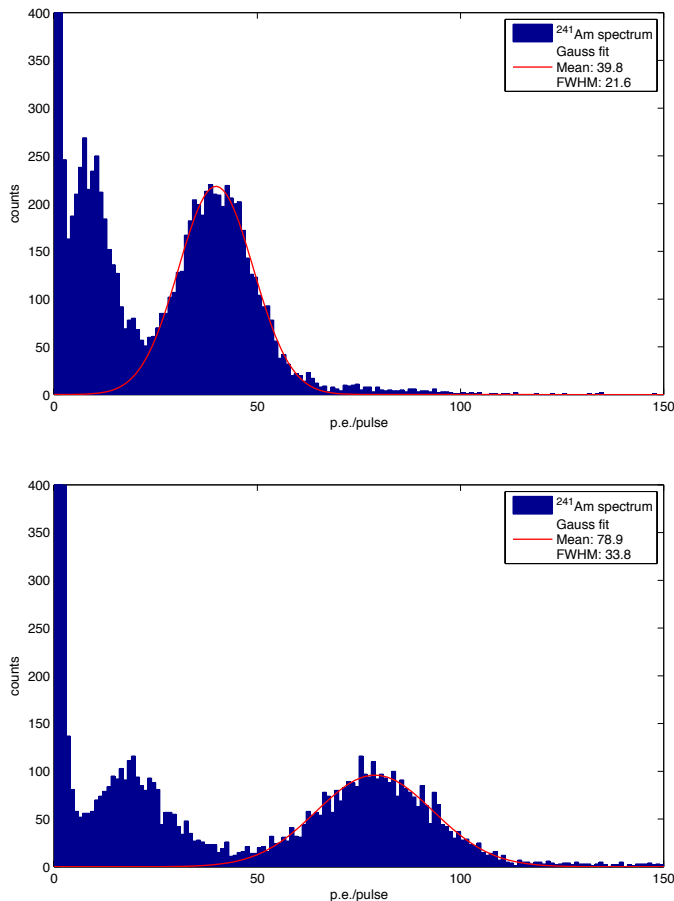


**Fig. 6.8:** Measurement of a  $^{241}\text{Am}$  spectrum in the MCRIM setup with air (top) and with gel (bottom) between crystal and PMT. The photopeak at  $59.5\text{keV}$  was fitted by a single Gaussian to obtain the MLY. The peak on the left results from a mixture of discrete x-rays while the exponentially increasing background to the left of this peak is due to "dark noise" from the PMT.

Figure 6.8 shows two recorded spectra with the gap between crystal and PMT filled by air and gel. The peak on the right is the photopeak of the  $59.5\text{keV}$  gammas from the  $^{241}\text{Am}$  source. The peak on the left results from a mixture of discrete x-rays while the exponentially increasing background to the left of this peak is due to "dark noise" from the PMT. The few events above the  $59.5\text{keV}$

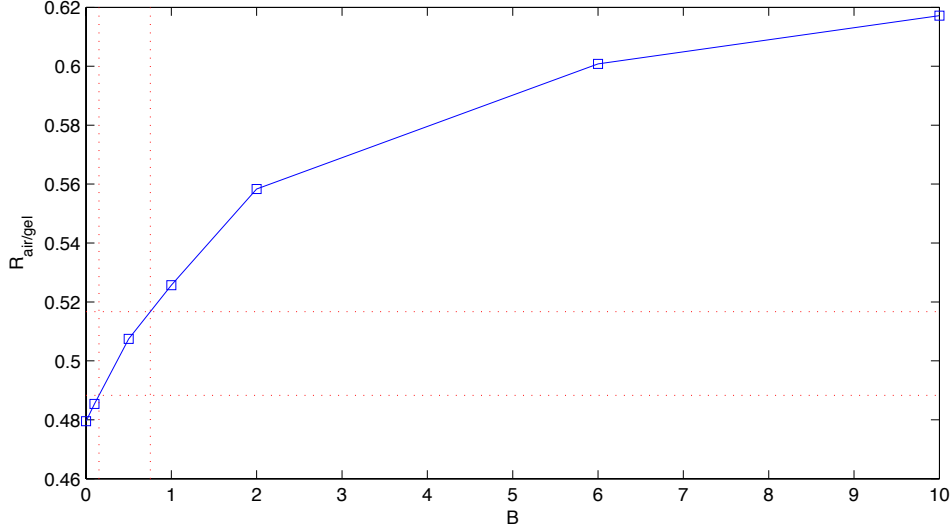
peak originate from atmospheric muons and natural radioactive background. In each measurement the MLY is defined as the peak position of a single-Gaussian fit to the photopeak at  $59.5\text{keV}$  while the first peak in the spectrum was neglected (see figure 6.8).

Material in gap	MLY (p.e.)
Air	$39.9 \pm 0.7$
Gel	$79.3 \pm 1.7$

**Tab. 6.2:** Results of the MCRIM measurements with the gap between crystal and PMT filled by air and gel. The mean values and errors of the MLY were each calculated from the repetition of four measurements.

Table 6.2 shows the results of the measurements. The mean values of the MLY were each calculated from the repetition of four measurements. The given errors are the statistical errors at 95% confidence level calculated from these repetitions and result from slight differences in, e.g., the positioning and surface cleanliness of the crystal in the measurements. The ratio  $R_{air/gel}$  determined from the measurements is

$$R_{air/gel} = 50.3 \pm 1.4\%.$$

Determination of  $B$  through MC matching


**Fig. 6.9:** Simulations of the ratio  $R_{air/gel}$  for different values of  $B$ . The dashed (red) horizontal lines indicate the experimentally determined range of the value  $R_{air/gel}$ . The corresponding limits of  $B$  (dashed (red) vertical lines) are determined by the intersection of the horizontal lines with the graph from the simulation.

Figure 6.9 shows the results of the ratio  $R_{air/gel}$  from simulations of the setup with different values for  $B = \frac{\alpha_{scat}}{\alpha_{abs}}$ . The MLY in each simulation was also defined by the peak position of a single-Gaussian fit to the photopeak in the simulated spectrum. The value of  $B$  can be deduced by comparing the results with the measured ratio  $R_{air/gel}$ . The error on  $B$  (vertical lines) is evaluated by the intersection of the experimental error lines (horizontal lines) with the simulation curve. This places  $B$  in a range from 0.15 to 0.75. The best value for  $B$  is taken as the mean between the two values:

$$B = 0.45 \pm 0.30$$

Since  $\alpha_{att} = \alpha_{abs} + \alpha_{scat} = 0.3348 \pm 0.0255 \text{cm}^{-1}$ , the scattering and absorption lengths can be calculated:

$$L_{scat} = \alpha_{scat}^{-1} = 9.57 \pm 4.36 \text{cm}$$

$$L_{abs} = \alpha_{abs}^{-1} = 4.34 \pm 0.90 \text{cm}$$

### Determination of $N_0$ through MC matching

The intrinsic light yield  $N_0$  can now be deduced by requiring the simulated light yield to match the MLY in the case that the gap is filled by air. To find the errors on  $N_0$ , simulations were carried out using the limits of  $B$  as input parameters (see table 6.3 and figure 6.10). This provides the range of collection efficiencies which is used to derive the range of the intrinsic light yield. The best estimate of the intrinsic light yield is taken as the mean of the extreme values:

$$N_0 = 24800 \pm 3300 \text{ ph/MeV}$$

It should be pointed out that since the refractive index and scintillation spectrum used as input parameters for the simulation were not measured directly there is some additional uncertainty in the determined values. However, since the error on  $B$  is rather large they can probably be neglected. Furthermore, for a typical dark count rate of  $500 \text{ Hz}$  [91] the expected number of dark counts in the recorded pulses of  $50 \mu\text{s}$  length is  $500 \text{ s}^{-1} \cdot 50 \cdot 10^{-6} \text{ s} = 0.0025$  and can therefore be neglected. However, the MLY might be underestimated because the introduced threshold in the photon counting function leaves some less amplified photoelectron pulses uncounted. In addition, besides the slow decay time constant of  $\text{CaWO}_4$  and the low-energy gammas of the  $^{241}\text{Am}$  source some pileup of single photons in the measured PMT pulses can occur (see appendix A).

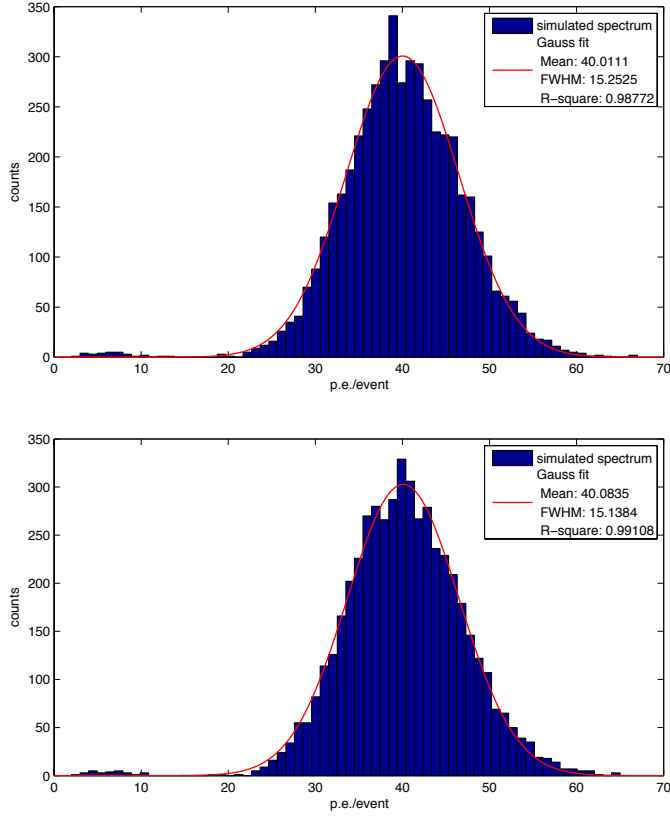


**Fig. 6.10:** Simulated spectrum of  $59.5\text{keV}$  gammas for the MCRIM setup with air in the gap. For the top figure the parameter  $B = 0.15$  was used in the simulation and for the bottom figure  $B = 0.75$ . The light yield  $N_0$  was determined in such a way that that the fit to the spectrum gives the best match to the MLY of  $39.9\text{p.e.}$

$B$	$N_0$ (ph/MeV)	simulated MLY (p.e.)
0.15	28,100	40.0
0.75	21,500	40.1

**Tab. 6.3:** Results of the MC simulations carried out to determine the values for the intrinsic light yield  $N_0$ . To find the errors on  $N_0$ , the simulations were carried out using the limits of  $B$  as input parameters.

## 6.2.4 Testing the Obtained Values

### Prediction of the MLY with the gap filled with silicon oil

To confirm the validity of the simulation input parameters determined with the MCRIM technique a measurement was performed with the gap filled by silicon oil DC 200 ( $n = 1.405$ ). The result was compared to the prediction of the MC simulation.

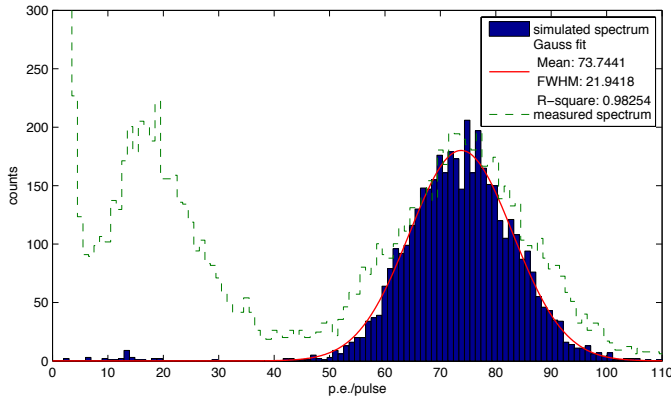


**Fig. 6.11:** Comparison of the simulated (dark blue histogram, red line) and measured spectrum (dashed green line) of the MCRIM setup with silicon oil in the gap. As input parameters for the simulation the values determined with the MCRIM technique were used. The position of the simulated photopeak at  $59.5\text{keV}$  matches the one in the measured spectrum. The x-rays that lead to the left peak in the measured spectrum were not implemented in the simulation.

Figure 6.11 shows the simulated spectrum of this setup, the predicted MLY is  $73.7p.e.$ . The MLY determined experimentally by the repetition of four measurements is  $72.9 \pm 1.5p.e.$  which is in good agreement with the value predicted by the MC simulation. Figure 6.11 also shows the spectrum from one of the measurements scaled to a similar count rate. The position of the peak does coincide with that from the simulation but it is broader. The main reason for this broadening is that the simulation does not take into account the intrinsic resolution of the PMT (caused by the signal amplification through the dynode chain). The x-rays that lead to the left peak in the measured spectrum were not implemented in the simulation.

### Prediction of the MLY for other crystals from the same ingot

A second test of the predictions of the simulation was performed with the differently shaped crystals "Sheldon III" (cylinder) and "Sheldon IV" (truncated pyramid) (see section 4.1). Under the assumption that all of these crystals have the same optical properties since they were cut from the same ingot it should be possible to predict their MLY when the correct dimensions of the crystals are entered in the simulation.

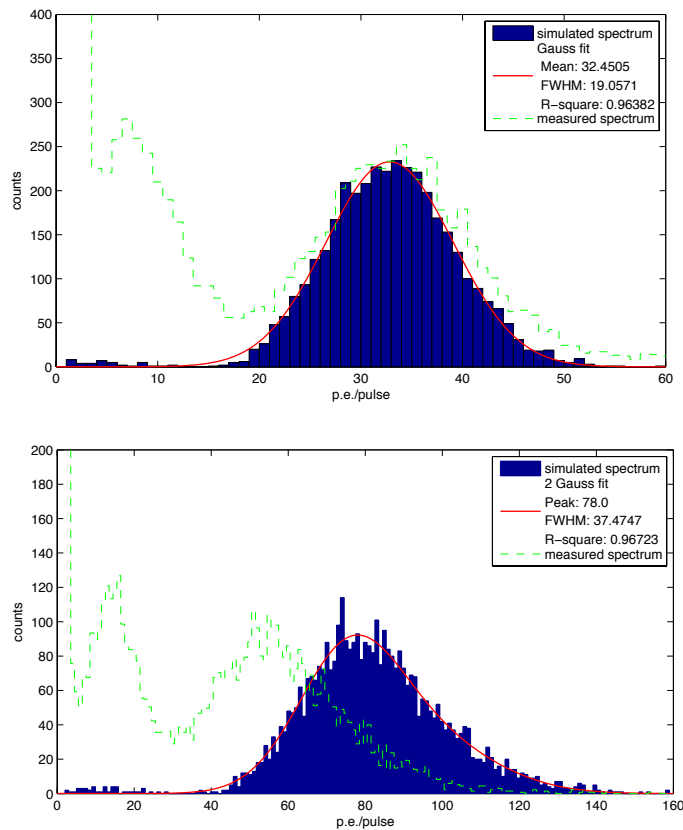


**Fig. 6.12:** Comparison of the simulated (dark blue histogram, red line) and measured spectra (dashed green line) for the crystals "Sheldon III" (top) and "Sheldon IV" (bottom). To determine the MLY the spectra of the crystal "Sheldon III" were fitted by single-Gaussians. The spectra of the crystal "Sheldon IV" had to be fitted by double-Gaussians due to the non-uniformity caused by the "focussing effect" which also leads to a higher collection efficiency.

Figure 6.12 shows the simulated spectra for the crystals "Sheldon III" and "Sheldon IV" when the gap between crystal and PMT is filled by air. The MLY

predicted for "Sheldon III" was again obtained from a single-Gaussian fit to the simulated spectrum. The simulated spectrum for the crystal "Sheldon IV" (truncated pyramid), however, has to be fitted by a double-Gaussian. This is caused by the non-uniformity of the light collection due to the "focussing effect" which, however, also leads to a higher collection efficiency (see sections 4.4 and 5.3). Therefore the simulated MLY of the crystal "Sheldon IV" is increased compared to the other two crystals (see table 6.4).

crystal	simulated MLY (p.e.)	MLY (p.e.)
Sheldon III	32.4	$32.3 \pm 0.4$
Sheldon IV	78.0	$52.9 \pm 1.3$

**Tab. 6.4:** Test of the predictions of the simulations for the differently shaped crystals "Sheldon III" (cylinder) and "Sheldon IV" (truncated pyramid) which were cut from the same ingot. For the crystal "Sheldon III" the MLY of the simulation and the experiment are in good agreement while for the crystal "Sheldon IV" the predicted MLY is  $\sim 47\%$  too high.

Table 6.4 summarizes the results of the measurements performed with the crystals "Sheldon III" and "Sheldon IV" with air in the crystal-PMT gap in comparison to those of the simulations of the setup. The mean values and errors were again each calculated from the repetition of four measurements. For the crystal "Sheldon III" the predicted MLY is in very good agreement with the measurement. However, for the crystal "Sheldon IV" the predicted value is  $\sim 47\%$  higher than the experimental one. This discrepancy can be assigned to a difference in the optical parameters ( $N_0$ ,  $L_{abs}$ ,  $L_{scat}$ ) compared to the other crystals. Possible reasons might be that the light yield of the crystal is decreased due to a local oxygen deficiency in the part of the ingot where the crystal was cut from. In addition, the small cloudy enclosures found in the crystal (see section 4.1) might lead to additional absorption. Furthermore, a difference in the surface quality of the crystal could also lead to the observed discrepancy.

Examples of the measured spectra are shown in figure 6.12 in comparison to the simulated ones. It can be seen that for the crystal "Sheldon IV", apart from the position, the shape of the photopeak at  $59.5\text{keV}$  resembles the shape of the simulated spectrum. For the determination of the MLY this peak was also fitted by two Gaussians while the photopeak of the crystal "Sheldon III" could be fitted by a single Gaussian. In addition, similar to the simulations, the MLY of the crystal "Sheldon IV" is increased compared to the other two crystals. This suggest that the simulation is qualitatively right and that the features of the measured spectrum of the crystal "Sheldon IV" can also be explained by the "focussing effect".

## 6.3 Light-Yield Measurements of Differently Shaped Crystals and Housings

In order to experimentally compare the light collection of differently shaped crystals in differently shaped housings, as suggested by the MC simulations in section 5.3, the crystals "Sheldon II" (block shaped), "Sheldon III" (cylinder) and "Sheldon IV" (truncated pyramid) were mounted in a reflective housing which was then placed onto the PMT window in the MCRIM setup (see figure 6.13). For the crystal "Sheldon III" a cylindrical housing was used while the other two crystals were mounted in a box-shaped housing (see figure 6.14). The reflective housings are made of aluminum and covered with 3M radiant mirror film VM2000<sup>4</sup> on the inside, the crystals are fixed by small holders made of polyethylene. The scintillation photons can escape through a hole with a diameter of  $25\text{mm}$  at the bottom of the housing which is facing the PMT window (see figures 6.13 and 6.14). The geometry of this setup is similar to that of a CRESST-like detector module, although with smaller dimensions. However, contrary to a CRESST-like detector module, the PMT can only detect light from one side and the holders cover a larger fraction of the crystal's surface. The crystals were again excited by a  $^{241}\text{Am}$  source and the photon counting software described in section 6.2.2 was used to analyze the recorded PMT pulses.

---

<sup>4</sup>The VM2000 foil is the progenitor of the VM2002 foil and has very similar optical properties (see [21]).

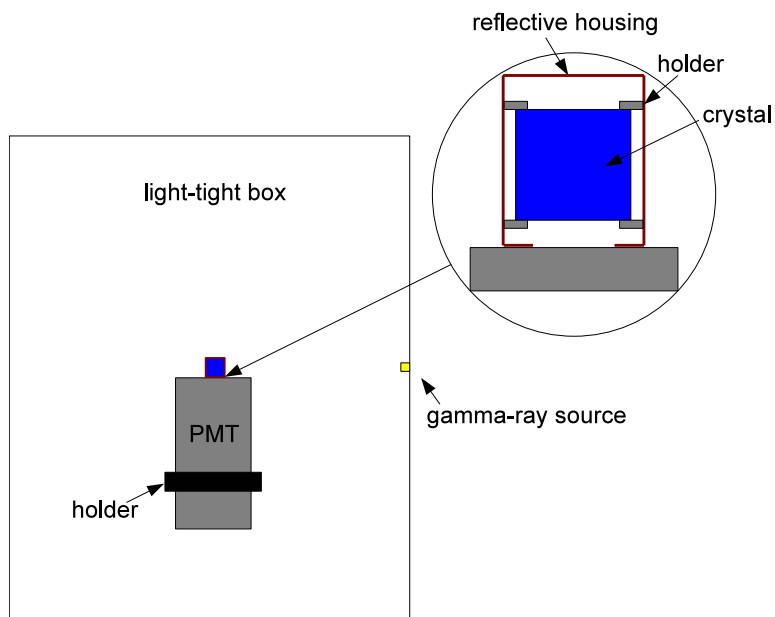


**Fig. 6.13:** Schematic drawing of the setup for the light-yield measurements. The reflective housing in which the crystal is mounted is placed onto the PMT window of the MCRIM setup.

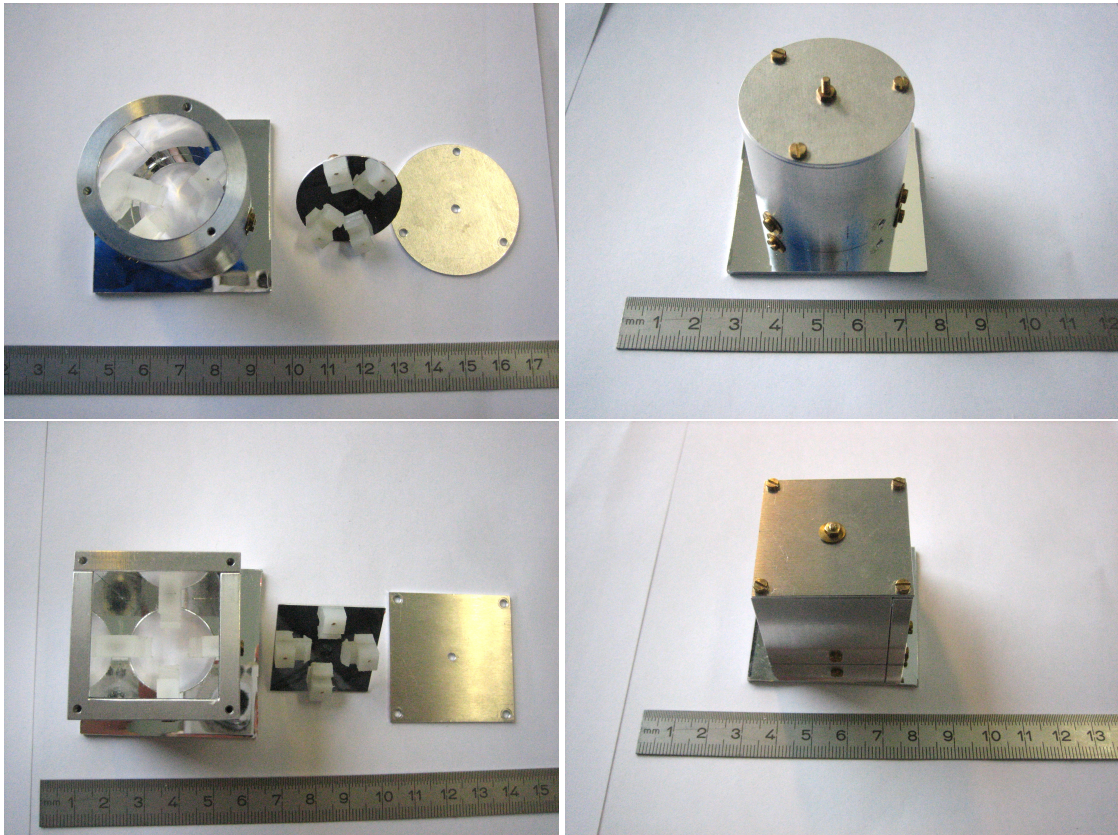


**Fig. 6.14:** Cylindrical (top) and box-shaped (bottom) reflective housing used for the light-yield measurements. The crystals are fixed by small holders made of polyethylene and the inside of the housing is covered with a highly reflective foil. The scintillation light can escape through a hole in the bottom of the housing which is facing the PMT window.

### 6.3.1 Results and Discussion

In each recorded spectrum the MLY and FWHM are defined as the peak position and full width at half maximum of a Gaussian fit to the  $59.5\text{keV}$  photopeak from the  $^{241}\text{Am}$  source. The resolution of this peak is defined as the ratio  $\text{FWHM}/\text{MLY}$ . The mean values and errors were again calculated each from the repetition of four measurements.

#### Polished crystals before annealing

Table 6.5 shows the results of the measurements with the differently shaped crystals as they were obtained from the crystal laboratory. The crystals' surfaces were all polished and they were *not* annealed under oxygen atmosphere. In figure 6.15

## 6. Characterization of the Self-Grown $\text{CaWO}_4$ Crystals

---

examples of the recorded spectra for each module are shown. In contrast to the measurements in section 6.2 the second peak at lower energies that originates from a mixture of x-rays (see figure 6.8) is not visible because the x-rays cannot penetrate the reflective housing.

<b>module</b>	a)	b)	c)
<b>crystal</b>	Sheldon II (block shaped)	Sheldon III (cylinder)	Sheldon IV (truncated pyramid)
<b>reflective housing</b>	box	cylinder	box
<b>MLY (p.e.)</b>	$32.0 \pm 0.7$	$30.8 \pm 0.9$	$52.3 \pm 0.8$
<b>FWHM (p.e.)</b>	$16.6 \pm 0.4$	$16.2 \pm 0.5$	$27.3 \pm 0.4$
<b>FWHM/MLY (%)</b>	$51.8 \pm 1.7$	$52.6 \pm 2.0$	$52.5 \pm 0.7$

**Tab. 6.5:** Results of the light-yield measurements of differently shaped crystals in different reflective housings. The mean values and errors were each calculated from the repetition of four measurements. In each recorded spectrum the MLY and FWHM was determined by a single-Gaussian fit to the  $59.5\text{keV}$  photopeak. For module c) the MLY is increased by  $\sim 67\%$ . However, due to the also increased FWHM it shows no improved resolution FWHM/MLY compared to the other modules.

### 6.3. Light-Yield Measurements of Differently Shaped Crystals and Housings

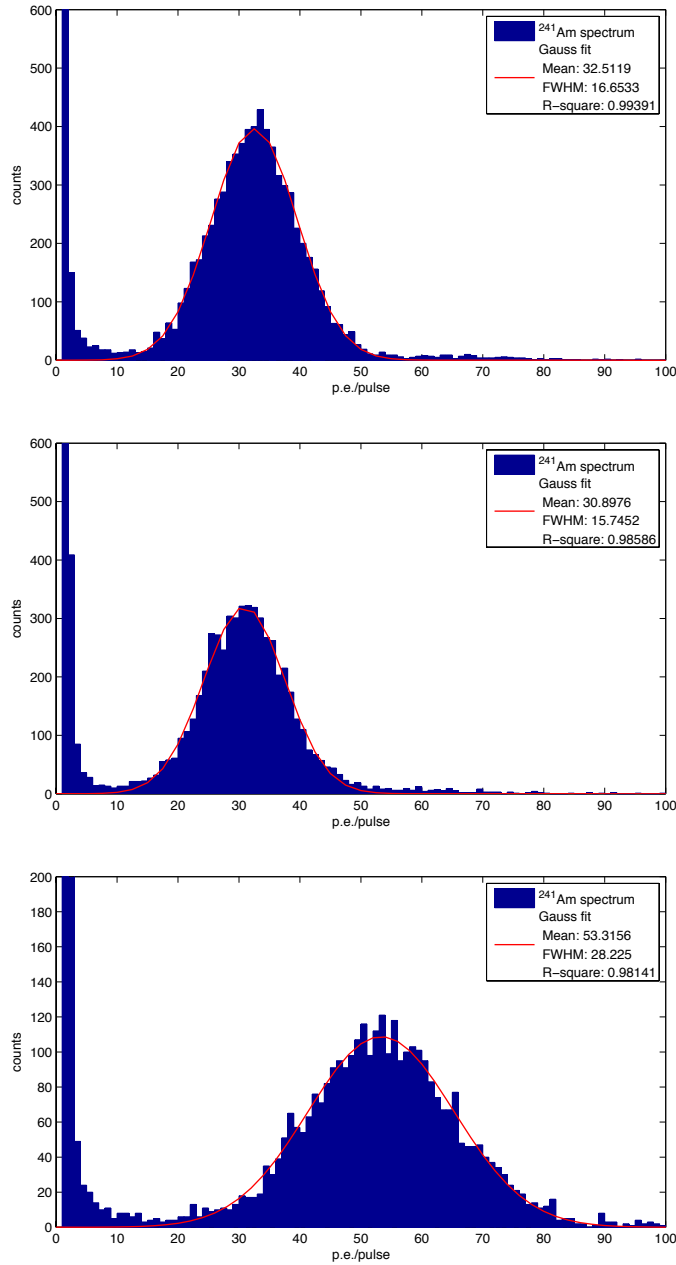


**Fig. 6.15:**  $^{241}\text{Am}$  spectra measured with modules a), b), c) (from top to bottom) (see also table 6.5). The second peak at lower energies that originates from a mixture of x-rays (see figure 6.8) is not visible because the x-rays cannot penetrate the reflective housing.

In the measurements the MLY of module a) is slightly increased compared to

module b) but the values agree within errors. For module c) the MLY is increased by  $\sim 67\%$ . However, due to the also increased FWHM it shows no improved resolution. The simulations in section 5.3 and measurements in section 6.2 showed that this is due to the "focussing effect" which increases the efficiency but also the non-uniformity of the light collection. In contrast to the measurements in the previous section though, the spectrum of the crystal "Sheldon IV" can be fitted by a single-Gaussian which indicates that the light collection is more uniform if the crystal is mounted in the reflective housing.

### Crystals after roughening of the surface facing the PMT

To test the effects of roughening experimentally the crystals were measured again after one surface had been roughened using boron carbide powder with a grain size of  $\sim 4 - 14\mu\text{m}$ . For these measurements the crystals were mounted in the reflective housing with the roughened surface facing the PMT window as is the case in CRESST-II where the light detector faces the roughened surface. Examples of the measured spectra are shown in figure 6.16, the results are summarized in table 6.6.

module	a)	b)	c)
crystal	Sheldon II (block shaped)	Sheldon III (cylinder)	Sheldon IV (truncated pyramid)
reflective housing	box	cylinder	box
MLY (p.e.)	$31.0 \pm 0.6$	$36.8 \pm 0.7$	$51.3 \pm 0.6$
FWHM (p.e.)	$16.2 \pm 0.3$	$18.0 \pm 0.3$	$24.1 \pm 0.6$
FWHM/MLY (%)	$52.2 \pm 0.6$	$48.9 \pm 0.7$	$47.0 \pm 0.8$

**Tab. 6.6:** Results of the light yield measurements after the crystal's surface facing the PMT was roughened. Other details as in table 6.5. For module a) roughening had no significant influence on the measured spectrum while for module b) it led to an increase of the MLY by  $\sim 19\%$ . For module c) roughening reduces the FWHM by  $\sim 12\%$  whereas the MLY is kept constant within errors.

### 6.3. Light-Yield Measurements of Differently Shaped Crystals and Housings

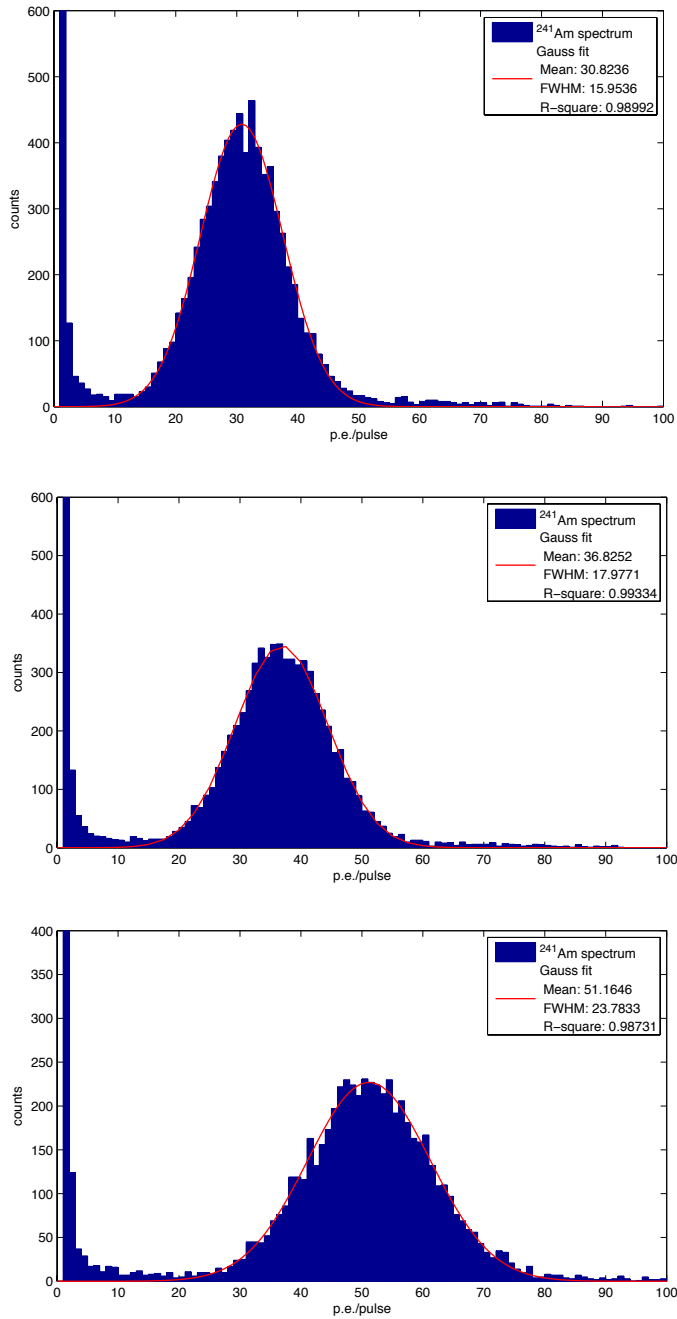


**Fig. 6.16:**  $^{241}\text{Am}$  spectra measured with modules a), b), c) (from top to bottom) (see also table 6.6) after roughening of the crystal's surface facing the PMT.

It can be seen that in module a) roughening of the block-shaped crystal had no significant influence on the MLY or resolution. In module b), however, roughening

led to an increase of the MLY and resolution by  $\sim 19\%$  and  $\sim 7\%$ , respectively. The result cannot be directly compared to the simulations in section 5.2. However, it rather suggests that the simulation model of a roughened surface is insufficient as it only leads to a significant increase of the light collection for crystals with a much smaller attenuation coefficient (see section 5.2). This may be assigned to the fact that in contrast to the simulation, in the experiment roughening does mainly increase the transmission through the roughened surface itself. In module c) roughening reduces the FWHM of the photopeak by  $\sim 12\%$ , whereas the MLY is kept constant within errors which leads to an improved resolution by  $\sim 10\%$ . This confirms the results obtained from the simulations in section 5.3 that roughening can reduce the non-uniformity that arises from the "focussing effect". However, experimentally the effect is not as prominent as in the simulations and some of the non-uniformity remains because the measured FWHM of the photopeak is still increased compared to the modules a) and b).

### Crystals after annealing

After roughening the crystals were annealed under oxygen atmosphere for  $48h$  at  $1450^\circ\text{C}$ . After this procedure all crystals appeared optically clearer and the crystals "Sheldon II" and "Sheldon III" showed a very light green hue. In addition, the roughened surface became smoother during the annealing. Table 6.7 shows the results of the light-yield measurements with the annealed crystals. Examples of the recorded spectra are shown in figure 6.17.

module	a)	b)	c)
crystal	Sheldon II (block shaped)	Sheldon III (cylinder)	Sheldon IV (truncated pyramid)
reflective housing	box	cylinder	box
MLY (p.e.)	$38.4 \pm 0.6$	$32.7 \pm 0.7$	$60.2 \pm 0.4$
FWHM (p.e.)	$18.9 \pm 0.2$	$17.6 \pm 0.9$	$30.1 \pm 0.2$
FWHM/MLY (%)	$49.1 \pm 1.4$	$54.0 \pm 1.7$	$50.1 \pm 0.6$

**Tab. 6.7:** Results of the light yield measurements after annealing of the crystals. Other details as in table 6.5. For modules a) and c) the MLY is increased by  $\sim 24\%$  and  $\sim 17\%$ , respectively. In module b), however, the MLY shows an decrease by  $\sim 11\%$  compared to the measurements before annealing.

### 6.3. Light-Yield Measurements of Differently Shaped Crystals and Housings

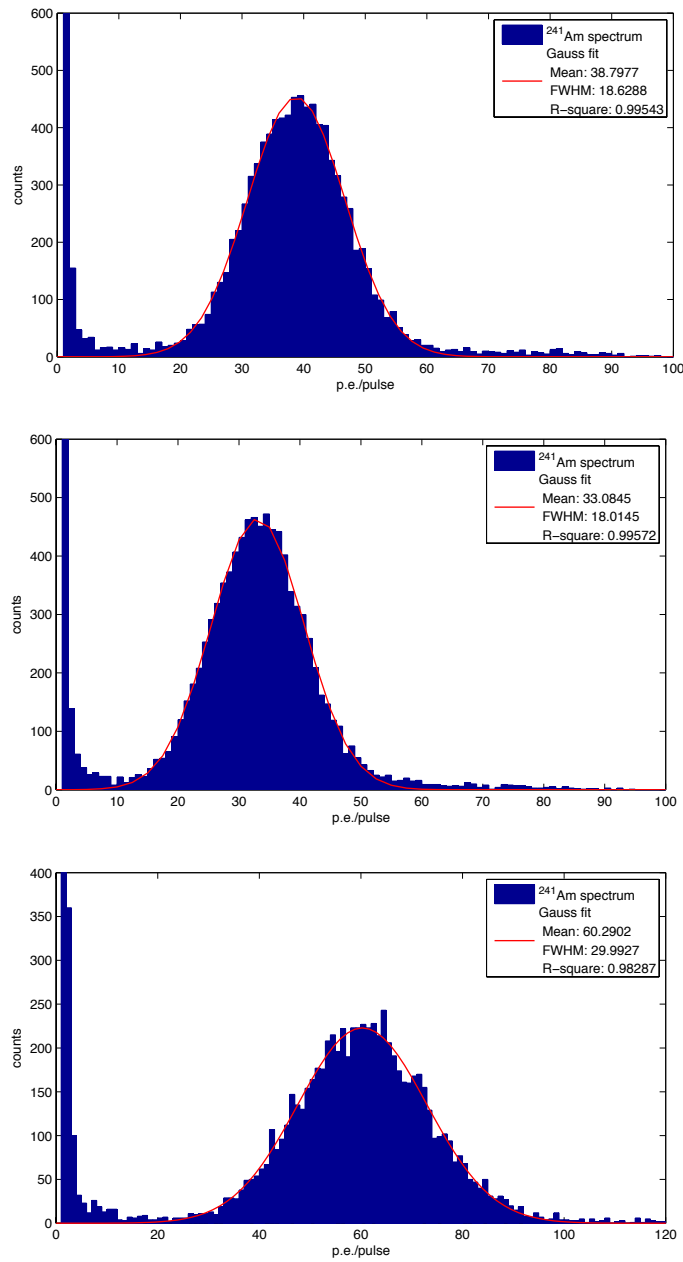


**Fig. 6.17:**  $^{241}\text{Am}$  spectra measured with modules a), b), c) (from top to bottom) (see also table 6.7) after annealing the crystals.

For module a) the annealing process led to an increase of the MLY and an improved resolution by  $\sim 24\%$  and  $\sim 6\%$ , respectively. In module b), however, the MLY shows a decrease by  $\sim 11\%$  compared to the measurements before anneal-

ing. The MLY of module c) is increased by  $\sim 17\%$ . However, because of the also increased FWHM the resolution is worsened by  $\sim 7\%$ . These results suggest that the annealing process did increase the light output of the crystals but also compensated the effects of roughening which originally led to an increase of the MLY in module b) and a decreased FWHM in module c). This is supported by the fact that the roughened surface appeared smoother after annealing. It can also be seen that the increase of the MLY varies by different amounts for the different crystals. In module b) it is only increased by  $\sim 6\%$  compared to that of the polished crystal before annealing.

### Crystals after re-roughening

As the appearance of the roughened surface changed after annealing the roughening was reapplied and the light yield measurements were performed again. The results are shown in table 6.8 and figure 6.18.

module	a)	b)	c)
crystal	Sheldon II (block shaped)	Sheldon III (cylinder)	Sheldon IV (truncated pyramid)
reflective housing	box	cylinder	box
MLY (p.e.)	$43.3 \pm 0.5$	$42.8 \pm 0.9$	$60.6 \pm 0.8$
FWHM (p.e.)	$19.9 \pm 0.4$	$20.0 \pm 0.6$	$28.1 \pm 0.6$
FWHM/MLY (%)	$46.0 \pm 1.0$	$46.7 \pm 1.3$	$46.4 \pm 1.0$

**Tab. 6.8:** Results of the light yield measurements after re-roughening of the crystals. Other details as in table 6.5. For module c) the MLY is increased by  $\sim 40\%$  compared to the other modules. However, due to the also increased FWHM it shows no improved resolution.

### 6.3. Light-Yield Measurements of Differently Shaped Crystals and Housings

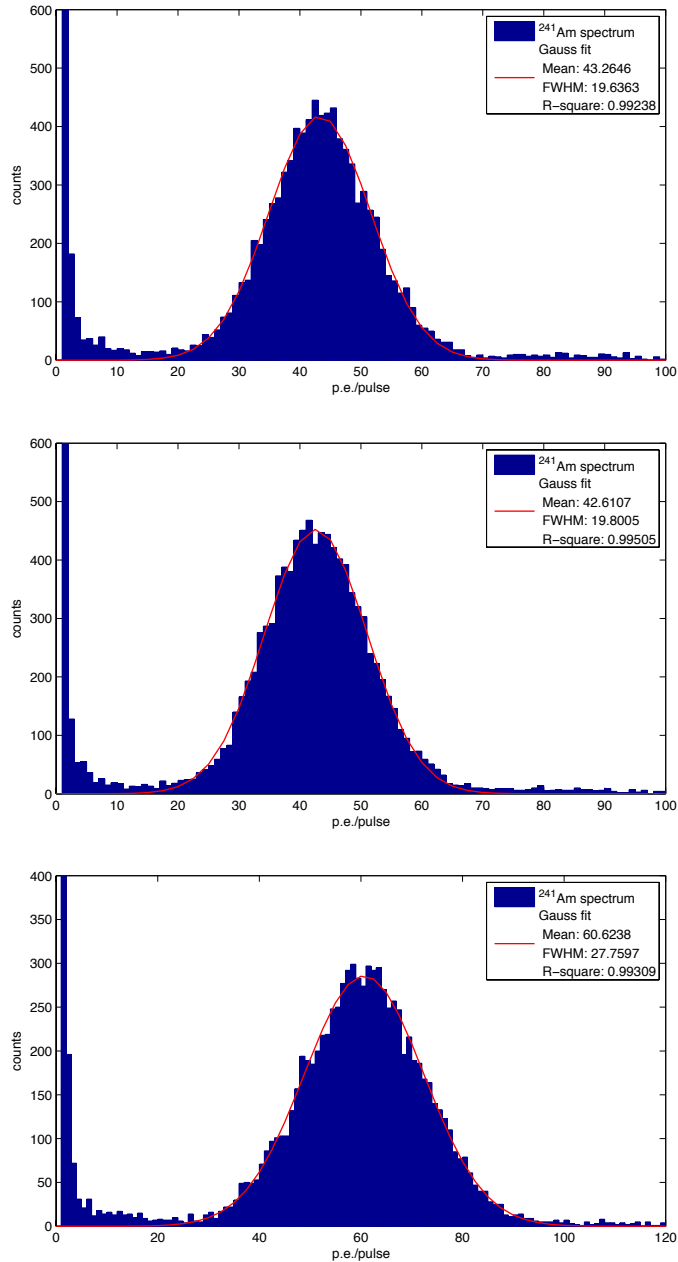


**Fig. 6.18:** Measured  $^{241}\text{Am}$  spectra with module a), b), c) (from top to bottom) (see also table 6.8) after re-roughening of the annealed crystals.

In this final comparison of the different modules it can be seen that the MLY of module a) and b) is comparable while the MLY of module c) is increased by  $\sim 40\%$ . However, also the FWHM of module c) is increased so that it shows no

improved resolution. Another interesting result is that for module a) the MLY is increased by  $\sim 13\%$  after the roughening is reapplied while no changes were observed after roughening of the unannealed crystal. This may be assigned to the fact that annealing decreases the attenuation coefficient of the crystal which increases the relative amount of trapped light that is removed by a roughened surface (see section 5.2).

Since in the measurements the resolution of all modules is equal within errors it has to be decided by means of other criteria (e.g. achievable close packing) which of them should be favored as a future detector design.

### 6.3.2 Influence of the Position of the Irradiating Source

In the measurements described in the previous section the crystals were irradiated from the side (see figure 6.13). Since the gammas are stopped near the crystal surface there is only little variation in the radial position of the scintillation events. To test the influence of the radial dependence of the light collection the modules were also measured with the source placed above the module (see figure 6.19).

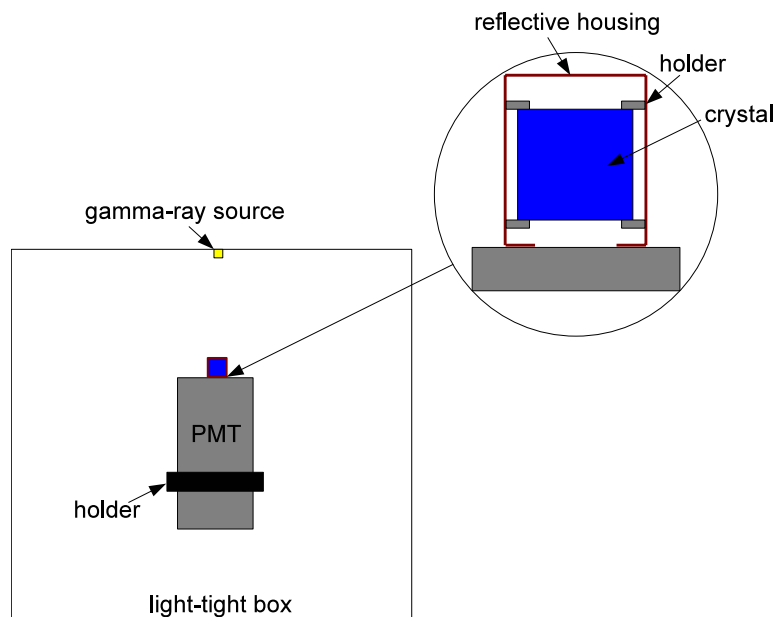


**Fig. 6.19:** Schematic drawing of the setup for the light-yield measurements with the source placed above the crystal to test the influence of the radial dependence of the light collection on the measured spectra.

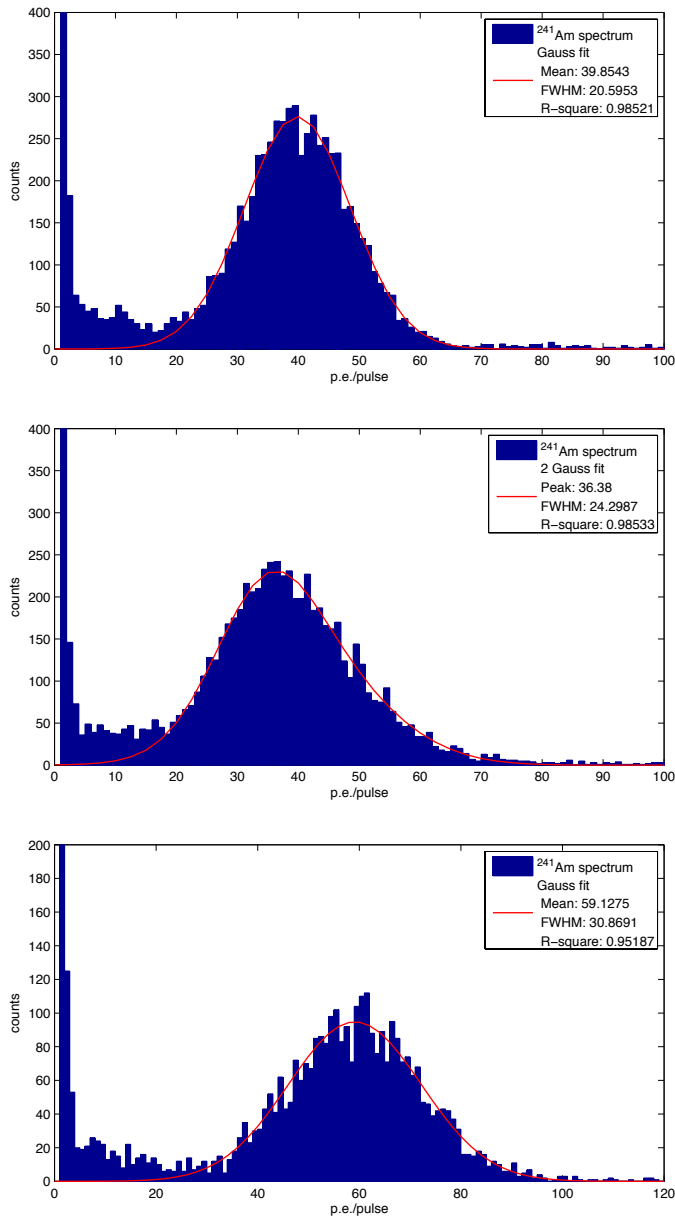
### Crystals after annealing

Table 6.9 and figure 6.20 show the results of the crystals after annealing as in table 6.7 and figure 6.17 but with the gamma-ray source placed above the module.

module	a)	b)	c)
crystal	Sheldon II (block shaped)	Sheldon III (cylinder)	Sheldon IV (truncated pyramid)
reflective housing	box	cylinder	box
MLY (p.e.)	$40.2 \pm 0.4$	$36.3 \pm 0.4$	$59.3 \pm 0.4$
FWHM (p.e.)	$20.8 \pm 0.4$	$24.2 \pm 0.3$	$29.4 \pm 1.5$
FWHM/MLY (%)	$51.9 \pm 0.6$	$66.5 \pm 1.4$	$49.7 \pm 2.7$

**Tab. 6.9:** Results of the light yield measurements as in table 6.7 when the crystal is irradiated from the top. For modules a) and c) the different irradiation causes only little changes to the measured spectra. For module b) the resolution is worsened by  $\sim 23\%$  compared to the measurement with the irradiation from the side.

## 6. Characterization of the Self-Grown $\text{CaWO}_4$ Crystals



**Fig. 6.20:**  $^{241}\text{Am}$  spectra measured with modules a), b), c) (from top to bottom) as in figure 6.17 when the crystal is irradiated from the top. The measured spectra of modules a) and c) can be fitted by single-Gaussian while the spectrum of module b) has to be fitted by a double-Gaussian.

It can be seen that for module a) and c) the different irradiation causes only little changes to the measured spectrum. For module b), however, the MLY and more prominently the FWHM are significantly increased compared to the mea-

surement where the crystal is irradiated from the side which ultimately leads to a worsened resolution by  $\sim 23\%$ . This can be assigned to the radial dependence of the fraction of trapped light which increases with distance from the cylinder axis (see sections 4.3 and 5.1). Therefore the different radial positions of the scintillation events lower the mean fraction of trapped light but lead also to an additional non-uniformity. The measured spectrum in this case does not show a doublet structure like in the simulations depicted in figure 5.6, however, it is also better fitted by two Gaussians (see figure 6.17).

These results support the fact obtained from the simulations in section 5.3 that the light collection in a block shaped crystal is more uniform compared to the cylinder as the fraction of trapped light does not show a large radial dependence on the position of the scintillation event.

### Crystals after re-roughening

module	a)	b)	c)
crystal	Sheldon II (block shaped)	Sheldon III (cylinder)	Sheldon IV (truncated pyramid)
reflective housing	box	cylinder	box
MLY (p.e.)	$44.8 \pm 0.7$	$46.5 \pm 0.4$	$60.7 \pm 0.2$
FWHM (p.e.)	$21.5 \pm 0.3$	$24.4 \pm 0.3$	$27.9 \pm 0.5$
FWHM/MLY (%)	$48.0 \pm 0.7$	$52.6 \pm 0.8$	$45.9 \pm 0.9$

**Tab. 6.10:** Results of the light yield measurements as in table 6.8 when the crystal is irradiated from the top. For modules a) and c) the different irradiation causes only little changes to the measured spectra. For module b) the resolution is worsened by  $\sim 13\%$  compared to the measurement with the irradiation from the side.

## 6. Characterization of the Self-Grown $\text{CaWO}_4$ Crystals

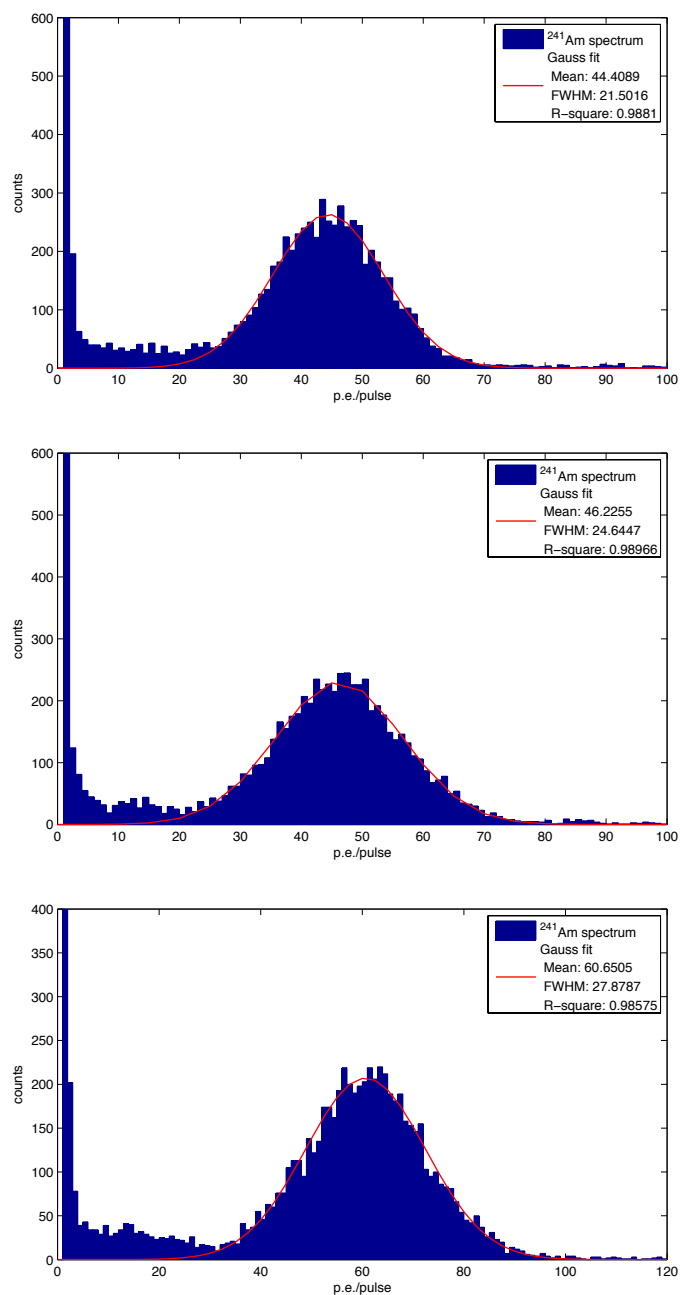


**Fig. 6.21:**  $^{241}\text{Am}$  spectra measured with modules a), b), c) (from top to bottom) as in figure 6.18 when the crystal is irradiated from the top. In contrast to the previous measurement depicted in figure 6.20 the measured spectrum of module b) can now be fitted by a single-Gaussian.

Table 6.10 and figure 6.21 show the results of the crystals after annealing and re-roughening as in table 6.8 and figure 6.18 but with the gamma-ray source placed above the module. For modules a) and c) the spectra do not change significantly if they are irradiated from the top for module b) however the resolution is worsened by  $\sim 13\%$ . This can be assigned to the fact that some of the radial dependence of the fraction of trapped light in module b) remains after roughening. However, in contrast to the previous measurement depicted in figure 6.20 the measured spectrum can now be fitted by a single-Gaussian.

In this final comparison the measurements favor module c) where the resolution is improved by  $\sim 13\%$  compared to module b). Module a) shows a resolution improved by  $\sim 9\%$  compared to module b). However the crystal "Sheldon II" in module a) has a factor of  $\sim 2.4$  higher mass compared to the crystal "Sheldon IV" in module c) which makes it more suited for the close packing of the detector modules. Furthermore, in comparison to a truncated pyramid a block-shaped crystal will be easier to manufacture and less material will be lost from the original ingot. Therefore module a) appears as a favorable design for future detectors.

## 6.4 Comparison of the MLY to the Reference Crystal "Boris"

For the  $CaWO_4$  crystals that are used in CRESST-II the light yield at RT is usually compared to a reference crystal from SRC "Carat" named "Boris". This crystal is cylindrical with  $40mm$  in diameter and height as those employed in the experiment. As the measured light yield depends on the dimensions of the crystal and it has yet not been possible to produce a cylindrical crystal with  $40mm$  in diameter and height at the crystal laboratory of the TUM (see section 4.1), the MLY of the self-grown crystals cannot be directly compared to "Boris". With the simulation input parameters determined in section 6.2, however, it is possible to compare the MLY of "Boris" in the MCRIM setup (see figure 6.4) to a simulation for a self-grown crystal with the same dimensions.

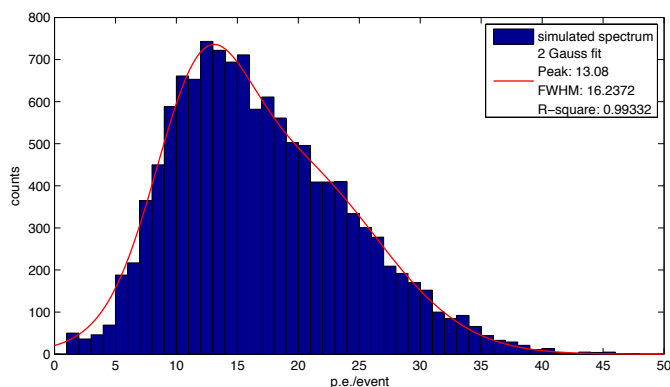
### 6.4.1 Results and Discussion

Figure 6.22 shows the simulated spectrum of  $59.5keV$  gammas in the MCRIM setup with air between the crystal and the PMT. The crystal was implemented as a cylinder with  $40mm$  diameter and height with the same parameters for  $L_{abs}$ ,  $L_{scat}$  and  $N_0$  that were determined in section 6.2 for the self-grown crystal "Sheldon II" prior to the annealing under oxygen atmosphere. The predicted MLY from this simulation is  $13.1p.e.$ . It can be noticed that the photopeak in the spectrum has

## 6. Characterization of the Self-Grown $\text{CaWO}_4$ Crystals

---

to be fitted by a double-Gaussian. This can be assigned to the non-uniformity which arises from the low absorption length leading to a decreased light collection for scintillation events with larger distance to the PMT.



**Fig. 6.22:** Simulated spectrum of  $59.5\text{keV}$  gammas for a cylindrical crystal with  $40\text{mm}$  diameter and height in the MCRIM setup with air between the crystal and the PMT. As simulation input parameters the values determined in section 6.2 for the self-grown crystal "Sheldon II" were used. To determine the MLY, the spectrum was fitted by a double-Gaussian.

For the measurements, the crystal "Boris" was placed in the MCRIM setup on the thin wires on the PMT window and was irradiated from one side with the  $^{241}\text{Am}$  source. Figure 6.23 shows one of the measured spectra with the  $59.5\text{keV}$  photopeak fitted by a single Gaussian to determine the MLY. Table 6.11 shows the results from the repetition of four measurements. In comparison, the simulated MLY of the self-grown crystal is only  $\sim 37\%$  of that measured for "Boris". However, the light output can be increased by up to a factor of 2 after the annealing under oxygen atmosphere [21].

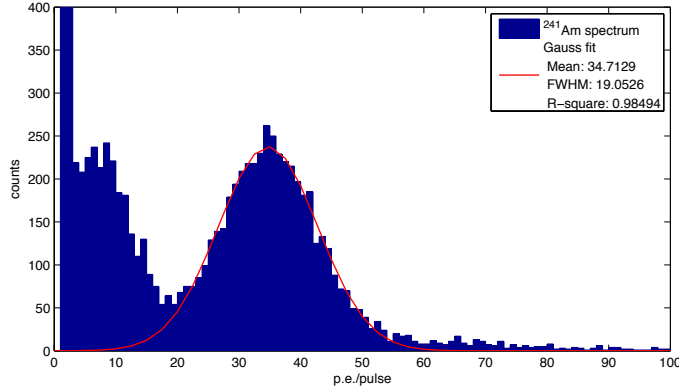


**Fig. 6.23:** Measured  $^{241}\text{Am}$  spectrum for the crystal "Boris" in the MCRIM setup with air between the crystal and the PMT. The MLY was determined by a single-Gaussian fit to the measured spectrum.

crystal	Boris	simulated crystal
MLY (p.e.)	$35.1 \pm 0.4$	13.1
FWHM (p.e.)	$19.2 \pm 0.4$	16.2
FWHM/MLY (%)	$54.8 \pm 1.2$	124

**Tab. 6.11:** Results of the light yield measurements of the reference crystal Boris in comparison to the simulation of a self-grown crystal.

## 6.5 Measurement of the Radiopurity

To determine the radiopurity of a self-grown  $\text{CaWO}_4$  crystal it was screened with a high-resolution Ge detector in our shallow underground lab ( $\sim 15m.w.e.$ ). For this measurement a cylindrical crystal of  $25mm$  diameter and  $57mm$  height with a mass of  $202g$  was used. The measurement lasted for 12 days. The recorded spectrum showed no lines above the background, i.e. no signs of radioactive contamination. From this measurement upper limits on the absolute activities of certain radionuclides were derived (see tables 6.12 and 6.13) [94].

6. Characterization of the Self-Grown  $CaWO_4$  Crystals

---

<i>isotope</i>	<i>CaWO<sub>4</sub> crystal</i>
<b>K-40</b>	$< 90.7^{+8.4}_{-7.4} \cdot 10^{-3} \text{ Bq/kg}$ $< 3.51^{+0.33}_{-0.29} \cdot 10^{-10} \text{ g/g}$
$^{228}\text{Ac}$	$< 27.3^{+2.0}_{-1.8} \cdot 10^{-3} \text{ Bq/kg}$ $< 3.31^{+0.24}_{-0.22} \cdot 10^{-22} \text{ g/g}$
$^{212}\text{Pb}$	$< 24.4^{+3.9}_{-3.7} \cdot 10^{-3} \text{ Bq/kg}$ $< 4.75^{+0.76}_{-0.71} \cdot 10^{-22} \text{ g/g}$
$^{212}\text{Bi}$	$< 120.0^{+9.1}_{-8.0} \cdot 10^{-3} \text{ Bq/kg}$ $< 2.21^{+0.17}_{-0.15} \cdot 10^{-22} \text{ g/g}$
<b>Th-232 chain</b>	$< 30.3^{+1.8}_{-1.6} \cdot 10^{-3} \text{ Bq/kg}$ $< 7.48^{+0.44}_{-0.39} \cdot 10^{-9} \text{ g/g}$
$^{234}\text{Pa}$	$< 309.4^{+28.6}_{-25.2} \cdot 10^{-3} \text{ Bq/kg}$ $< 1.22^{+0.11}_{-0.10} \cdot 10^{-23} \text{ g/g}$
$^{226}\text{Ra}$	$< 642.7^{+61.0}_{-53.8} \cdot 10^{-3} \text{ Bq/kg}$ $< 1.76^{+0.17}_{-0.15} \cdot 10^{-14} \text{ g/g}$
$^{214}\text{Pb}$	$< 37.9^{+2.4}_{-2.2} \cdot 10^{-3} \text{ Bq/kg}$ $< 3.12^{+0.20}_{-0.18} \cdot 10^{-23} \text{ g/g}$
$^{214}\text{Bi}$	$< 59.2^{+3.6}_{-3.1} \cdot 10^{-3} \text{ Bq/kg}$ $< 3.63^{+0.22}_{-0.19} \cdot 10^{-23} \text{ g/g}$
<b>U-238 chain</b>	$< 46.7^{+2.0}_{-1.8} \cdot 10^{-3} \text{ Bq/kg}$ $< 3.75^{+0.16}_{-0.14} \cdot 10^{-9} \text{ g/g}$

**Tab. 6.12:** Upper limits on the absolute activities (given in Bq/kg as well as in g/g at 90%CL) of a self-grown  $CaWO_4$  crystal for the different isotopes from the  $^{232}\text{Th}$ - and the  $^{238}\text{U}$ -decay chains, as well as for  $^{40}\text{K}$ . In the case, that several gamma lines were used for the calculation of the activity of one isotope, the quoted value is the weighted average of the single activities. The limits given for the whole decay chains are again the weighted averages of the activities of the different isotopes.

<i>isotope</i>	<i>CaWO<sub>4</sub> crystal</i>
<sup>235</sup> U	$< 334.6^{+30.3}_{-26.6} \cdot 10^{-3} \text{ Bq/kg}$ $< 4.18^{+0.38}_{-0.33} \cdot 10^{-9} \text{ g/g}$
<sup>231</sup> Pa	$< 474.6^{+73.1}_{-67.8} \cdot 10^{-3} \text{ Bq/kg}$ $< 2.71^{+0.42}_{-0.39} \cdot 10^{-13} \text{ g/g}$
<sup>227</sup> Th	$< 546.8^{+105.8}_{-101.5} \cdot 10^{-3} \text{ Bq/kg}$ $< 4.81^{+0.93}_{-0.89} \cdot 10^{-19} \text{ g/g}$
<sup>219</sup> Rn	$< 118.2^{+14.2}_{-13.3} \cdot 10^{-3} \text{ Bq/kg}$ $< 2.46^{+0.30}_{-0.28} \cdot 10^{-25} \text{ g/g}$
<sup>211</sup> Pb	$< 65.0^{+6.7}_{-6.0} \cdot 10^{-3} \text{ Bq/kg}$ $< 7.12^{+0.74}_{-0.66} \cdot 10^{-23} \text{ g/g}$
<b>U-235 chain</b>	$< \mathbf{93.9^{+5.5}_{-4.9}} \cdot 10^{-3} \text{ Bq/kg}$ $< \mathbf{1.17^{+0.69}_{-0.61}} \cdot 10^{-9} \text{ g/g}$

**Tab. 6.13:** Upper limits on the absolute activities (given in Bq/kg as well as in g/g at 90%*CL*) of a self-grown *CaWO<sub>4</sub>* crystal for the different isotopes from the <sup>235</sup>U-decay chain. Other details as in table 6.12.

## 6.6 Summary and Consequences for New Detectors

### Light yield and optical parameters of the self-grown crystals

In this chapter the attenuation coefficient of the self-grown *CaWO<sub>4</sub>* crystal "Sheldon II" was determined with a transmission measurement prior to the annealing under oxygen atmosphere. The obtained value  $\alpha_{att} = 0.3348 \pm 0.0255 \text{ cm}^{-1}$  at 430nm is by a factor of  $\sim 3$  higher than that measured for a crystal from SRC "Carat" [86].

This value for  $\alpha_{att}$  was used to determine the intrinsic light yield  $N_0$  and the absorption and scattering length  $L_{abs}$  and  $L_{scat}$  of the crystal with a combination of experiments and MC simulations (MCRIM technique). The determined values  $L_{scat} = 9.57 \pm 4.36 \text{ cm}$  and  $L_{abs} = 4.34 \pm 0.90 \text{ cm}$  suggest that absorption is

dominant over scattering in the crystal. The determined intrinsic light yield was  $N_0 = 24800 \pm 3300 \text{ph}/\text{MeV}$  at  $59.5 \text{keV}$  which is  $\sim 9\%$  higher than that measured for the already mentioned crystal from SRC "Carat" [86].

These values show that the unannealed crystal "Sheldon II" has a relatively high intrinsic light yield. However due to the large attenuation coefficient and the small ratio of scattering to absorption a large fraction of the scintillation photons will be absorbed before escaping the crystal (quasi trapping).

The determined parameters  $L_{abs}$ ,  $L_{scat}$  and  $N_0$  were tested for the crystal "Sheldon II" and two differently shaped crystals that were cut from the same ingot by comparing the measured light yield (MLY) of an experiment with the prediction of a MC simulation. For the crystal "Sheldon II" (block shaped) and "Sheldon III" (cylinder) the predictions of the simulation were in good agreement with the measurements. The predicted MLY for the crystal "Sheldon IV" (truncated pyramid) though was  $\sim 47\%$  too high. This suggests that even for crystals from the same ingot the optical parameters can show some variation making it impossible to correctly predict their MLY with the same simulation input parameters. The small cloudy enclosures found in some of the crystals (see section 4.1) might be an explanation for this discrepancy.

## Comparison of differently shaped crystals and housings

The differently shaped crystals (block shaped, cylinder, truncated pyramid) were mounted into differently shaped reflective housings (cylinder, box shaped), as suggested by the MC simulations, and excited with  $59.5 \text{keV}$  gammas from a  $^{241}\text{Am}$  source while the scintillation light was detected by a photomultiplier (PMT). The different modules were then compared regarding their MLY and resolution of the photopeak.

For these measurements the crystals were annealed under oxygen atmosphere and the surface facing the PMT had been roughened. This procedure increased the MLY and resolution by  $\sim 16 - 39\%$  and  $\sim 11 - 12\%$ , respectively, depending on the crystal shape. It was further observed that the resolution of all modules was comparable when they were irradiated from the side. However, when irradiated from the top the resolution of the crystal "Sheldon III" (cylinder) mounted in a cylindrical housing worsened by  $\sim 13\%$  while this had no significant effect on the other crystals. This can be assigned to the radial dependence of the fraction of trapped light in a cylindrical crystal, which leads to a less uniform light collection (see section 5.2).

The MLY of the crystal "Sheldon II" (block-shaped) in a box shaped housing is comparable to that of the cylindrical crystal and housing, however, it shows a more uniform light collection and the resolution is improved by  $\sim 9\%$ . This confirms the results obtained from the MC simulations in section 5.3 which also favor the

block-shaped crystal and housing over the cylindrical module due to its more uniform light collection.

The MLY of the crystal "Sheldon IV" (truncated pyramid) in a box-shaped housing was increased by  $\sim 30 - 40\%$  depending on the irradiation compared to the cylindrical module. However, the resolution was only improved by  $\sim 13\%$  as the taper-shaped cross section leads to an increased but also less uniform light collection. In contrast to the MC simulations in section 5.3, in the measurements the uniformity of the light collection was only slightly improved after roughening of the crystal.

As the crystal "Sheldon II" (block-shaped) has a factor of  $\sim 2.4$  higher mass compared to the crystal "Sheldon IV" (truncated pyramid) it is more suited for close packing of the detector modules. Furthermore, in comparison to a truncated pyramid a block-shaped crystal will be easier to manufacture and less material will be lost from the original ingot.

### Comparison to the reference crystal "Boris"

The light yield of the crystal "Boris" that is used as a reference for the CRESST-II experiment was measured and compared to a simulation which uses the values for  $L_{abs}$ ,  $L_{scat}$  and  $N_0$  that were determined for the self-grown crystal "Sheldon II" before the annealing under oxygen atmosphere. Here the simulated MLY was  $\sim 37\%$  of that measured for "Boris". Since the crystal "Sheldon II" was not annealed under oxygen this value can still be increased significantly.

### Investigation of the radiopurity

The investigation of the radiopurity of one of self-grown crystals with a high-resolution Ge detector revealed no signs of radioactive contamination.

### Consequences for new detectors

Due to the relatively high intrinsic light yield of the self-grown  $CaWO_4$  crystals it seems feasible to use them in the CRESST and future EURECA experiments. Furthermore the radiopurity measurement showed no signs of radioactive contamination. To obtain a sufficient light output from crystals with dimensions as those currently used in CRESST-II or even larger ones it will however be necessary to reach a smaller absorption coefficient  $\alpha_{abs}$  than determined in the measurements. As the value of  $\alpha_{abs}$  was determined for an unannealed crystal this might already be achievable by the annealing process.

The measurements of differently shaped crystals and housings favor a block-shaped

## *6. Characterization of the Self-Grown $\text{CaWO}_4$ Crystals*

---

crystal (with the surface facing the light detector roughened) in a box-shaped housing since it shows the most uniform light collection and can achieve the highest packing density. The energy resolution of this module is improved by  $\sim 9\%$  compared to the cylindrical crystal (with the surface facing the light detector roughened) and housing when it is irradiated from the top. As the crystal shaped like a truncated pyramid showed an increased but also less uniform light collection it offers no significant improvement compared to the block-shaped crystal.

# Chapter 7

## Conclusion and Outlook

The CRESST experiment aims at the direct detection of WIMPs with cryogenic detectors. Of great importance in this rare event search is the background discrimination which is achieved by the simultaneous detection of the phonon signal and the scintillation light of the  $CaWO_4$  targets. A central task in improving the discrimination ability of a detector module will be to achieve a better light collection. Another important issue is to ensure the availability of scintillating crystals that match the special requirements of CRESST and the future EURECA experiment.

### 7.1 Czochralski Growth of $CaWO_4$ Crystals

During this thesis, several  $CaWO_4$  crystals with a mass of  $\sim 250 - 790g$  were produced with a dedicated Czochralski furnace installed at the crystal laboratory of the Technische Universität München (TUM). The growth of large ingots with diameters  $\gtrsim 40mm$ , however, is still challenging. Therefore, a new rhodium crucible with a diameter of  $120mm$  (instead of  $80mm$  diameter of the old crucible) is currently under installation which will allow an easier growth of crystals with a larger diameter. In the future the growth parameters will be further optimized to obtain highly transparent crystals with less defects and a lower absorption coefficient.

### 7.2 Optical and Scintillation Properties of the Self-Grown Crystals

One of the self-grown crystals was characterized prior to the annealing under oxygen atmosphere. The absorption and scattering lengths  $L_{abs}$  and  $L_{scat}$  and the intrinsic light yield  $N_0$  of this crystal were determined by the Monte-Carlo Refractive Index Matching (MCRIM) technique, a combination of experiments and Monte

Carlo simulations. The obtained values  $L_{scat} = 9.57 \pm 4.36 \text{ cm}$ ,  $L_{abs} = 4.34 \pm 0.90 \text{ cm}$  and  $N_0 = 24800 \pm 3300 \text{ ph/MeV}$  show that the crystal has a relatively high intrinsic light yield. However, due to the relatively low value of  $L_{abs}$  and the small ratio  $L_{abs}/L_{scat}$  a large fraction of the scintillation photons will be absorbed before escaping the crystal (quasi trapping).

In addition, the radiopurity of the crystals was investigated with a high-resolution Ge detector which revealed no signs of radioactive contamination [94]. In the future, further measurements with larger crystals and longer exposures will be performed in a new underground laboratory at our institute.

To obtain a sufficient light output from crystals with dimensions as those currently used in CRESST-II or even larger ones, it will be necessary to reach a larger absorption length. This might already be achievable by annealing under oxygen atmosphere. Therefore, the characterization of the crystal should be repeated after the annealing process. In addition, also the refractive index and the scintillation spectrum should be measured to obtain a complete set of simulation input parameters. An experimental setup to measure the scintillation spectrum (under UV excitation) is currently under construction. Furthermore, the light yield at low temperatures ( $< 10 \text{ K}$ ) where it is expected to stay constant should be investigated. A setup for such measurements is available within the CRESST collaboration at the Universität Tübingen. The determined parameters can then be used to simulate new detector geometries like modules with multiple light detectors that face different surfaces of the  $\text{CaWO}_4$  crystal.

The MCRIM setup for the characterization of the crystals can be improved with an additional preamplifier which would allow a clearer distinction of the photoelectron pulses from the noise. In the future the scintillation pulses should be measured integrally which will allow to characterize other materials with faster scintillation decay curves (with time constants  $\lesssim 100 \text{ ns}$ ) where the pileup of single photons is non-negligible. For these measurements the setup should be calibrated with an LED to determine the integrated value of a single-photon pulse measured by the photomultiplier. This will allow the deduction of the absolute light yield in terms of photoelectrons from an integrally measured scintillation pulse. Together with the simulation the setup can also be used to determine the intrinsic light yield and the scattering and absorption coefficients of future self-grown  $\text{CaWO}_4$  crystals or other scintillating materials.

Furthermore, it will also be important to investigate the phonon properties of the self-grown crystals. Therefore, as a next step, a crystal will be equipped with a TES and operated as a cryogenic detector. Such a detector is currently under construction and will be tested at the neutron scattering facility for the quenching factor measurements (see section 2.3.1). This setup can be used to study the performance of a detector module containing both a cryogenic phonon and a cryogenic light detector.

## 7.3 Investigation of Differently Shaped Crystals and Housings

### Monte Carlo simulations

To study the collection of scintillation light Monte Carlo (MC) simulations of a CRESST-like detector module based on GEANT4 have been established. The simulations showed that with the currently used cylindrical crystal, depending on the scattering and absorption lengths, on average  $\sim 12\% - 60\%$  of the scintillation light remains (quasi) trapped inside the crystal. Furthermore, the light collection is not uniform but depends on the radial position of the scintillation event inside the crystal. This spatial dependence can lead to a doublet structure in the measured spectrum of monoenergetic events. The simulation showed that on average a fraction  $\eta \approx 13\%$  of the scintillation light is absorbed by the light detector. The fraction of the energy deposited by a gamma that is detected as scintillation light in the simulation is  $\sim 1.5\%$ , in good agreement with experimental results that showed values of  $\sim 1\%$  [28].

Roughening of the crystal surface that is facing the light detector reduces the mean fraction of (quasi) trapped light to a value of  $\sim 7 - 48\%$  and can also improve the uniformity (i.e. decrease the spatial dependence) of the light collection depending on the absorption and scattering lengths. Experimentally though, the profits of roughening seem even more pronounced than in the simulations.

MC simulations of differently shaped crystals and housings were performed. The results were evaluated regarding the efficiency  $\eta$  and uniformity  $\sigma_\eta$  of the light collection with respect to the position of the scintillation event and compared to the currently used cylindrical crystal, with the planar surface (facing the light detector) roughened, in a cylindrical housing. A good detector should have a high and uniform light collection, i.e. a large value of the ratio  $\eta/\sigma_\eta$ . In these terms the simulations favor a crystal shaped like a truncated pyramid with the large end face (facing the light detector) roughened in a box-shaped housing. For this configuration the ratio  $\eta/\sigma_\eta$  shows an increase by a factor of  $\sim 6.3$ . However, the crystal shape has some disadvantages regarding the close packing of the detector modules since it has similar dimensions but only  $\sim 50\%$  of the volume of the currently used cylinder. As an alternative a block-shaped crystal (with the same volume as the cylinder) in a box-shaped housing offers close packing and exhibits an increase of the ratio  $\eta/\sigma_\eta$  by a factor of  $\sim 2.5$ . Since the ingots produced with the Czochralski method already have a block-like shape (see section 4.1) this would have the additional advantage of losing only little material when the crystals are cut. Furthermore, a block-shaped crystal will be easier to manufacture in comparison to a truncated pyramid.

The MC simulation of the CRESST-like detector module can still be improved by implementing the wavelength-shifting properties of the reflective foil. It would also be desirable to know the foil's reflectivity at low temperatures. As simulation-input parameters for the  $CaWO_4$  crystal the values of  $L_{abs}$ ,  $L_{scat}$  and  $N_0$  determined by the MCRIM technique can be used. For the future, the MC simulation can help to understand the performance of newly developed detector modules like the one with two light detectors or the composite detector design that are employed in the current run of CRESST-II (see section 2). As there probably is some discrepancy between a roughened surface in the simulations and the experimental results other GEANT4 models of surface finishes and other simulation softwares (e.g. LITRANI [95]) should also be tested.

### Light-yield measurements

Differently shaped crystals (block shaped, cylinder, truncated pyramid), as suggested by the MC simulations, were cut from a self-grown ingot. The crystals were mounted into differently shaped reflective housings (cylinder, box shaped) and excited with  $59.5keV$  gammas from a  $^{241}Am$  source while the scintillation light was detected by a photomultiplier. The different modules were then compared regarding the measured light yield (MLY) and resolution of the photopeak.

As a final treatment the crystals were annealed under oxygen atmosphere and the surface facing the photomultiplier was roughened. Both procedures together increased the MLY and improved the resolution by  $\sim 16 - 39\%$  and  $\sim 11\%$ , respectively, depending on the crystal shape.

The measurements favor a block-shaped crystal in a box-shaped housing since it shows the most uniform light collection and can achieve the highest packing density. The resolution of this module is improved by  $\sim 9\%$  compared to the cylindrical crystal and housing. This confirms the results obtained from the MC simulations which also favor the block-shaped crystal and housing due to its more uniform light collection compared to the cylindrical module. The crystal shaped like a truncated pyramid in a box-shaped housing showed an increase of the MLY by  $\sim 35\%$  but a less uniform light collection and therefore no significantly improved resolution in the measurements compared to the block-shaped crystal and housing. In contrast to the MC simulations, in experiment the additional non-uniformity due to the taper-shaped cross section of this crystal could not completely be removed by roughening the surface facing the light detector (see sections 5.3 and 6.3). In the future, it should be tested if a more uniform light collection can be achieved with a different degree of roughness.

## 7.4 Post-Growth Treatment of the Crystals

In the future, the annealing process can be further optimized by controlling the partial pressure of oxygen during the annealing. Furthermore, chemical etching can improve the light output to an even higher degree than mechanical polishing [96]. For  $CaWO_4$  it has been shown that a rough surface finish achieved by annealing under HCl vapor can increase the light output of the crystals by  $\sim 50\%$  [97]. As an alternative it is possible to roughen the crystals with an argon-ion source that is installed in an RF-sputtering magnetron facility at our institute [98]. An especially large increase of the light output can be expected if it will be possible to create a so-called effective medium with a continuously changing refractive index on the crystal surface like in black silicon (see section 4.4).

A novel approach to increase the light output of heavy inorganic scintillators is the concept of photonic crystals (PhC). It has been shown that the problem of total internal reflection in a scintillator with a high refractive index can be partially overcome by machining a thin PhC slab - a periodic pattern of nano-holes - into the exit surface of the material [99]. By this pattern certain modes of the light can be diffracted out of the crystal that would otherwise be totally reflected. In simulations the light output for different scintillating materials was improved by a factor of  $\sim 2$  with this technique [100]. However, the manufacturing process of such a PhC slab is rather complex.

## 7.5 Consequences for New Detectors

It has been possible to produce several  $CaWO_4$  crystals with a high intrinsic light yield that showed no signs of radioactive contamination. With the new crucible, that is currently under installation, the production of crystals with larger dimensions that can be used in CRESST or EURECA seems feasible. To ensure that the crystals really match the special requirements of these experiments, however, it will still be necessary to further investigate their scintillation and *phonon* propagation properties as well as their radiopurity.

Together with the MC simulations the light-yield measurements suggest that a design characterized by a block-shaped crystal in a box-shaped housing should be pursued for future detectors in the experiments CRESST and EURECA. The improved resolution of the light channel that can be achieved with such a module will lead to a better discrimination between different types of recoil events (see section 2.3.1). In addition, a block-shaped crystal is relatively easy to manufacture and has the advantage of losing only little material from the original ingot which also has a block-like shape. Furthermore, the possibility concerning a close packing of the detector modules increases the probability to identify neutron events as

## *7. Conclusion and Outlook*

---

background due to multiple scattering and will allow the installation of a large target mass in the volume of the cryostat. These considerations are of particular importance for CRESST and the future large-scale EURECA experiment.

# Appendices



# Appendix A

## Estimation of the expected pileup in the light yield measurements

Besides the slow scintillation decay curve of  $CaWO_4$  and the low number of detected photons in the light yield measurements in chapter 6 there may be some pileup of single photons in the PMT pulses. The number of photons that remain uncounted because they arrive within a time of  $6ns$ , which was entered as the minimal peak distance in the photon counting software, can be estimated with the MC simulation of the MCRIM setup from section 6.2.

For this purpose the measurement with the largest MLY of  $79.3p.e.$  (see table 6.2) was simulated with the parameters depicted in table 6.1 and the values for  $N_0$ ,  $L_{abs}$  and  $L_{scat}$  determined in section 6.2. In addition, a fast scintillation decay time of  $1.4\mu s$  with a relative amplitude of 30% and a slow decay time of  $9.2\mu s$  with an amplitude of 70% were entered into the simulation. These values were determined for the scintillation decay curve of  $CaWO_4$  at RT under excitation with  $^{60}Co$  gammas [65].

## A. Estimation of the expected pileup in the light yield measurements

---

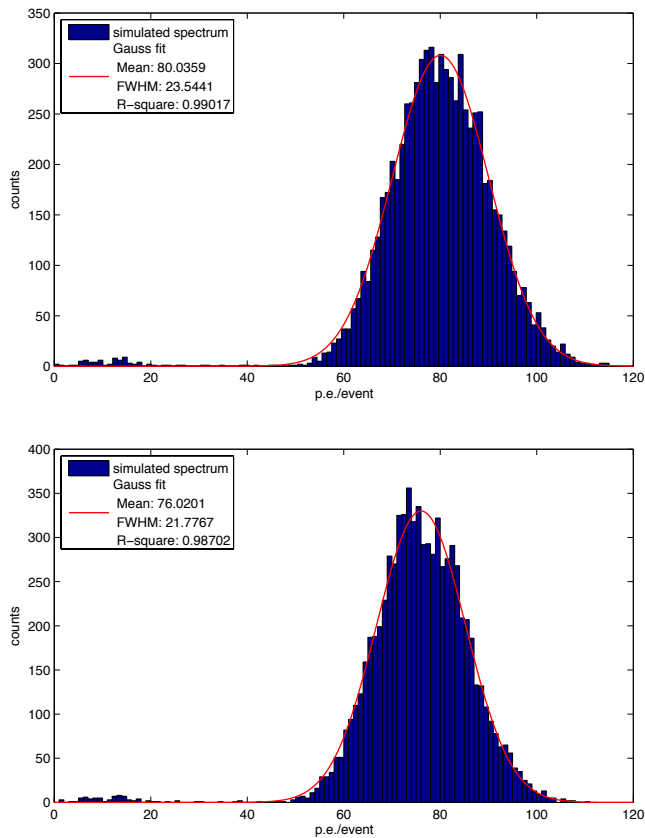


**Fig. A.1:** Simulated spectrum of the measurement depicted in table 6.2 with gel between the crystal and the PMT. The top figure shows the spectrum that is obtained if all detected photons are counted. In the bottom figure all photons that arrive within  $6ns$  after the last counted photon are ignored. This leads to a slight reduction of the position of the photopeak by  $\sim 5\%$ .

Figure A.1 shows the simulated spectrum of the setup irradiated by  $59.5keV$  gammas. The simulated MLY of  $80.0p.e.$  obtained from a Gaussian fit to the photopeak is in good agreement with the experimental value of  $79.3 \pm 1.7p.e.$ . Figure A.1 also shows the spectrum that is obtained if all photons that arrive within a time interval of  $6ns$  after a detected photon are not counted. The MLY determined by a Gaussian fit to this spectrum is  $76.0p.e.$ . Therefore the systematic error introduced in the light yield measurements due to the pileup of single photons is smaller than  $\sim 5\%$ .

# Bibliography

- [1] F. Zwicky, *Helv. Phys. Acta* **6**, 110 (1933).
- [2] K. G. Begeman, A. H. Broeils, and R. H. Sanders, *Mon. Not. R. Astron. Soc.* **249**, 523 (1991).
- [3] D. N. Schramm and M. S. Turner, *Rev. Mod. Phys.* **70**, 303 (1998).
- [4] G. Hinshaw *et al.*, *Astrophys. J. Suppl. Ser.* **180**, 225 (2009).
- [5] E. Komatsu *et al.*, *Astrophys. J. Suppl. Ser.* **180**, 330 (2009).
- [6] D. Clowe *et al.*, *Astrophys. J. Lett.* **648**, L109 (2006).
- [7] M. Bradač *et al.*, *Astrophys. J.* **687**, 959 (2008).
- [8] G. R. Blumenthal, S. M. Faber, J. R. Primack, and M. J. Rees, *Nature* **311**, 517 (1984).
- [9] J. Ruz and The C. A. S. T. Collaboration, *J. Phys.: Conf. Ser.* **110**, 062023 (2008).
- [10] E. W. Kolb and M. S. Turner, *Frontiers in Physics* (Addison-Wesley, Reading, 1990).
- [11] J. L. Feng, arXiv:1003.0904v2 [astro-ph.CO] (2010).
- [12] P. Gondolo, arXiv:astro-ph/0403064 (2004).
- [13] J. A. R. Caldwell and J. P. Ostriker, *Astrophys. J.* **251**, 61 (1981).
- [14] R. Bernabei *et al.*, in *AIP Conf. Proc.*, Vol. 1223 of *AIP Conf. Proc.*, edited by C. Cecchi, S. Ciprini, P. Lubrano, & G. Tosti (AIP, Melville, NY, 2010), pp. 50–59.
- [15] C. Savage, P. Gondolo, and K. Freese, *Phys. Rev. D* **70**, 123513 (2004).

- [16] R. Bernabei *et al.*, Phys. Rev. D **77**, 023506 (2008).
- [17] C. Savage, G. Gelmini, P. Gondolo, and K. Freese, J. Cosmol. Astropart. Phys. **4**, 10 (2009).
- [18] D. P. Finkbeiner, T. Lin, and N. Weiner, Phys. Rev. D **80**, 115008 (2009).
- [19] M. F. Weber *et al.*, Science **287**, 2451 (2000).
- [20] W. Westphal *et al.*, J. Low. Temp. Phys. **151**, 824 (2008).
- [21] J. Ninkovic, Dissertation, Technische Universität München, 2005.
- [22] J. Lewin, Astropart. Phys. **6**, 87 (1996).
- [23] J. Lanfranchi, Dissertation, Technische Universität München, 2005.
- [24] T. Lachenmaier, Dissertation, Technische Universität München, 2005.
- [25] M. Kiefer, Diploma thesis, Julius-Maximilians-Universität Würzburg, 2007.
- [26] H. Kraus *et al.*, Nucl. Instrum. Methods Phys. Res. A **600**, 594 (2009).
- [27] M. Kiefer, private communication (unpublished).
- [28] E. Pantic, Dissertation, Technische Universität München, 2008.
- [29] F. Petricca, Dissertation, Ludwig-Maximilians-Universität München, 2005.
- [30] P. Meunier *et al.*, Appl. Phys. Lett. **75**, 1335 (1999).
- [31] G. Angloher *et al.*, Astropart. Phys. **23**, 325 (2005).
- [32] H. Wulandari, J. Jochum, W. Rau, and F. von Feilitzsch, arXiv:hep-ex/0401032v1 (2004).
- [33] P. Huff, Dissertation, Technische Universität München, 2010.
- [34] T. Jagemann, Dissertation, Technische Universität München, 2004.
- [35] V. B. Mikhailik *et al.*, Phys. Rev. B **69**, 205110 (2004).
- [36] J. Åström *et al.*, Phys. Lett. A **356**, 262 (2006).
- [37] R. Strauss, Diploma thesis, Technische Universität München, 2009.
- [38] M. Aglietta *et al.*, Astropart. Phys. **2**, 103 (1994).

- [39] D. Smith and N. Weiner, Phys. Rev. D **64**, 043502 (2001).
- [40] S. Chang, G. D. Kribs, D. Tucker-Smith, and N. Weiner, Phys. Rev. D **79**, 043513 (2009).
- [41] D. P. Finkbeiner, T. R. Slatyer, N. Weiner, and I. Yavin, J. Cosmology Astropart. Phys. **9**, 37 (2009).
- [42] C. E. Aalseth *et al.*, arXiv:1002.4703v2 [astro-ph.CO] (2010).
- [43] D. Hooper, J. I. Collar, J. Hall, and D. McKinsey, arXiv:1007.1005v2 [hep-ph] (2010).
- [44] The CDMS Collaboration and Z. Ahmed, arXiv:0912.3592v1 [astro-ph.CO] (2009).
- [45] EDELWEISS Collaboration *et al.*, Phys. Lett. B **687**, 294 (2010).
- [46] J. Angle *et al.*, Phys. Rev. Lett. **100**, 021303 (2008).
- [47] The XENON100 Collaboration *et al.*, arXiv:1005.0380v2 [astro-ph.CO] (2010).
- [48] J. I. Collar and D. N. McKinsey, arXiv:1005.0838v3 [astro-ph.CO] (2010).
- [49] The XENON100 Collaboration, arXiv:1005.2615v1 [astro-ph.CO] (2010).
- [50] J. I. Collar and D. N. McKinsey, arXiv:1005.3723v1 [astro-ph.CO] (2010).
- [51] H. Kraus *et al.*, Nucl. Phys. B **173**, 168 (2007).
- [52] [http://www.mindat.org/min\\_3560.html](http://www.mindat.org/min_3560.html).
- [53] K. Nassau and L. G. van Uitert, J. Appl. Phys. **31**, 1508 (1960).
- [54] P. Lecoq *et al.*, *Inorganic Scintillators for Detector Systems: Physical Principles and Crystal Engineering (Particle Acceleration and Detection)* (Springer, Berlin, 2006).
- [55] Cyberstar, Parc Sud Galaxie - 1, Rue des Tropiques - BP 344, 38435 ECHIROLLES Cedex - France.
- [56] H. Rösler, *Lehrbuch der Mineralogie* (Springer, Berlin, 1979).
- [57] K. Nassau and A. M. Broyer, J. Appl. Phys. **33**, 3064 (1962).

- [58] B. Cockayne, D. S. Robertson, and W. Bardsley, Br. J. Appl. Phys. **15**, 1165 (1964).
- [59] A. R. Chaudhuri and L. E. Phaneuf, J. Appl. Phys. **34**, 2162 (1963).
- [60] K. Nassau, J. Phys. Chem. Solids **24**, 1503 (1963).
- [61] H. A. Koehler and C. Kikuchi, Phys. Status Solidi B **43**, 423 (1971).
- [62] T. Edison, Nature **53**, 470 (1896).
- [63] P. A. Rodnyi, *Physical Processes in Inorganic Scintillators (Laser & Optical Science & Technology)*, 1 ed. (CRC-Press, Boca Raton, 1997).
- [64] R. Grasser, A. Scharmann, and K.-R. Strack, J. Lumin. **27**, 263 (1982).
- [65] V. B. Mikhailik, H. Kraus, S. Henry, and A. J. B. Tolhurst, Phys. Rev. B **75**, 184308 (2007).
- [66] T. Frank, Ph.D. thesis, Technische Universität München, 2002.
- [67] M. Moszyński *et al.*, Nucl. Instrum. Methods Phys. Res. A **553**, 578 (2005).
- [68] D. Wahl, V. B. Mikhailik, and H. Kraus, Nucl. Instrum. Methods Phys. Res. A **570**, 529 (2007).
- [69] R. F. Lang *et al.*, arXiv:0910.4414v1 [nucl-ex] (2009).
- [70] D. Curie, *Luminescence in Crystals* (Wiley, New York, 1963).
- [71] E. Hecht, *Optik*, 2 ed. (Addison-Wesley Publishing Company, Reading, MA, 1992).
- [72] O. S. O. America, *Handbook of Optics*, 2 ed. (McGraw-Hill Professional, Columbus, 1994), Vol. 2.
- [73] C. Carrier and R. Lecomte, Nucl. Instrum. Methods Phys. Res. A **278**, 622 (1989).
- [74] C. Gerthsen and H. Vogel, *Gerthsen Physik*, 17 ed. (Springer-Verlag GmbH, Berlin, 1993).
- [75] E. Auffray *et al.*, in *Nucl. Instr. Methods Phys. Res. A: International Conference on Inorganic Scintillators and their use in Scientific and Industrial Applications 6 SCINT 2001* (HAL, Chamonix France, 2002), Vol. 486, pp. 22–34.

- [76] C. Carrier and R. Lecomte, Nucl. Instrum. Methods Phys. Res. A **294**, 355 (1990).
- [77] C. Carrier and R. Lecomte, Nucl. Instrum. Methods Phys. Res. A **292**, 685 (1990).
- [78] J. L. Radtke, Radiation Scintillation Detector, 1990.
- [79] A. N. Ishaque and G. C. Hilton, Radiation detection devices with tapered scintillator crystals, 1993.
- [80] S. E. Derenzo and J. K. Riles, IEEE Trans. Nucl. Sci. **29**, (1982).
- [81] B. Neganov and V. Trofimov, Otkrytia i izobreteniya **146**, 215 (1985).
- [82] P. N. Luke, J. Appl. Phys. **64**, 6858 (1988).
- [83] C. Isaila, Dissertation, Technische Universität München, 2010.
- [84] S. Koynov, M. S. Brandt, and M. Stutzmann, Appl. Phys. Lett. **88**, 203107 (2006).
- [85] P. Huff, private communication (unpublished).
- [86] D. Wahl, Ph.D. thesis, St Catherine's College, Oxford, 2005.
- [87] W. A. Shurcliff and R. Clark Jones, J. Opt. Soc. Am. **39**, 912 (1949).
- [88] R. H. Gillette, Rev. Sci. Instrum. **21**, 294 (1950).
- [89] PerkinElmer, Ferdinand-Porsche-Ring 17, 63110 Rodgau, Germany.
- [90] ET Enterprises Ltd, Riverside Way, Uxbridge, UB8 2YF, UK.
- [91] *9305KB series data sheet*, 5 ed., ET Enterprises Ltd, 09.
- [92] Agilent Technologies Deutschland GmbH, Herrenberger Str. 130, 71034 Böblingen, Deutschland.
- [93] Thorlabs GmbH, Hans-Boeckler-Str. 6, 85221 Dachau/Munich, Germany.
- [94] The measurement was performed by M. Hofmann, Physik-Department E15, Technische Universität München, James-Franck-Straße, D-85748 Garching (unpublished).
- [95] F. Gentit, Nucl. Instrum. Methods Phys. Res. A **486**, 35 (2002).

- [96] D. Strul, J. Sutcliffe-Goulden, P. Halstead, and P. K. Marsden, IEEE Trans. Nucl. Sc. **49**, 619 (2002).
- [97] V. Yakovyna *et al.*, Opt. Mater. **30**, 1630 (2008).
- [98] S. Roth, Diploma thesis, Technische Universität München, 2007.
- [99] M. Kronberger, E. Auffray, and P. Lecoq, IEEE Trans. Nucl. Sc. **55**, 1102 (2008).
- [100] A. Knapitsch *et al.*, Nucl. Instrum. Methods Phys. Res. A **In Press, Corrected Proof**, (2010).

# Acknowledgements

Mein Dank gilt in erster Linie Prof. Franz von Feilitzsch für die Möglichkeit meine Diplomarbeit an seinem Lehrstuhl zu machen. Die besondere Freiheit aber auch seine motivierenden Worte beim Anfertigen dieser Arbeit waren von großem Wert. Außerdem schätze ich den Einsatz und die Unterstützung die er für seine Diplomanden zeigte sowie seine sympathische menschliche Art.

Zusätzlich danke ich auch Prof. Lothar Oberauer und Prof. Tobias Lachenmaier für die freundliche Aufnahme am Lehrstuhl E15.

An nächster Stelle danke ich Walter Potzel und Jean-Come Lanfranchi für die exzellente Betreuung meiner Arbeit. Jean-Come Lanfranchi danke ich besonders für seine ständige Unterstützung sei es in fachlichen oder organisatorischen Dingen bei denen ich sehr von seiner Erfahrung profitiert habe. Außerdem für seine Offenheit und lockeren Umgang der ihn für mich auch zu einem gutem Freund gemacht hat. Walter Potzel möchte ich vor allem für die intensive Hilfe und Zeit die er beim Korrigieren dieser Arbeit aufgewendet hat danken sowie für seine Freundlichkeit und seinen außerordentlich kompetenten fachlichen Rat.

Besonders möchte ich mich außerdem bei meinen Kollegen Raimund Strauss, Sabine Roth, Sebastian Pfister, Christian Ciemniak, Christian Isaila, Achim Gütlein und Michael Willers für die Freundlichkeit mit der ich in der Kryo-Arbeitsgruppe aufgenommen wurde bedanken. Dabei möchte ich die besonders gute Zusammenarbeit mit Raimund Strauss erwähnen dessen Interesse an meiner Arbeit immer eine gute Motivation gewesen ist. Sabine Roth danke ich für die Einführung in die Aufdampfanlagen und Kryostaten und dafür dass ich sie mich so oft mit nach Garching mitgenommen hat.

Desweiteren danke ich Dominikus Hellgartner, Christian Isaila, Raimund Strauss und Michael Willers für die nette Atmosphäre in unserem Büro sowie allen anderen Mitarbeitern des Lehrstuhls E15 für das angenehme Arbeitsklima.

Für die fachliche Hilfe beim Aufbau und Durchführen meiner Experimente danke ich besonders Christian Ciemniak, Marc Tippmann, Michael Wurm und Hermann Hagn. Christian Ciemniak galt für mich als erster Ansprechpartner wenn es um die Charakterisierung von Kristallen ging. Marc Tippmann und Michael Wurm waren mir eine große Hilfe in Sachen Photomultiplier und Datenaufnahme. Hermann

---

Hagn danke ich für die Zeit die er sich beim Aufbau und Entstören der Messelektronik genommen hat.

Special thanks go to David Wahl who never hesitated to answer my questions about the MCRIM technique.

Für die Hilfe beim Anfertigen der Simulationen danke ich besonders Sebastian Pfister, Achim Gütlein, Randolph Möllenberg und Jürgen Winter.

Für die gute Zusammenarbeit bei der Herstellung der Kristalle danke ich außerdem Andreas Erb, Michael Stanger und allen weiteren Mitarbeitern des Kristallabors.

Martin Hofmann danke ich für das zur Verfügung stellen der Messung mit dem Germanium Detektor.

Desweiteren muss ich mich bei Christof Sailer und Sebastian Pfister bedanken die mir bei meinen ersten Schichten am Gran Sasso alles wichtige gezeigt haben.

I would also like to thank all members of the CRESST collaboration, especially Patrick Huff for the good cooperation and fruitful discussions.

Für die Durchführung diverser mechanischer Arbeiten danke ich Harald Hess, Erich Seitz und Thomas Richter von unserem Werkstatt-Team sowie Norbert Gärtner für seine Beratung in Sachen Strahlenschutz.

Besonderer Dank gilt auch unseren Sekretärinnen Maria Bremberger und Sonja Kraus für ihre wichtige Arbeit und die Hilfe bei allen organisatorischen und verwaltungstechnischen Fragen.

Ein ganz besonderer Dank gilt natürlich auch meinen Eltern ohne deren Unterstützung, vor allem in finanzieller Hinsicht, mein Studium nicht möglich gewesen wäre.

Darüber hinaus gibt es einige Leute und Institutionen bei denen ich mich explizit *nicht* bedanken möchte nämlich der bayerischen Regierung und allen anderen Verantwortlichen für die Erhebung von Studiengebühren und ihren Vorstellungen von Bildungsförderung. Außerdem den Münchner Verkehrsbetrieben für die erfolgreiche Verhinderung eines Semestertickets seit über sieben Jahren.

